UNIVERSITY OF READING

Department of Meteorology

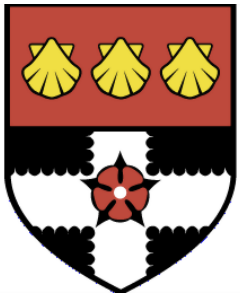

The role of orographic drag in modelled atmospheric circulation

Annelize van Niekerk

A thesis submitted for the degree of Doctor of Philosophy

November 2017

Declaration

I confirm that this is my own work and the use of all material from other sources has been properly and fully acknowledged.

A. van Niekerk

Abstract

Recent studies have demonstrated that the representation of orography in models is highly uncertain. Motivated by the large spread in the climatological circulation and the circulation response to climate change seen among models, the primary aim of this work is to quantify the uncertainty introduced by their representation of orography. This is done through a number of experiments using different comprehensive atmospheric models across horizontal resolutions and timescales.

First, it is shown that two of the models considered are unable to maintain an equivalent total (resolved plus parameterized) orographic drag across resolutions over the Northern Hemisphere (NH) mid-latitudes, leading to systematic biases at lower climate model resolutions. The suitability of substituting one drag parameterization scheme for another is also investigated. It emerges that there is a strong regional dependence of the model error on the drag parameterization scheme employed.

High-resolution global and limited area models analysed over the Himalayan Plateau are used as a proxy for the truth. The non-robustness to resolution over this region is attributed to particular components of the orographic drag parameterization scheme and its formulation. It is shown that most of the reduction in short-range forecast error that occurs with increasing resolution is due to a reduction in the parameterized orographic drag, as opposed to the addition of resolved orographic drag.

Finally, the impact of the uncertainty in the parameterized orographic drag scheme on the circulation and its response to climate change is investigated. The low-level parameterized orographic drag is found to be beneficial for the modelled stationary wave field over the NH and for the jet latitude in both hemispheres. Over the NH, the amplitude of the stationary wave response to climate change across the experiments is shown to scale with the magnitude of low-level parameterized orographic drag through its influence on the present-day climatological stationary wave amplitudes.

Acknowledgements

First and foremost, I would like to thank my supervisor, Ted Shepherd, for his guidance and inspiration. His support of and faith in me has meant a lot for my growth as a person and as a scientist. I have been extremely lucky to be part of Ted's group and I would like to thank them all for broadening my knowledge inside and out of group meetings. In particular, I would like to thank Giuseppe Zappa for his contributing ideas on chapter 6. Inna Polichtchouk for her comments on the introduction and for being a source of positivity and grounding. To Nick Byrne for questioning everything and listening to my problems when I needed it.

I express my gratitude to Miguel Teixeira for his comments on this thesis and for bestowing his theoretical understanding. To my committee members, Maarten Ambaum and Pier Luigi Vidale, for getting me thinking about my work and keeping me on track. Thank you to my examiners, Françoise Lott and to Maarten Ambaum, for taking the time to read the thesis and for their thorough questioning during my viva.

John Scinocca for his great sense of humour and hospitality during my visit with him in Canada. I learnt a lot from our long afternoon discussions, his insightful emails and his knowledge of modelling in general. Norm McFarlane for our chats over coffee and his comments on chapter 6. To everyone at CCCma for their technical assistance and cakes.

Irina Sandu for performing experiments with the ECMWF IFS for analysis in this thesis and for being wonderful in general. To both her and Anton Beljaars for their interesting and thought provoking discussions.

Simon Vosper for replying to all of my long emails and for his enthusiasm towards my work. Stuart Webster for his technical assistance with the Met Office limited area model and to Steve Derbyshire and Andy Elvidge for their helpful discussions.

To the Reading meteorology department, especially the PhD students and 3rd floor Lyle, for making the Met department an amazing place to be.

A huge thank you to my family (including the Weatherleys) for their love and support. Finally, to Adam for everything - you are amazing.

Contents

List of Figures

List of Tables

Chapter 1

Introduction

1.1 Impacts of orography

The impact of orography on the large scale circulation is evident in the stark hemispheric asymmetry that is observed on the Earth. The Northern Hemisphere (NH) storm tracks exhibit large zonal asymmetries and, while there are also large zonal asymmetries in the Southern Hemisphere (SH), the NH deviations tend to stay fixed for longer periods of time and are, therefore, suggestive of geographically fixed sources. These features also maximise downwind of the highest and most extensive mountainous regions. Figure 1.1 illustrates these differences between the hemispheres, showing the 850hPa wind speed and wind vectors from ERA-interim reanalysis (Dee et al., 2011) over the NH wintertime (December, January and February (DJF) mean) between 1979 to 2016. The SH circulation is almost zonally symmetric and the winds are much stronger compared with the NH. Over the NH, the maximum wind speeds occur in the ocean sectors and the jets are tilted towards the pole at their exit region. Near the largest mountainous regions, namely the Himalayan Plateau and the Rocky Mountains, the flow has a tendency to move to the north as it approaches the orography and to the south downwind of it.

Early attempts to understand the role of orography in generating these features were based on conservation of potential vorticity arguments. The conservation of potential vorticity in a barotropic, frictionless, adiabatic atmosphere is given by (Ertel, 1942a,b)[1]:

[1]See Schubert et al. 2004 for English translations of Ertel's texts.

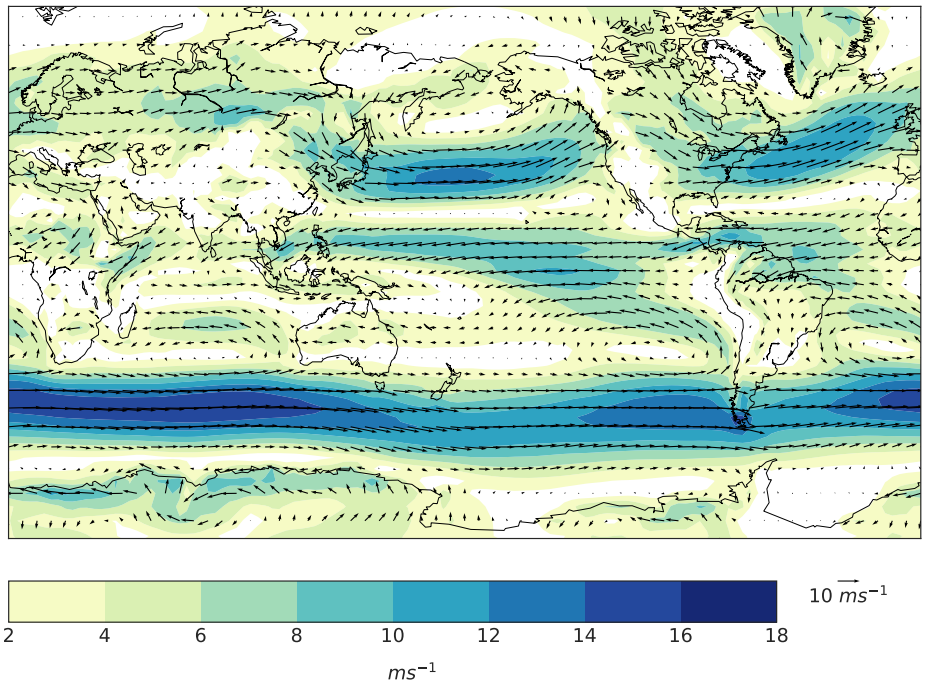

Figure 1.1: NH wintertime (DJF) 850hPa mean winds. Coloured contours are the absolute wind speed ($\sqrt{u^2+v^2}$) and arrows indicate the wind vector.

$$\frac{D}{Dt}\left(\frac{\zeta+f}{H}\right)=0 \tag{1.1}$$

where $H=H(x,y,t)$ is the depth of the fluid column, defined as the distance between potential temperature surfaces θ_0 and $\theta_0+\delta\theta$, $\zeta=\frac{\partial v}{\partial x}-\frac{\partial u}{\partial y}$ is the relative vorticity of the fluid and $f=2\Omega\sin\phi$ is the Coriolis parameter. $D/Dt=\frac{\partial}{\partial t}+\mathbf{u}\cdot\nabla$ is the material derivative following the fluid parcel. Equation (1.1) states that the absolute vorticity $(\zeta+f)$ is conserved following the motion of the fluid, given that the depth of the fluid is constant. However, if the depth of the fluid changes it is the potential vorticity, $(\zeta+f)/H$, that is conserved following the motion. This means that on encountering an elevated surface (i.e. orography) the depth of the fluid will change and, thus, the absolute vorticity must change in order to conserve potential vorticity.

Figure 1.2 shows a classic schematic from Holton (1979) of westerly flow over large scale orography, with figure 1.2(a) depicting a horizontal cross section along the evolution of the fluid column and figure 1.2(b) a plan view of the fluid parcel trajectory. Upstream of the orography the depth of the fluid increases as a result of the vertical

deflection of the $\theta_0 + \delta\theta$ surface. This is balanced by an increase in absolute vorticity, $\zeta + f$, inducing a cyclonic circulation (ζ increases) and a poleward movement of the fluid parcel (f increases). Directly over the mountain, the fluid depth is reduced and a large negative absolute vorticity anomaly is induced. The lower panel of figure 1.2 shows the equatorward movement (f decreases) and anticyclonic tendency (ζ decreases) of the fluid that results from the decrease in the fluid depth. On the lee of the mountain, the fluid parcel is now further equatorward relative to its position on the windward side and has an anticyclonic tendency, meaning that $\zeta + f$ is small. The depth is also increased on the leeward side of the mountain and, in order to counter this, the fluid develops cyclonic curvature (ζ increases) and drifts poleward (f increases) downstream of the orography.

The initial vorticity anomaly induced by the orography sets up a Rossby wave downstream, characterised by positive and negative vorticity anomalies. A similar description of the anomalous vorticity generation of flow going over a mountain can be found in Smith (1979) and a more general description of the response to a vorticity anomaly in Hoskins et al. (1977). The potential vorticity conservation line of reasoning is extremely powerful for explaining the zonal asymmetries identified in figure 1.1. For example, the northward deflection of the flow as it approaches the Rockies and the Himalayas, the southward deflection directly downstream and the northward deflection further downstream, particularly over the Rockies, are indicative of a Rossby wave red response to orography.

The waves generated by orography are a major source of the observed time-mean circulation asymmetries, known as stationary waves. Indeed, the response of simplified representations of the atmosphere (for example, steady linear shallow water models) to orographic forcing mirror many of these observed features (e.g. Charney and Eliassen 1949; Egger 1976; Grose and Hoskins 1979; Nigam et al. 1988; Valdes and Hoskins 1991; Cook and Held 1992, to name a few). Of course, not all of the zonal asymmetry is set up by orography. Differential heating due to sea-surface temperature anomalies (Smagorinsky, 1953) and differences in the heat capacity of the land and ocean also generate these regional features of the large scale circulation, not to mention the important role that transients and non-linear interactions play (Valdes and Hoskins, 1991; Ringler and Cook, 1997). The relative importance of these different forcings in setting up the time-mean circulation has been extensively studied using stationary wave models (see Held et al. 2002 for a review). The success of these models in reproducing the observed

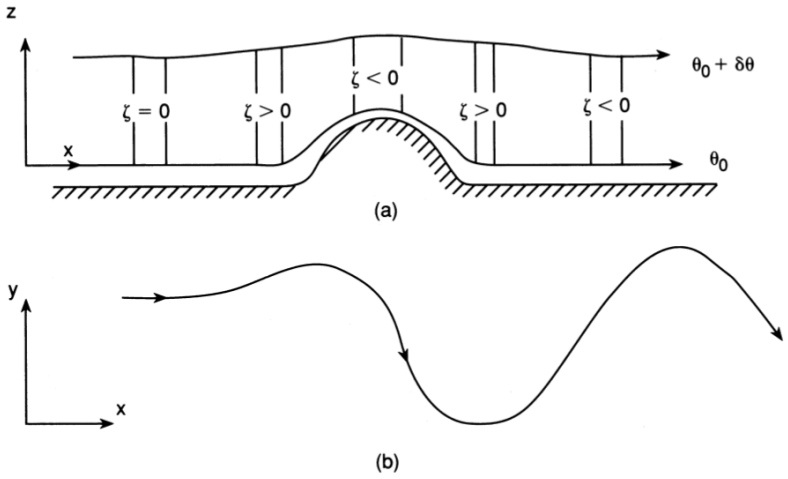

Figure 1.2: Illustration of the relative vorticity perturbation (ζ) that results from the interaction of the atmosphere with large scale orography. (a) A horizontal cross-section and (b) a plan view of the streamline displacement, in which the mean winds are from left to right. Reproduced from Holton (1979).

circulation and their failure to do so without orographic forcing implies not only that the underlying theory is useful in understanding the atmospheric response to different forcings but also that orography is key in this success. Studies with more complex general circulation models have allowed for more accurate and confident attribution of the importance of orography in regional aspects of the circulation, particularly in shaping the south-east to north-west tilting of the mid-latitude jets seen in figure 1.1 (e.g. Kasahara et al. 1973; Manabe and Terpstra 1974; Brayshaw et al. 2009).

As well as affecting the longitudinal and latitudinal structure of the large scale circulation, the interaction between orography and the fluid atmosphere has an impact on the vertical structure of the circulation. Surface perturbations to the flow can propagate upwards in a stably-stratified atmosphere. These vertical perturbations can grow large in amplitude with height, leading to instability and interaction with the mean flow so as to transfer momentum between the troposphere and the upper atmosphere. In order to better understand the characteristics of this propagation, Charney and Drazin (1961) sought to answer the question: how much of the wave energy from the troposphere can propagate into the upper atmosphere and what determines the efficiency of this propagation? They derived a wave equation that describes the vertical

variation of small amplitude disturbances through a mean zonal flow that is assumed to be a function of height only. Their theoretical results, which were closely matched with the observed stratospheric circulation, indicated that it is primarily the variation of the mean zonal winds with height that prevents the wave energy from escaping beyond the lower stratosphere, with the wintertime circulation being more conducive to vertical propagation compared with the summertime circulation. Waves with larger horizontal extents (smaller wavenumbers) are more able to propagate in the vertical so that the troposphere acts as a short-wavelength filter (see also Matsuno 1970 who considered the propagation of stationary waves in the vertical and meridional directions in a background flow that is also varying in both directions).

Generally speaking, planetary scale waves with long horizontal wavelengths are generated by differential heating or orography at the surface. Several studies have asserted that tropospheric conditions can be used as a precursor to sudden stratospheric warmings (e.g. Quiroz 1986; Woollings et al. 2010; Nishii et al. 2011, to name a few). It may then be argued that much of the observed stratospheric disturbances in the NH are due to orographic forcing. Manifestly, the far more frequently observed stratospheric sudden warmings in the NH compared with the SH[2] is indicative of their relationship with the inhomogeneity of the Earth's surface (Matsuno, 1971). In the upper atmosphere, where ozone and other chemical constituents are implicated in the radiative properties of the atmosphere, the breaking of waves generated by orography can alter the distribution and aid mixing of chemical species (e.g. Garcia and Solomon 1985). The Rossby and gravity wave dissipation in the upper atmosphere, in part generated by orography, that occurs in the mid-latitudes helps drive the Brewer-Dobson circulation (Brewer, 1949; Dobson, 1956), a global scale cell which transports air from the tropical tropopause to the mid-latitude stratosphere. This transport is important for the spatial distribution of ozone and water vapour and for the removal of chlorofluorocarbons (CFCs) from the atmosphere.

Orography also has important dynamic impacts on smaller, localised scales. For example, the vertical displacement of air over small scale mountains (unaffected by the Coriolis force) can generate gravity waves that may propagate considerable distances in the vertical (Teixeira, 2014). The breaking of these waves can locally modify the winds at high altitudes and generate clear air turbulence that can have damaging

[2]There has been only one sudden stratospheric warming detected in the Southern Hemisphere since observations began in the 1940s (Krüger et al., 2005).

effects on aircraft (e.g. Lilly 1978; Ralph et al. 1997). Additionally, large amplitude wave breaking close to the mountain top can form a region that restricts the vertical wave propagation, allowing the flow on the leeward side of the mountain to accelerate downslope, generating downslope windstorms (Clark and Peltier, 1977; Peltier and Clark, 1979; Clark and Peltier, 1984). Downslope windstorms may lead to very large near surface wind acceleration, with gusts up to $100ms^{-1}$ (NOAA, 2017), that cause loss and damage of property. Separation of flow around isolated mountains occurs when the air is not able to ascend the orography and von Kàrmàn vortex streets, which are oscillating vorticity anomalies, may form downstream of the mountain. Flow over orography in non-hydrostatic conditions, typically only important for very small scale orography, can result in the horizontal propagation of trapped lee waves generated by the orography (Teixeira et al., 2013). While these phenomena may be due to small scale orography and act locally, their cumulative impact can have implications for the large scale circulation.

So far, only the dynamic impacts of orography have been discussed, being the main focus of the thesis. However, there are also several other important impacts from, for example, moist and thermodynamic processes associated with orography that are briefly touched upon here. The lifting of an air parcel as it approaches a mountain leads to expansion and adiabatic cooling of the parcel. If this cooling is sufficient to produce condensation of water vapour within the parcel and the wind direction prevails, clouds are generated on the windward side of the mountain. Since much of the moisture in the air can be precipitated out before it has completely transversed the mountain, a 'rain shadow' forms on the leeward side. A large scale example of this effect is seen over the Himalayas, where intense rainfall is observed on the southern flank of the Tibetan Plateau and arid conditions are maintained over the Gobi desert. This process can also occur locally on much smaller scales, leading to intense rainfall. What is more, large meridional wind anomalies, generated by orography, cause anomalous advection of moist air from the tropics or dry air from the poles, affecting the local hydro-climate. It is also possible for mountains to change the length of day of the Earth, as the force from the atmosphere onto the orography may be large enough to slow down or accelerate the solid Earth. These length of day changes are small but observable and have been attributed to changes in the mountain torque and the Earth-atmosphere momentum exchange that results from this (Boer, 1990; Salstein and Rosen, 1994).

1.2 Orography in models

It is clear that the zonal and hemispheric asymmetries seen throughout the atmosphere are shaped by the distribution of orography. Without accurate representation of these orographic processes in models accurate and robust predictions of the weather or the circulation sensitivity to climate change are unlikely. Modelling the influence of orography on the climate system becomes problematic, however, when resolving the full orographic spectrum is compromised by the strive for computational efficiency. As an example, the zonal wavenumber power spectra of the orography at 45N from the Global One-km Base Elevation (GLOBE $1km$) dataset[3], a numerical weather prediction (NWP) model and a climate model are shown in figure 1.3. As expected from the distribution of orography in the NH extra-tropics, the spectrum peaks at wavenumber 2. While the power decays at smaller wavenumbers, the GLOBE $1km$ spectrum reveals that this decay is slow and that power exists at many scales. The NWP model, which is generally run for only short periods of time, is resolving much more of the orography at the smaller scales compared with the coarse resolution global climate model, although there is still a substantial fraction that remains unresolved. This means that many sharp and dynamically important orographic features are smoothed by averaging over a grid box or by spectral truncation.

It could be argued that, since much of the orographic power is at the larger scales, the impact of the smaller scales are negligible. However, this assumption has been shown to be false through analysis of error growth in short range forecasting. The initial errors, which tend to be on small scales, rapidly grow in magnitude and contaminate the large scales (Dalcher and Kalnay, 1987). For example, Wallace et al. (1983) showed that some of the systematic error growth in the European Centre for Medium Range Weather Forecasting (ECMWF) model of the time could be attributed to the underrepresentation of orographic forcing. What is more, Tibaldi (1986) showed that much of this error can be alleviated by the addition of power to orography at the small scales only.

To atone for this loss of the smaller scales within models, parameterizations of the sub-grid scale orographic drag processes are introduced. A detailed description of

[3]The Global One-km Base Elevation (GLOBE $1km$) dataset is the source dataset used by the Met Office and the European Centre for Medium Range Weather Forecasting to generate the surface elevation boundary condition for their models.

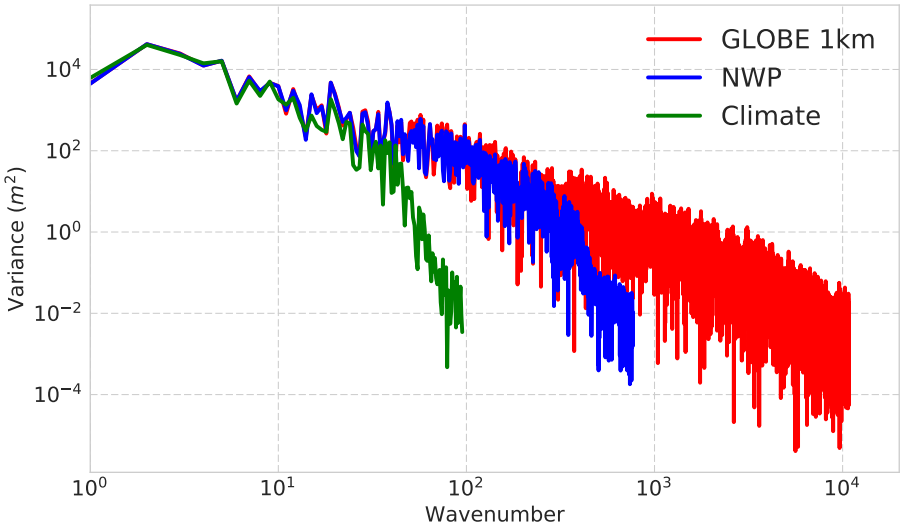

Figure 1.3: Zonal wavenumber power spectra of orography at 45N for the GLOBE dataset, a model at NWP resolution and at climate model resolution.

these parameterizations is presented in section 2.2. The benefits of representing these processes for NWP and climate modelling were first recognised by Palmer et al. (1986), Chouinard et al. (1986), McFarlane (1987) and Miller et al. (1989), who found that excessive westerly wind biases could be alleviated through the addition of a linearly approximated gravity wave drag parameterization. It then became apparent that these sub-grid scale mountain effects went beyond linear gravity wave generation and the addition of a sub-grid scale orographic blocking parameterization, which accounts for the non-linear regimes of flow around orography, led to immense improvements in forecast scores (Lott and Miller, 1997; Scinocca and McFarlane, 2000; Webster et al., 2003). In fact, the success of orographic drag parameterization schemes is testament to the importance of small scale orographic processes for the maintenance of the large scale circulation. There are now three orographic effects that are commonly parameterized in models: the sub-grid scale orographic blocking; gravity wave propagation, which may also include an element of drag due to downslope wind storm generation (Scinocca and McFarlane, 2000); and turbulent orographic form drag. The first two processes account for scales up to the grid-scale and the turbulent drag accounts for scales at which gravity wave generation becomes impossible due to non-hydrostatic effects, which is taken to be up to approximately $5km$ (Beljaars et al., 2004). However, it should be noted that, while all models include a parameterization for orographic gravity wave drag,

the number and construction of parameterized drag processes varies greatly between models.

1.3 Model uncertainty

In general, most of what we have confidence in about the climate response to increased greenhouse gases is thermodynamically controlled and we are left in disagreement over the sensitivity of the atmospheric circulation to climate change (Shepherd, 2014). For example, models within the 5th Coupled Model Inter-Comparison Project (CMIP5) ensemble do not agree on the sign of the latitudinal shift of the NH mid-latitude jets, let alone the magnitude of the response (Barnes and Polvani, 2013). The regional response to climate change exhibits even larger uncertainty, a substantial fraction of which can be attributed to model uncertainty (Hawkins and Sutton, 2009). What is more, the CMIP5 ensemble has revealed that the systematic model biases in the present-day climatology are often considerably larger than the response to climate change (e.g. Zappa et al. 2013). This casts doubt on the models' ability to make trustworthy projections of the circulation under climate change. As well as having systematic biases in their climatologies, models also exhibit a wide spread in magnitude about those biases (e.g. Manzini et al. 2014). The factors at play are numerous. However, examination into the way modelling centres represent particular processes and how uncertainty in these processes affect the circulation may allow us to attribute cause to some of these dynamical uncertainties. As was laid out in the first part of this introduction, orographic processes are crucial for the accurate representation of the atmospheric circulation and, yet, their treatment in models is very uncertain. The contributing issues are discussed below.

Figure 1.3 shows that there is no clear scale separation in the spectrum of orography, meaning that the processes related to the different scales are also not easily separable. Unlike clouds and convection that are typically completely unresolved even in NWP models, the orographic spectrum is partly resolved by the dynamics of the models and the rest must be parameterized. Knowing exactly where to draw the line between what is and is not resolved is complicated by the model having an 'effective resolution' (Davies and Brown, 2001). The effective resolution, as opposed to the grid point resolution, is the number of grid points required to fully represent a processes.

It may not be equal to the grid-point resolution, varies from process to process and is dependent on model numerics. This makes the formulation of resolution-aware parameterization schemes, such as orographic drag parameterizations, even more difficult since they must include the effects of processes on several scales, with those scales being equivocal (Vosper et al., 2016). Coupled with the growing ethos of seamless atmospheric prediction, in which parameterization schemes are expected to perform well at all resolutions without changing their physics, the exchange between parameterized and resolved orographic drag with increasing resolution may be precarious.

Carissimo et al. (1988), Clark and Miller (1991) and subsequently Smith et al. (2005) looked at the horizontal resolution sensitivity of orographic drag over the Alpine regions and found that an increase in resolution did lead to an increase in resolved orographic drag. This is consistent with the notion that an increase in horizontal resolution leads to an increase in the height and slope of the Alpine barrier, which would lead to non-linear, high drag flow regimes (Nappo, 2013; Stein, 1992). Additionally, Vosper (2015) showed that a well tuned orographic drag parameterization scheme within a NWP resolution model can reproduce explicitly resolved drag from higher resolution limited area simulations with a good degree of accuracy. In contrast, Brown (2004) investigated the global resolution dependence of parameterized and resolved orographic torques in the ECMWF Integrated Forecast System (ECMWF IFS) of the time and found that the decrease in the parameterized orographic drag with increased resolution was not compensated by an increase in resolved torque. In fact, the resolved drag changed very little with increasing resolution in certain regions. This leads one to question the ability of models to maintain an equivalent total surface drag globally across a wide range of resolutions, particularly at climate model resolutions. Since different models do not have the same horizontal resolution, their orographic surface boundary conditions and resolved orographic drag will differ. They may also differ in their treatment of resolved orography by using different source datasets or through filtering of the small scale resolved orography to retain model stability (Webster et al., 2003).

The separation of drag into different parameterized components has led to ambiguity in the size of their respective contributions within models. Their representation of unresolved orographic processes will also differ as a result of subjective tuning or different theoretical undertakings. The Working Group on Numerical Experimentation (WGNE) drag inter-comparison project, which aims to better understand the way in which modelling centres close their momentum budgets, found that the boundary

layer stress and low-level orographic blocking parameterizations are often used interchangeably (Zadra et al., 2013). The seemingly arbitrary choices of parameters made in parameterization schemes, as a result of a lack of observational constraints, allow for model tuning so that models with lower orographic blocking tended to have higher boundary layer drag, which includes the turbulent orographic form drag parameterization. Since the boundary layer and orographic drag act on different scales and respond to stability in opposite ways, and the boundary layer parameterization has an impact on the energy budget, this compensation of one for the other may be unphysical. As well as the uncertainty introduced by the various orographic processes, different options for parameterization formulation add another level of complexity. For example, the turbulent orographic form drag can be modelled using an effective roughness length for momentum (Wood and Mason, 1993) or through an explicit orographic stress profile (Wood et al., 2001; Beljaars et al., 2004). The high number of unconstrained, tunable parameters in orographic drag parameterization schemes reflect the state of our understanding of orographic drag processes.

There are reasons to believe that variations in the amount of surface drag, such as orographic drag, have a substantial impact on the circulation from both idealised and fully comprehensive modelling studies. Chen et al. (2007) and Chen and Zurita-Gotor (2008) demonstrated that changes in surface drag in an idealised model can lead to large deviations in the model's climatological jet latitude. More recently, Sandu et al. (2016) demonstrated that, even if a model retains its total low-level parameterized orographic drag, a change in the relative contributions from two different parameterized orographic drag processes can lead to large quantitative differences in the model's circulation and forecast scores. Pithan et al. (2016) showed that the removal of low-level parameterized orographic drag in the Met Office Unified Model can lead to a change in the circulation that is reminiscent of the CMIP5 multi-model mean biases. Specifically, these biases include a too zonal NH circulation, a feature which has for a long time been known to be alleviated by the addition of orography (cf. Charney and Eliassen 1949; Grose and Hoskins 1979; Brayshaw et al. 2009 and several others). It is therefore possible that some of the spread seen in the climatological circulation of models may be attributed to their representation of orography.

From the discussion above, it can be concluded that there are two main sources of uncertainty that arise from the representation of orography in models, namely, model resolution and orographic drag parameterization formulation. The 'uncertainty

in model resolution' refers not only to the resolved orography but also to the response of the parameterization schemes to changes in resolution. Moreover, the orographic drag parameterization formulation encompasses the following: the tuning parameters; the theoretical undertaking; the implementation; and the combination of drag processes included.

1.4 Thesis outline

With the motivations above in mind, it is the purpose of this thesis to assess the role that orographic drag plays in the general circulation of the atmosphere and to understand how its representation in models affects circulation uncertainty and systematic biases. Since much of the work in this thesis is related to the uncertainty in the parameterized orographic drag processes, section 2.1 begins with an introduction to the theory used in formulating the parameterization schemes. Section 2.2 then goes on to describe a particular parameterization scheme in detail. Section 2.3 gives a detailed description of the diagnostics used in the analysis.

In the introduction we identified that there are two main sources of uncertainty in the representation of orography within models: model resolution and orographic drag parameterization formulation. In order to address these it seemed fitting to perform model sensitivity experiments over a range of horizontal resolutions and timescales, and to make use of different models employing different orographic drag parameterizations. Section 3 describes these models used as well as the pre-existing data sets used in their initialisation and validation.

The uncertainty introduced by model resolution is investigated in the first part of chapter 4. Diagnosis of the angular momentum budget, described in detail in section 2.3.1, is used to assess the relative contribution of resolved and parameterized surface drag towards balancing the atmospheric angular momentum flux convergence in an atmospheric model. A nudging framework for constraining the large scale circulation as the horizontal resolution is varied is introduced and validated against short range forecasts. These experiments are then used to assess the fidelity of the exchange between parameterized and resolved orographic torques with changes in horizontal resolution. The results from another atmospheric model are also compared in this chapter. We further demonstrate how the nudging framework can be used to diagnose model drift

and systematic model error over short timescales.

The second part of chapter 4 looks at the circulation sensitivity to changes in the orographic drag parameterization. This is related to the issue of model uncertainty introduced by tuning and a lack of constraints on the contributions from different parameterized surface drag processes. Here, the nudging and momentum budget frameworks are again used to understand how, given the large scale circulation, other drag processes, such as the boundary layer and resolved drag, compensate for changes in the parameterized orographic drag. Since the nudging technique can also be used to diagnose model error, the suitability of substituting one parameterization scheme for another is identified for different regions of the globe.

The results presented in chapter 4 motivate the need for a better understanding of and constraints on the orographic drag parameterization schemes, particularly over complex orography in the NH mid-latitudes. Chapter 5, therefore, makes use of high resolution limited area and global modelling experiments to better understand the shortcomings of the orographic drag parameterization scheme. Since the Himalayan Plateau is one of the largest and most complex orographic regions on the globe and presents a particular challenge for the orographic drag parameterization scheme, the impacts of the orographic drag parameterization scheme are compared with the impacts of additional resolved orography over this region using two different models. A more detailed analysis of the parameterization formulation and its suitability to such complex topography and flow is performed. This allows us to diagnose the origin of the errors that result from this parameterization scheme.

While chapters 4 and 5 look at the importance of orographic representation for model fidelity at short timescales, chapter 6 seeks to understand its impacts at longer timescales. Chapter 6 is focused on the uncertainty introduced by parameterization formulation and parameter tuning in particular. In the first part, a set of experiments, performed with a comprehensive atmospheric general circulation model, is used to ascertain the range of climatological circulations that may arise from orographic drag parameterization uncertainty. A mechanistic investigation of the response to changes in parameterized orographic drag is undertaken. The model's time mean circulation under different parameterization configurations is then compared with reanalysis data to determine the impacts of the orographic drag parameterization scheme on model fidelity.

The second part of chapter 6 is concerned with how the uncertainty in the parameterized orographic drag affects the circulation response to climate change. The set of perturbed parameterized orographic drag model configurations, used in the first part of chapter 6, are then used to perform climate change experiments. A connection between changes in the climatological circulation, brought about by changes to the parameterized orographic drag, and the circulation response to climate change is established using empirical model evidence and linear stationary wave theory.

Finally, chapter 7 summarises the results of the thesis and discusses the implications of the work for the broader field. Open questions and possible future work stemming from the thesis are also presented.

Chapter 2

Theoretical considerations

2.1 Theory of orographic drag

Given here is a non-exhaustive background to the theory that is used in the formulation of orographic drag parameterization schemes. The purpose of this description is to make the reader aware of some of the general assumptions made in orographic drag parameterization schemes so that the work in the chapters to follow is presented in context.

2.1.1 Gravity wave generation

At the scales considered by the parameterization scheme the spherical geometry of the Earth may be neglected. The force exerted on the topography by the atmosphere at the surface of the Earth (in Cartesian coordinates) is given by:

$$\mathbf{F} = \int_{-\infty}^{\infty} \int_{-\infty}^{\infty} p(x, y, 0) \nabla h(x, y) dx dy \tag{2.1}$$

where p the pressure at the surface, h is the surface elevation and $\nabla = (\partial/\partial x, \partial/\partial y)$. Note that the coordinates $p(x, y, z)$ are such that z defines the height from the surface as opposed to mean sea level. The force exerted on the atmosphere is equal and opposite to the force that is exerted on the topography. Since the fluid atmosphere clearly cannot go through the mountain, it must respond to this force locally by going either over or around the obstacle. If the former is the case and the atmosphere is stably stratified,

the vertically displaced fluid generates density anomalies and buoyancy-driven gravity waves can be generated. In the latter case, the fluid moves in the horizontal plane while remaining at low levels. This type of behaviour is referred to as low-level blocking and can lead to vortex shedding and large deceleration of the flow both upstream and downstream of the orography.

The interaction of the atmosphere with orography can be very complicated but by making reasonable approximations about the background flow in which it resides, as well as the shape of the orography itself, it is possible to derive analytical expressions that reproduce the observed and modelled response to orography. For the theory of orographically generated gravity wave used in parameterization schemes these approximations generally include the following:

- The density perturbations due to the orography are small compared with the background density (i.e. $\rho'/\rho_0 \ll 1$), this is the Boussinesq approximation.
- The perturbations are sufficiently small that wave-wave interactions are not taken into account and the linear approximation can be made.
- The rotation of the Earth does not have an impact on the wave generation or propagation.
- The waves are in hydrostatic balance ($\partial p'/\partial z = -\rho' g$).
- The topography is of simple shape, such as an isolated bell-shape or elliptical mountain.
- The flow is inviscid.
- The atmosphere is dry.
- The atmosphere is in a steady state ($\partial/\partial t = 0$).
- The background winds and static stability are constant with height in the region of wave generation.

Making these assumptions and linearising the horizontal momentum, hydrostatic and continuity equations about some background state leads to the following set of equations, following Smith (1980) and Phillips (1984):

$$\rho_0 U u'_x = -p'_x \tag{2.2}$$

$$\rho_0 U v'_x = -p'_y \tag{2.3}$$

$$p'_z = \rho_0 \frac{\theta'}{\Theta} g \tag{2.4}$$

$$u'_x + v'_y + w'_z = 0 \tag{2.5}$$

$$U\theta'_x + w' \frac{d\Theta}{dz} = 0 \tag{2.6}$$

where ρ_0 is the constant background density, g is the acceleration due to gravity and subscripts denote partial derivatives with respect to given a variable (e.g. $u'_x = \frac{\partial u'}{\partial x}$). Primes denote the perturbation from the mean background winds, pressure and potential temperature such that:

$$\begin{aligned} u(x,y,z) &= U + u'(x,y,z) \\ v(x,y,z) &= v'(x,y,z) \\ w(x,y,z) &= w'(x,y,z) \\ p(x,y,z) &= p'(x,y,z) \\ \theta(x,y,z) &= \Theta(z) + \theta'(x,y,z). \end{aligned}$$

Combining equations (2.2)-(2.6) leads to a single equation describing the vertical velocity perturbation (w'):

$$\frac{N^2}{U^2}[w'_{xx} + w'_{yy}] + w'_{xxzz} = 0 \tag{2.7}$$

where $N^2 = \frac{g}{\Theta}\frac{d\Theta}{dz}$ is the background static stability, which is assumed constant with height. Fourier decomposition of the vertical wind perturbation:

$$w'(x,y,z) = \int_{-\infty}^{\infty}\int_{-\infty}^{\infty} \hat{w}(k,l,z) e^{i(kx+ly)} dk dl$$

can then be used to obtain a simple harmonic oscillator equation describing the fluctuations in the amplitude of the wave in the vertical:

$$\hat{w}_{zz} + \left[\frac{N^2}{U^2}\frac{(k^2+l^2)}{k^2}\right]\hat{w} = 0. \tag{2.8}$$

The solution to (2.8) is given by:

$$\hat{w}(k,l,z) = \hat{w}(k,l,0)e^{imz} \tag{2.9}$$

where

$$m = \frac{N}{U}\frac{(k^2+l^2)^{1/2}}{k} \tag{2.10}$$

is the vertical wavenumber and $\hat{w}(x,y,0)$ is the amplitude of the vertical wind perturbation at the surface. For the purposes of understanding the vertical propagation of gravity waves, we assume that the flow goes over the mountain so that the surface boundary condition is:

$$w'(x,y,0) = Uh_x \tag{2.11}$$

where h is the surface elevation. Combining (2.11), the Fourier decomposition of $w'(x,y,z)$ and $h(x,y) = \int_{-\infty}^{\infty}\int_{-\infty}^{\infty}\hat{h}(k,l)e^{i(kx+ly)}dkdl$ leads to:

$$\hat{w}(k,l,0) = iUk\hat{h}(k,l). \tag{2.12}$$

Substituting this into (2.9) and performing an inverse Fourier transform gives an expression for the vertical wind perturbation:

$$w'(x,y,z) = \int_{-\infty}^{\infty}\int_{-\infty}^{\infty} iUk\hat{h}(k,l)e^{imz}e^{i(kx+ly)}dkdl. \tag{2.13}$$

This shows how the vertical wind perturbation is directly proportional to the mean background winds, the height of the topography and the inverse of the horizontal extent of the topography (i.e. the wavenumber k).

For the non-hydrostatic case where (2.4) becomes $\rho_0 U w'_x = \rho_0\frac{\theta'}{\Theta}g - p'_z$, the vertical wavenumber becomes:

$$m = \left(\frac{N^2}{U^2} - k^2\right)^{1/2}\frac{(k^2+l^2)^{1/2}}{k}. \tag{2.14}$$

Comparing (2.10) and (2.14), it can be seen that the hydrostatic approximation is only valid for $k \ll N/U$. For typical atmospheric values of $U = 10ms^{-1}$ and $N = 10^{-2}s^{-1}$ this equates to a horizontal wavelength of $\lambda_x > 2\pi 10^3 m$. This means that orography with horizontal wavelengths smaller than $\sim 6km$ will not be in hydrostatic balance, in typical atmospheric conditions.

Similarly, if rotation is incorporated into the set of equations (2.2)-(2.6) through the f-plane approximation[1], while retaining the hydrostatic approximation[2], the vertical wavenumber becomes:

$$m = \frac{N(k^2 + l^2)^{1/2}}{(U^2k^2 - f^2)^{1/2}}. \tag{2.15}$$

This means that the approximation of non-rotating flow is only valid for $k \gg f/U$. For typical values of U in mid-latitudes ($f = 2\Omega \sin(\pi/4) \approx 10^{-4}s^{-1}$) rotation effects will become important for the generation of waves over orography with horizontal scales larger than $\sim 600km$ ($\lambda_x > 2\pi 10^5 m$). The expression presented in (2.13) is then typically only valid in the range $6km < \lambda_x < 600km$. In general, atmospheric models with resolutions higher than $6km$ will not have a substantial orographic gravity wave drag component, if any, which means the lower bound of the inequality is satisfied. What is more, for sub-grid orography in a typical climate model the largest horizontal scales will be $\sim 300km$, just pushing the upper limit of what is considered unaffected by rotation.

The expression for the vertical velocity perturbation can be used to find an expression for the pressure perturbation at the surface. This is done by recognising that equations (2.2), (2.3) and (2.5) can be combined to form:

$$p'_{xx} + p'_{yy} = \rho_0 U w'_{zx}. \tag{2.16}$$

Substituting (2.13) and $p'(x, y, z) = \int_{-\infty}^{\infty} \hat{p}(k, l, z) e^{i(kx+ly)} dkdl$ into (2.16) gives an expression for the pressure perturbation amplitude:

$$\hat{p} = \frac{i\rho_0 UNk}{(k^2 + l^2)^{1/2}} \hat{h}(k, l) e^{imz}. \tag{2.17}$$

[1] $f = 2\Omega \sin \phi_0$, where Ω is the rotation rate of the Earth and ϕ_0 is some constant reference latitude

[2] This is a consistent combination of approximations, since non-hydrostatic effects are typically only important for small scales, whereas rotation is important for large scales.

The expression for the force exerted on the mountain by the atmosphere due to the pressure perturbation, i.e. (2.1), can be rewritten as:

$$\mathbf{F} = 4\pi^2 i \int_{-\infty}^{\infty}\int_{-\infty}^{\infty} \hat{p}^*(k,l,0)\hat{h}(k,l)\mathbf{k}dkdl \tag{2.18}$$

where $\hat{p}^*$ is the complex conjugate of $\hat{p}$ and $\mathbf{k} = (k,l)$ is the wavenumber vector. Using (2.17) evaluated at the surface in the above equation results in:

$$\mathbf{F} = 4\pi^2 \rho_0 UN \int_{-\infty}^{\infty}\int_{-\infty}^{\infty} \frac{k\mathbf{k}}{(k^2+l^2)^{1/2}}|\hat{h}(k,l)|^2 dkdl. \tag{2.19}$$

Furthermore, by substitution of (2.17) into (2.2) and (2.3) using:

$$\int_{-\infty}^{\infty}\int_{-\infty}^{\infty} \rho_0 \mathbf{u}'(0)w'(0)dxdy = 4\pi^2\rho_0 \int_{-\infty}^{\infty}\int_{-\infty}^{\infty} \hat{\mathbf{u}}^*(k,l,0)\hat{w}(k,l,0)dkdl \tag{2.20}$$

it can be shown that:

$$\mathbf{F} = -\int_{-\infty}^{\infty}\int_{-\infty}^{\infty} \rho\mathbf{u}'(0)w'(0)dxdy \tag{2.21}$$

where $\mathbf{u}' = (u', v')$. In the linear hydrostatic limit the orographic surface pressure torque over an isolated mountain is balanced by the vertical flux of horizontal momentum. This vertical flux of momentum is referred to as the gravity wave stress. Eliassen and Palm (1960) showed that, if the wave stress (denoted by $\tau = \rho_0\mathbf{u}'(z)w'(z)$) is constant with height and the background wind is non-zero, the mean wave energy (given by the sum of the wave kinetic energy and available potential energy) is constant in time. This means that the vertical wave momentum flux from the surface only has an impact on the mean flow when the wave is dissipating, which occurs when the wave breaks or reaches a critical level. The wave dissipation, breaking and critical layer interaction is discussed in more detail in section 2.1.2.

The final expression for the surface pressure force (or gravity wave surface stress) is dependent on the way in which one defines the orography. Smith (1980) used a circular bell-shaped mountain and Phillips (1984) extended this to an elliptical mountain given by:

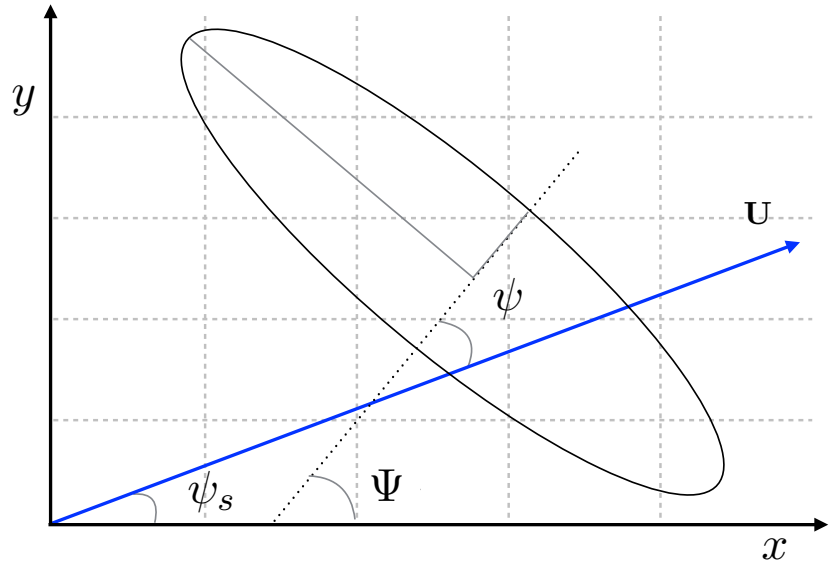

Figure 2.1: Illustration of an elliptical mountain with its major axis rotated by an angle Ψ relative to the x-axis, an impinging wind vector $\mathbf{U}$ at an angle ψ_s relative to the x-axis, and the major axis of topography at an angle ψ relative to the wind vector.

$$h(x,y) = \frac{h_0}{(1+(x/a)^2+(y/b)^2)^{\mu}} \tag{2.22}$$

in which h_0 is the maximum elevation of the orography, a and b are the x and y scales, respectively, and μ is a parameter controlling the sharpness of the terrain.

Phillips (1984) was able to arrive at an expression for the pressure drag for an elliptic barrier that is rotated counter clockwise by an angle Ψ relative to the incoming wind, which is assumed here to be only in the x direction:

$$\mathbf{F} = \rho_0 U N h_0^2 b G \mathbf{D} \tag{2.23}$$

where $\mathbf{D} = (B\cos^2\Psi + C\sin^2\Psi, (B-C)\sin\Psi\cos\Psi)$ and G is a function of μ. B and C are functions of the horizontal scaling length $\gamma = a/b$. For a wind vector ($\mathbf{U}$) that is not purely in the x direction, (2.23) can be redefined as the stress parallel ($F_\parallel$) and perpendicular ($F_\perp$) to the wind vector:

$$\mathbf{F}'_{\parallel,\perp} = \rho_0 |\mathbf{U}| N h_0^2 b G \mathbf{D}'_{\parallel,\perp} \tag{2.24}$$

where $\mathbf{D}'_{\parallel,\perp} = (B\cos^2\psi + C\sin^2\psi, (B-C)\sin\psi\cos\psi)$. Figure 2.1 illustrates the geometry of the orography and the angles referred to in the equation above. $\psi = \Psi - \psi_s$ is the angle between the wind vector and the major axis of topography. ψ_s is the angle between the surface wind vector, $\mathbf{U} = (U, V)$, and the x-axis. (2.24) is the equation on which the formulation for the surface stress from vertically propagating gravity waves is based. It shows that, in the linear hydrostatic non-rotating limit, the stress from orographically generated gravity waves will be larger for orography with a large horizontal and vertical extent and in the presence of strong horizontal winds.

2.1.2 Gravity wave propagation

From (2.8) it can be seen that, for hydrostatic, non-rotating, orographically generated gravity waves, a singularity occurs when $U = 0$. This singularity is called a critical level and represents the point at which the linear theory breaks down. Booker and Bretherton (1967) devised a theory for the behaviour of gravity waves as they approach a critical layer and found that, as the wave approaches a critical level, its perturbation amplitude increases, leading to instability and wave breaking.

The wave becomes unstable when the vertical gradient of the total potential temperature ($\theta = \Theta + \theta'$), that is the perturbation plus mean potential temperature, becomes negative:

$$\frac{d\Theta}{dz} + \frac{\partial\theta'}{\partial z} \leq 0. \tag{2.25}$$

McFarlane (1987) described the growth of the vertical perturbation and the behaviour that leads to convective instability and breaking of gravity waves. In his derivations he does not assume that the winds, static stability and density are independent of height, as has been done in the derivations of gravity wave surface stress, since these factors become important in regions where wave dissipation occurs. By assuming an orographic streamline perturbation of the form $\eta(x, 0) = h_0 \cos kx$ at the surface and that the wavelength of the waves are short compared to variations in the background state (i.e. the Wentzel-Kramer-Brillouin (WKB) approximation), he was able to show that the wave amplitude growth with height can be described by:

$$\eta(x, z) = h_0 \left(\frac{\rho_0(0)N(0)U(0)}{\rho_0(z)N(z)U(z)}\right)^{1/2} \cos\left(kx + \int_0^z \frac{N}{U} dz\right) \tag{2.26}$$

where $\rho_0(0)$, $N(0)$ and $U(0)$ are the values evaluated at the surface. Using the expression $\theta'(z) = -\eta(z)\frac{d\Theta}{dz}$ the instability condition, (2.25), can be rewritten as:

$$\frac{d\Theta}{dz}\left(1 - \frac{\partial\eta}{\partial z}\right) - \eta\frac{d^2\Theta}{dz^2} \leq 0. \tag{2.27}$$

By assuming that the final term on the left hand side is negligible, McFarlane (1987) showed that, to first approximation, convective instability will ensue when the vertical gradient of the streamline displacement is more than unity. In other words, when:

$$F_r(z) = \frac{h_0 N}{U}\left(\frac{\rho_0(0)N(0)U(0)}{\rho_0(z)N(z)U(z)}\right)^{1/2} \geq 1. \tag{2.28}$$

$F_r(z)$ is referred to as the local Froude number. This changes with height and is used to determine the point of wave breaking due to convective overturning, or wave saturation. Equation (2.28) is the criterion used in the MetUM and other orographic gravity wave drag parameterization schemes for the diagnosis of wave breaking.

The amplitude of the streamline displacement can be rewritten as:

$$\eta(x, z) = \frac{F_r U}{N}\cos\left(kx + \int_0^z \frac{N}{U}dz\right), \tag{2.29}$$

showing how η is modulated by this local Froude number such that its amplitude increases with F_r. A decrease in the wind U, static stability N and ρ all contribute towards increasing the amplitude of the wave, bringing it closer to saturation.

Although wave saturation and critical layer interaction are conceptually different, the criteria for wave saturation also satisfies the criteria for the critical layer of an orographically generated stationary wave ($U = 0$). The expression for the local Froude number, (2.28), tells us that F_r and η will go to infinity when the background wind speed goes to zero, which means that the amplitude of the perturbation grows infinitely large, leading to very large streamline displacements and convective overturning.

2.1.3 Orographic blocking

Blocking occurs when the flow is directed around the mountain, rather than over it. Smith (1980) constructed an energy argument for blocking, which makes things more intuitive. If the air is able to flow over the obstacle, as is assumed from the lower

boundary condition in section 2.1.1, then, from (2.23), gravity waves will be generated that radiate energy away at a rate:

$$drag \times U \sim \rho U N h_0^2 b \times U \tag{2.30}$$

and the kinetic energy incident on the mountain would be:

$$(\frac{1}{2}\rho U^2) h_0 b \times U. \tag{2.31}$$

Taking the ratio of these two to determine the efficiency, it is shown that the rate of energy loss will exceed the rate of energy supply when $F_{low} = Nh_0/U > \mathcal{O}(1)$, where F_{low} is the low-level Froude number. In other words, when the energy required to scale the mountain is more than the incoming energy, the flow must avoid the mountain. In this case, the vertical suppression dominates and the fluid parcels are forced to pass around the mountain, while remaining in the horizontal plane. When the low-level Froude number is large enough, so that the incident flow has enough energy, vertical displacement occurs. The depth of the flow that is able to go over the mountain, referred to as the effective height h_{eff}, is determined by the height at which the low-level Froude number is equal to one:

$$F_{low} = \frac{N h_{eff}}{U} = 1. \tag{2.32}$$

Below this height, the flow will go around the mountain. The depth over which this occurs is called the blocking depth and is given by:

$$Z_b = h - h_{eff} \tag{2.33}$$

where h is now the maximum height of the mountain. Figure 2.2 illustrates the separation of the mountain into a blocked layer below and a region of mountain wave generation aloft, where the flow is able to follow the shape of the topography. In reality these processes are not so distinct, and the interaction with the orography is far more complex with several other processes occurring simultaneously. Nevertheless, this theory does provide a way of accounting for the low-level orographic drag processes and the suppression of gravity wave generation in certain flow regimes.

The expression for the low-level blocking drag is largely independent of the linear

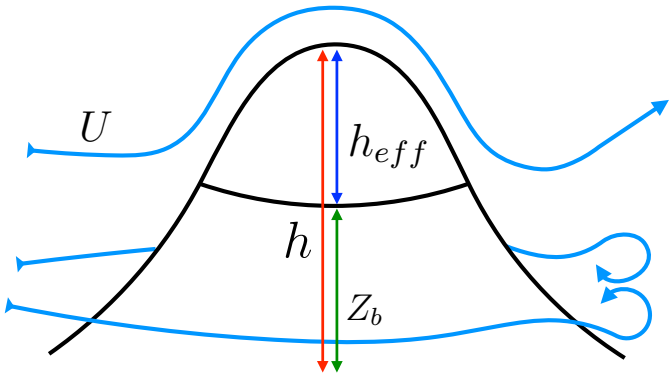

Figure 2.2: Illustration of effective height (h_{eff}) and blocking depth (Z_b) of an idealised mountain with incoming wind U.

wave theory and is based on empirical experiments and bluff body dynamics. The drag exerted on the mountain due to blocking at a particular height z is given by (Lott and Miller, 1997):

$$D_b(z) = \rho C_d l(z) \frac{U(z)|U(z)|}{2} \tag{2.34}$$

where $l(z)$ is the width of the obstacle in the direction of the flow and C_d is the drag coefficient. The width is defined in such a way that it reduces to zero at the top of the mountain and is given as a fraction of the length along the base of the mountain ($2b$):

$$l(z) = 2b \left(\frac{Z_b - z}{z} \right)^{1/2}. \tag{2.35}$$

2.2 Orographic drag parameterization scheme

The orographic drag scheme described here is that of the Met Office Unified Model (MetUM), although there is considerable overlap with the ECMWF IFS and other models. The mean resolved and sub-grid scale orography (SSO) is characterised from a $1km$ resolution source dataset called the Global Land One-Kilometre Base Elevation using the following parameters averaged over the model grid box:

- The mean height in the grid box: $\overline{H}$. This is calculated by averaging the height over all of the $1km$ data points within the model grid box and acts as the surface boundary condition to the resolved dynamics of the model.
- The standard deviation of the SSO: $\sigma = \sqrt{\frac{1}{N}\Sigma(\overline{H} - H)^2}$, where N is the number of source data points in the model grid-box. The SSO height is then defined as $h = n\sigma$, where $n = 2.5$ in the MetUM.
- The squared grid-box average gradient in the x-direction: $\sigma_{xx} = \overline{(\frac{\partial H}{\partial x})^2}$.
- The squared grid-box average gradient in the y-direction: $\sigma_{yy} = \overline{(\frac{\partial H}{\partial y})^2}$.
- The squared grid-box average gradient in the xy-direction: $\sigma_{xy} = \overline{\frac{\partial H}{\partial x}\frac{\partial H}{\partial y}}$.
- The anisotropy of the SSO: $\gamma = a/b$, where a and b are the lengths of the minor and major axis, as in (2.22). This is calculated from the SSO gradients via:

$$\gamma^2 = \frac{\sigma_{xx} + \sigma_{yy} - \sqrt{(\sigma_{xx} - \sigma_{yy})^2 + 4\sigma_{xy}^2}}{\sigma_{xx} + \sigma_{yy} + \sqrt{(\sigma_{xx} - \sigma_{yy})^2 + 4\sigma_{xy}^2}}.$$

- The mean slope of the SSO along the major axis:

$$\alpha^2 = 0.5\left(\sigma_{xx} + \sigma_{yy} + \sqrt{(\sigma_{xx} - \sigma_{yy})^2 + 4\sigma_{xy}^2}\right).$$

- The angle between the minor axis of the topography and the x-axis (see figure 2.1): computed as $\Psi = \frac{1}{2}\arctan\left(\frac{2\sigma_{xy}}{\sigma_{xx} - \sigma_{yy}}\right)$.

All of the parameters above are constant in time but vary from resolution to resolution, due to the grid-box averaging. One time-varying input required in (2.24) that is related to the anisotropy of the SSO is the angle between the low-level wind and the minor axis of topography, illustrated in figure 2.1. For the parameterization of gravity wave stress, this is given by $\psi = \Psi - \psi_s$ where $\psi_s = \arctan(\frac{v_{low}}{u_{low}})$. u_{low} and v_{low} are the low-level wind speeds and are calculated as the average winds over the depth $0.5h$ to h and so represent the wind vector at the top of the SSO. However, for the treatment of parameterized blocking drag $\psi_s(z) = \arctan\left(\frac{v(z)}{u(z)}\right)$ is used.

The source dataset is filtered prior to the calculation of the SSO variables. In the preparation of the resolved grid-box mean orography ($\overline{H}$) that is used in the model dynamics, the source dataset is filtered both prior and post computing the mean over the grid-box. Justification for this and the methods used are given in Webster et al. (2003).

2.2.1 Orographic blocking

The blocking and gravity wave generation components of the orographic drag parameterization are linked as a result of the division of the sub-grid mountain into the blocked layer depth and effective height by $Z_b = h - h_{eff}$ (see figure 2.2). Recall that the effective height is the depth of the mountain that the flow is able to go over, generating vertically propagating waves. This is determined by the low-level Froude number, $F_{low} = Nh/U$. In the MetUM, an inverse Froude number is defined such that $F_{av} = U_{av}/(N_{av}h)$ where U_{av} is the depth averaged wind speed resolved in the direction of the low-level flow and is given by:

$$U_{av} = \left| \frac{(u_{low}u_{av} + v_{low}v_{av})}{\sqrt{(u_{low}^2 + v_{low}^2)}} \right|. \tag{2.36}$$

The parameterization routine calculates the values of u_{av}, v_{av} and N_{av} as the average over the depth:

$$Z_{av} = \max(h, Z_n) + U_{av}/N_{av}. \tag{2.37}$$

Z_n is the depth of a surface neutral layer, if it exists, and is determined as the depth over which $N^2 < 1 \times 10^{-6} s^{-2}$. Since Z_{av} is itself a function of U_{av} and N_{av}, this is solved iteratively until it converges to within 5% of the previous value (or 5 iterations have been performed). This construction of the scheme is motivated by the results of Vosper et al. (2009) and attempts to account for the possibility of non-uniform static stability over the depth of the SSO.

The effective height of the mountain for gravity wave generation is determined via $h_{eff} = U/(NF_c)$, where F_c is a constant referred to as the critical Froude number. F_c takes a value of 4 in the MetUM. Since $F_{low} = 1/F_c$, $F_{low} > 1/4$ determines the point at which blocking occurs in the MetUM. This implies that the parameterization scheme

requires more kinetic energy to generate waves than what is typically anticipated from theory (see section 2.1.1 and Smith 1980). This parameter is treated as a tuning parameter and its small value is indicative of compensation for some other model error.

Lott and Miller (1997) adapted (2.35) so that the horizontal length of the mountain depends on the the angle of the wind relative to the axis of topography (ψ), the blocking depth (Z_b), the length of the minor and major axis (a, b) and the standard deviation of the SSO (σ):

$$l(z) = 2\max(b\sin\psi, a\cos\psi)\left(\frac{Z_b - z}{z + \sigma}\right)^{1/2}. \tag{2.38}$$

There is a reduction in the mountain width with increasing height and at the height of the blocking depth the width is zero. The width is summed over the number of obstacles encountered within the grid box (i.e. (2.38)$\times L_x L_y/4ab$) so that:

$$l(z) = \left(\frac{Z_b - z}{z + \sigma}\right)^{1/2}\left(\frac{L_x L_y}{2}\right)\max(\frac{\cos\psi}{a}, \frac{\sin\psi}{b}). \tag{2.39}$$

Here, L_x and L_y are the x and y dimensions of the grid box. Estimating that $a \sim \sigma/\alpha$ and $a/b \sim \gamma$ leads to the following expression for the orographic blocking drag:

$$\mathbf{D_b}(z) = C_d\max\left(2 - \frac{1}{r}, 0\right)\rho\frac{\alpha}{2\sigma}\left(\frac{Z_b - z}{z + \sigma}\right)^{1/2}\max(\cos\psi, \gamma\sin\psi)\frac{\mathbf{U}|\mathbf{U}|}{2} \tag{2.40}$$

where $\mathbf{U} = (U, V)$ is the mean wind vector and r is given by:

$$r = \left(\frac{\cos^2\psi + \gamma^2\sin^2\psi}{\gamma^2\cos^2\psi + \sin^2\psi}\right)^{1/2}. \tag{2.41}$$

The coefficient involving r allows the drag coefficient to vary with the aspect ratio, such that it is multiplied by a number between one and two (or zero) depending on whether the flow is parallel or perpendicular to the major axis of topography.

The directional terms can be approximated as $max(\cos\psi, \gamma\sin\psi) = (B\cos^2\psi + C\sin^2\psi)$. B and C are as in (2.23) and are given by $B = 1 - 0.18\gamma - 0.04\gamma^2$ and $C = 0.48\gamma + 0.3\gamma^2$, which are based on empirical approximations of the integrals described in Phillips (1984) (see also Teixeira and Miranda 2006).

Finally, the blocking drag per unit area within a grid box is then represented in the model through the expression:

$$\mathbf{D_b}(z) = C_d \max\left(2 - \frac{1}{r}, 0\right) \rho \frac{\alpha}{2\sigma} \left(\frac{Z_b - z}{z + \sigma}\right)^{1/2} \times (B\cos^2\psi + C\sin^2\psi)\frac{\mathbf{U}|\mathbf{U}|}{2}. \quad (2.42)$$

There is another unconstrained parameter in (2.42), namely C_d the drag coefficient. While studies have identified the likely magnitudes of this parameter through numerical or laboratory tank experiments (e.g. Vosper 2000), it is very much still a large source of uncertainty. In the MetUM, this parameter is arbitrarily set to 4 operationally. For comparison, this value is set to 2 in the ECMWF IFS.

Finally, the way in which the large scale flow is affected by the orographic blocking is through:

$$\frac{\partial \mathbf{U}}{\partial t} = -\frac{1}{\rho(z)}\mathbf{D_b}(z) \quad (2.43)$$

where $\rho(z)$ is the density at each height level in the model.

2.2.2 Gravity wave drag

The gravity wave drag parameterization scheme is based on the theory described in section 2.1.1 and makes use of the parameters listed at the beginning of section 2.2. The expression for the wave stress, that is the stress exerted on the mountain by the wind, is as in equation (2.24). Since the ψ is the angle between the minor axis of topography and the wind, the surface stress $\mathbf{F'}_{\parallel,\perp}$ is defined as the stress parallel and perpendicular to the low-level flow. It is convenient to describe the stress in this way since wave breaking at a critical level only occurs if the wind speed resolved in the direction of the surface stress is reducing or goes to zero.

As had been done for the blocking term, the stress is summed over the number of obstacles encountered in the grid box so that:

$$\mathbf{F'}_{\parallel,\perp} = \rho_{low} U_{low} N_{low} h_0^2 b G \mathbf{D'}_{\parallel,\perp} \times (\frac{L_x L_y}{4ab}) \quad (2.44)$$

where $U_{low} = \sqrt{u_{low}^2 + v_{low}^2}$ and ρ_{low} is the density averaged from $0.5h$ to h. G is set to

1 in the MetUM. The surface stress per unit area can then be defined as:

$$\mathbf{F'}_{\parallel,\perp} = \frac{\rho_{low} U_{low} N_{low} h_0^2 G}{4a} \mathbf{D'}_{\parallel,\perp}. \tag{2.45}$$

The minor axis of topography is approximated as the height of the topography over the mean slope ($a = \sigma/\alpha$) and h_0 is replaced by the effective height of the topography. The final expression for the gravity wave surface stress then becomes:

$$\mathbf{F'}_{\parallel,\perp} = \frac{\rho_{low} U_{low} N_{low} h_{eff}^2 G\alpha}{4\sigma} \mathbf{D'}_{\parallel,\perp}. \tag{2.46}$$

The saturation criteria for this scheme follows the work of McFarlane (1987), as is described in section 2.1.2. The wave breaks when a critical wave amplitude is reached, i.e. $A(z) > F_{sat} U(z)/N(z)$, in which:

$$A(z) = A(z-1) \left(\frac{\rho(z-1) U(z-1) N(z-1)}{\rho(z) N(z) U(z)} \right)^{1/2} \tag{2.47}$$

where z corresponds to the model level at which the values are calculated and $z-1$, therefore, corresponds to the value calculated on the model level just below. The amplitude at the surface is $A(0) = h_{eff}$. $U(z)$ is the wind speed at some model level resolved in the direction of the surface stress, such that:

$$U(z) = \frac{[u_{\parallel}(z), u_{\perp}(z)] \cdot \mathbf{D'}_{\parallel,\perp}}{|\mathbf{D'}_{\parallel,\perp}|} \tag{2.48}$$

where $u_{||}(z) = (u(z)u_{low} + v(z)v_{low})/|u_{low}|$ and $u_{\perp}(z) = (-v_{low}u(z) + u_{low}v(z))/|u_{low}|$ is the wind at some level z resolved in the direction parallel and perpendicular to the low-level winds, respectively.

The point at which the critical wave amplitude is reached is equivalent to the point at which the local Froude number in (2.28) exceeds unity since $F_{sat} = 1$ in the MetUM. The wave amplitude is then set to the critical amplitude and the wave stress is allowed to vary with height according to:

$$\tau(z) = \tau(z-1) \left(\frac{A(z)}{A(z-1)} \right)^2 \frac{\rho(z) N(z) U(z)}{\rho(z-1) N(z-1) U(z-1)}. \tag{2.49}$$

It should be pointed out that, since $U(z)$ is component of the wind in the direction of the surface stress, $\tau(0) = |\mathbf{F}_{\parallel,\perp}| = \rho_{low} U_{low} N_{low} h_{eff}^2 G\alpha |\mathbf{D'}_{\parallel,\perp}|/4\sigma$ defines the magnitude of

the surface stress. When the wave amplitude has not been set to the critical amplitude, the coefficients of $\tau(z-1)$ cancel to unity and there is no change in stress with height. However, the critical wave amplitude is approached as $U \to 0$, $N \to 0$ or $\rho \to 0$. When this occurs the amplitude of the wave will become very large and the critical wave amplitude very small, resulting in rapid dissipation of the wave and a reduction of the wave stress towards zero. Since the vertical grid is staggered in the MetUM, the values for the stress τ are calculated on the model's full levels and the tendencies are then applied to the resolved flow on the model's half levels using:

$$\frac{\partial U}{\partial t} = \frac{(\tau(z) - \tau(z-1))}{\rho_{av}\lambda_z(z)} \tag{2.50}$$

where $\lambda_z = \lambda_{frac} \times \frac{2\pi U(z)}{N(z)}$ is the vertical wavelength of the wave multiplied by some fraction ($\lambda_{frac} = 1$) and ρ_{av} is the density averaged over the height of λ_z. All of the stress is deposited as a constant deceleration extending from $z - \lambda_z$ to $z + \lambda_z$, where z is the point at which the saturation is diagnosed. This is based on the high resolution simulations undertaken by Epifanio and Qian (2008), in which they show that almost all of the wave stress is dissipated over one vertical wavelength. This approach of smoothing the stress deposition is also taken in order to improve the numerical stability of the model. If the wave breaks close to the sub-grid mountain top (i.e. $z - \lambda_z$ extends below h) the momentum is deposited from a height of $z + \lambda_z$ down to the surface at $z = 0$.

2.3 Diagnostics

2.3.1 Momentum budget calculations

The momentum budget is used frequently as a diagnostic throughout this work. It provides a measure of the relative importance of different terms for the atmospheric circulation but it also acts as a means of comparison between different models and model configurations. Below is a description of the momentum budget as well as the different forms that it may take as a result of various approximations. The method of discretisation for derivatives in the horizontal directions and integrals in the vertical are also given.

In the Met Office Unified Model the equation for the zonal wind component (u)

in spherical polar coordinates on hybrid geometric height coordinates (η) is given by (Staniforth et al., 2006):

$$\frac{Du}{Dt} = \frac{uv\tan\phi}{r} - \frac{uw}{r} + fv - 2\Omega\cos\phi w - \frac{1}{\rho r\cos\phi}\left(\frac{\partial p}{\partial\lambda} - \frac{\partial p}{\partial r}\frac{\partial r}{\partial\lambda}\right) + F_\lambda \tag{2.51}$$

where the material derivative following a fluid parcel is:

$$\frac{D}{Dt} = \frac{\partial}{\partial t} + \frac{u}{r\cos\phi}\frac{\partial}{\partial\lambda} + \frac{v}{r}\frac{\partial}{\partial\phi} + \dot{\eta}\frac{\partial}{\partial\eta} \tag{2.52}$$

$f = 2\Omega\sin\phi$ is the Coriolis parameter, r is the distance from the center of the Earth, u, v and w are the wind speeds in the zonal, meridional and vertical directions, respectively, and $\dot{\eta} = w\frac{\partial\eta}{\partial r} - \frac{u}{r\cos\phi}\frac{\partial r}{\partial\lambda}\frac{\partial\eta}{\partial r} - \frac{v}{r}\frac{\partial r}{\partial\phi}\frac{\partial\eta}{\partial r}$. The F_λ term is the sum of all the tendencies from parameterized processes that act on the zonal winds. In the MetUM, these include the parameterizations of boundary layer turbulent drag, orographic gravity wave drag, orographic blocking drag, spectral gravity wave drag and convective entrainment of momentum.

The continuity equation on hybrid geometric height coordinates is given by:

$$\frac{\partial}{\partial t}\left(r^2\rho\frac{\partial r}{\partial\eta}\right) + \frac{1}{\cos\phi}\frac{\partial}{\partial\lambda}\left(ru\rho\frac{\partial r}{\partial\eta}\right) + \frac{1}{\cos\phi}\frac{\partial}{\partial\phi}\left(rv\cos\phi\rho\frac{\partial r}{\partial\eta}\right) + \frac{\partial}{\partial\eta}\left(r^2\dot{\eta}\rho\frac{\partial r}{\partial\eta}\right) = 0. \tag{2.53}$$

Performing the operation $G\times(2.53) + \cos\phi r^2\rho\frac{\partial r}{\partial\eta}\times\frac{DG}{Dt}$ on some scalar field G gives the following identity:

$$\begin{aligned}\cos\phi r^2\rho\frac{\partial r}{\partial\eta}\frac{DG}{Dt} = &\frac{\partial}{\partial t}\left(r^2G\cos\phi\rho\frac{\partial r}{\partial\eta}\right) + \frac{\partial}{\partial\lambda}\left(ruG\rho\frac{\partial r}{\partial\eta}\right)\\ &+\frac{\partial}{\partial\phi}\left(rvG\cos\phi\rho\frac{\partial r}{\partial\eta}\right) + \frac{\partial}{\partial\eta}\left(r^2\dot{\eta}G\cos\phi\rho\frac{\partial r}{\partial\eta}\right).\end{aligned} \tag{2.54}$$

Setting $G = ur\cos\phi$ allows for the combination of the zonal momentum and continuity equations:

$$\cos\phi r^2\rho\frac{\partial r}{\partial\eta}\frac{D}{Dt}(ur\cos\phi) = \frac{\partial}{\partial t}\left(ur^3\cos^2\phi\rho\frac{\partial r}{\partial\eta}\right) + \frac{\partial}{\partial\lambda}\left(uu\cos\phi r^2\rho\frac{\partial r}{\partial\eta}\right) + \frac{\partial}{\partial\phi}\left(uvr^2\cos^2\phi\rho\frac{\partial r}{\partial\eta}\right) + \frac{\partial}{\partial\eta}\left(u\dot{\eta}r^3\cos^2\phi\rho\frac{\partial r}{\partial\eta}\right). \tag{2.55}$$

Expanding $D(ur\cos\phi)/Dt = r\cos\phi Du/Dt + uD(r\cos\phi)/Dt$, using equation (2.51) and cancelling terms gives:

$$\frac{D}{Dt}(ur\cos\phi) = fvr\cos\phi - 2\Omega r\cos^2\phi w - \frac{1}{\rho}\left(\frac{\partial p}{\partial\lambda} - \frac{\partial p}{\partial r}\frac{\partial r}{\partial\lambda}\right) + F_\lambda r\cos\phi. \tag{2.56}$$

Substitution of (2.56) into (2.55), divided through by $r^2\cos\phi$ (while remaining aware of the fact that the MetUM has a vertical coordinate that is dependent on r and uses a deep atmosphere), gives:

$$\begin{aligned}\frac{\partial}{\partial t}\left(ur\cos\phi\rho\frac{\partial r}{\partial\eta}\right) + \frac{1}{r^2}\frac{\partial}{\partial\lambda}\left(uur^2\rho\frac{\partial r}{\partial\eta}\right) \\ + \frac{1}{r^2\cos\phi}\frac{\partial}{\partial\phi}\left(uvr^2\cos^2\phi\rho\frac{\partial r}{\partial\eta}\right) + \frac{1}{r^2}\frac{\partial}{\partial\eta}\left(\dot{\eta}ur^3\cos\phi\rho\frac{\partial r}{\partial\eta}\right) \\ -fvr\cos\phi\rho\frac{\partial r}{\partial\eta} + 2\Omega r\cos^2\phi w\rho\frac{\partial r}{\partial\eta} + \left(\frac{\partial p}{\partial\lambda} - \frac{\partial p}{\partial r}\frac{\partial r}{\partial\lambda}\right)\frac{\partial r}{\partial\eta} - F_\lambda r\cos\phi\rho\frac{\partial r}{\partial\eta} = 0.\end{aligned} \tag{2.57}$$

This is the full three dimensional angular momentum equation for the MetUM. However, for the purposes of simplicity and for diagnostic calculation it is assumed that the horizontal derivatives of r are comparatively small (i.e. shallow atmosphere approximation). This then leaves the simpler form of the angular momentum ($m = ua\cos\phi$) equation:

$$\begin{aligned}\frac{\partial}{\partial t}\left(m\rho\frac{\partial r}{\partial\eta}\right) + \frac{1}{a\cos\phi}\frac{\partial}{\partial\lambda}\left(um\rho\frac{\partial r}{\partial\eta}\right) \\ + \frac{1}{a\cos\phi}\frac{\partial}{\partial\phi}\left(vm\cos\phi\rho\frac{\partial r}{\partial\eta}\right) + \frac{\partial}{\partial\eta}\left(\dot{\eta}m\rho\frac{\partial r}{\partial\eta}\right) \\ -fva\cos\phi\rho\frac{\partial r}{\partial\eta} + 2\Omega a\cos^2\phi w\rho\frac{\partial r}{\partial\eta} + \left(\frac{\partial p}{\partial\lambda} - \frac{\partial p}{\partial r}\frac{\partial r}{\partial\lambda}\right)\frac{\partial r}{\partial\eta} - F_\lambda a\cos\phi\rho\frac{\partial r}{\partial\eta} = 0.\end{aligned} \tag{2.58}$$

Sensitivity tests with output from experiments in chapter 4 reveal little difference in the overall magnitude of the terms when this assumption is made. However, this approximation is likely to be less accurate when going to much higher resolution as a result of the increasing horizontal gradients in r.

Taking the vertical integral of (2.58) on η levels from the top of the atmosphere to the surface, transforming the integral bounds to $\int_{z_0}^{\infty}$ and performing a zonal average then leaves:

$$\begin{aligned}\frac{\partial}{\partial t}\left[\int_{z_0}^{\infty} m\rho dr\right] + \frac{1}{a\cos\phi}\frac{\partial}{\partial\phi}\left[\int_{z_0}^{\infty} vm\cos\phi\rho dr\right] - \left[\int_{z_0}^{\infty} fva\cos\phi\rho dr\right] \\ + \left[\int_{z_0}^{\infty} 2\Omega a\cos^2\phi w\rho dr\right] - \left[p_0\frac{\partial z_0}{\partial\lambda}\right] - \left[\int_{z_0}^{\infty} F_\lambda a\cos\phi dr\right] = 0\end{aligned} \tag{2.59}$$

where [..] denotes a zonal average, p_0 is the pressure at the surface (on the first model level) and z_0 is the surface elevation. Since the model's top and bottom boundary conditions are such that $\dot{\eta}(0) = 0$ and $\dot{\eta}(1) = 0$, respectively, the vertical momentum flux terms disappear in the integral. Equation (2.59) is the equation that is used for the diagnostics in chapter 4.

Since the deep atmosphere terms are likely to play more of a role at higher resolutions and it is necessary to consider the lateral terms when a zonal average over a non-periodic domain cannot be taken, as is the case for a limited area domain, the vertically integrated momentum budget diagnostics used in chapter 5 discretise the full momentum equation as follows:

$$\begin{aligned}\frac{\partial}{\partial t}\left(\int_{z_0}^{\infty} u\rho dr\right) + \int_{z_0}^{\infty}\frac{1}{r^3\cos\phi}\frac{\partial}{\partial\lambda}\left(uur^2\rho\right)dr \\ + \int_{z_0}^{\infty}\frac{1}{r^3\cos^2\phi}\frac{\partial}{\partial\phi}\left(uvr^2\cos^2\phi\rho\right)dr - \int_{z_0}^{\infty} fv\rho dr + \int_{z_0}^{\infty} 2\Omega\cos\phi w\rho dr \\ + \int_{z_0}^{\infty}\frac{1}{r\cos\phi}\left(\frac{\partial p}{\partial\lambda} - \frac{\partial p}{\partial r}\frac{\partial r}{\partial\lambda}\right)dr - \int_{z_0}^{\infty} F_\lambda\rho dr = 0.\end{aligned} \tag{2.60}$$

To prevent over-complication, however, the momentum equation quoted in chapter 5 assumes a shallow atmosphere.

In chapter 4 the terms are calculated from 6-hourly output, whereas terms in chapter 5 are calculated using 3-hourly output. Before calculating the terms, the variables are interpolated onto the same grid, the Arakawa B grid, since the MetUM uses a horizontally staggered Arakawa C-grid (Arakawa and Lamb, 1977). The horizontal derivatives are performed in grid-point space and are centred differences, for example a derivative in the zonal direction in a periodic domain with N points and a resolution of $\Delta\lambda$ is given by:

$$\left.\frac{\partial X}{\partial \lambda}\right|_i = \begin{cases} \dfrac{(X_1 - X_N)}{2\Delta\lambda}, & \text{for } i = 0 \\ \dfrac{(X_{i+1} - X_{i-1})}{2\Delta\lambda}, & \text{for } i = 1, 2, ..., N-1 \\ \dfrac{(X_0 - X_{N-1})}{2\Delta\lambda}, & \text{for } i = N \end{cases} \tag{2.61}$$

and in the meridional direction, with a resolution of $\Delta\phi$ and N points, by:

$$\left.\frac{\partial X}{\partial \phi}\right|_j = \begin{cases} \dfrac{(X_1 - X_0)}{\Delta\phi}, & \text{for } j = 0 \\ \dfrac{(X_{j+1} - X_{j-1})}{2\Delta\phi}, & \text{for } j = 1, 2, ..., N-1 \\ \dfrac{(X_N - X_{N-1})}{\Delta\lambda}, & \text{for } j = N. \end{cases} \tag{2.62}$$

The only term that requires a vertical derivative is the pressure term, $\partial p/\partial r$. The model uses a Charney-Phillips grid staggering in the vertical and this derivative is taken on the model's full vertical levels, which start at the surface, so that the derivative is valid at the model's half levels. This is performed using a centred difference as follows:

$$\left.\frac{\partial X}{\partial r}\right|_k = \frac{(X_{k+\frac{1}{2}} - X_{k-\frac{1}{2}})}{(r_{k+\frac{1}{2}} - r_{k-\frac{1}{2}})}, \text{ for } k = \frac{1}{2}, \frac{3}{2}..., N - \frac{1}{2}. \tag{2.63}$$

Since the zonal winds are solved on the model's half levels the vertical integrals are computed using the heights (r) on the model's full levels:

$$\int_{z_0}^{\infty} X dr = \sum_{k=\frac{1}{2}}^{k=N-\frac{1}{2}} X_k (r_{k+\frac{1}{2}} - r_{k-\frac{1}{2}}). \tag{2.64}$$

The time derivative in the momentum budget equation, whichever form it takes, is calculated as the difference between the values of $\int_{z_0}^{\infty} u\rho dr$ at the end and beginning of the integration divided by the length of the integration. For the continuous nudged experiments this means taking the difference between the output at the end and beginning of the month of integration. For the short range forecasts, however, this means taking the difference at the end of the 24 hour forecast and the beginning of the model output, since there will be a discontinuity when the model is reinitialised. It should also be noted that in the nudged experiments the nudging tendencies act as an additional term within the momentum budget and are vertically integrated in the same way as the parameterized tendencies using (2.64).

In a hydrostatic model which assumes a shallow atmosphere and has a hybrid pressure coordinate system, as CanAM and ECWMF IFS do, the angular momentum budget (2.59) becomes:

$$\begin{aligned} &\frac{\partial}{\partial t}\left[\int_0^{p_0} m\frac{dp}{g}\right] + \frac{1}{a\cos\phi}\frac{\partial}{\partial\phi}\left[\int_0^{p_0} vm\cos\phi\frac{dp}{g}\right] \\ &-\left[\int_0^{p_0} fa\cos\phi v\frac{dp}{g}\right] - \left[p_0\frac{\partial z_0}{\partial\lambda}\right] - \left[\int_0^{p_0} F_\lambda a\cos\phi\frac{dp}{g}\right] = 0 \end{aligned} \tag{2.65}$$

where a is the mean radius of the Earth and $m = ua\cos\phi$. This is the equation discretised in the analysis of the ECMWF IFS in chapter 4. Equivalently, the momentum budget ((2.65) divided by $r\cos\phi$) becomes:

$$\begin{aligned} &\frac{\partial}{\partial t}\left[\int_0^{p_0} u\frac{dp}{g}\right] + \frac{1}{a\cos^2\phi}\frac{\partial}{\partial\phi}\left[\int_0^{p_0} uv\cos^2\phi\frac{dp}{g}\right] \\ &-\left[\int_0^{p_0} fv\frac{dp}{g}\right] - \left[\frac{p_0}{a\cos\phi}\frac{\partial z_0}{\partial\lambda}\right] - \left[\int_0^{p_0} F_\lambda\frac{dp}{g}\right] = 0. \end{aligned} \tag{2.66}$$

In CanAM4.1 this equation is discretised on the model's hybrid height vertical coordinate system with any zonal or meridional derivatives computed in spectral space and the vertical integrals discretised as in Laprise and Girard (1990).

2.3.2 Stationary Plumb flux

In chapter 6 the stationary Plumb flux is used to diagnose changes in the stationary wave forcing of the mean flow that result from changes in the parameterized orographic drag. The full derivation of the stationary Plumb flux can be found in Plumb (1985) and

of the Eliassen-Palm (EP) flux, from which it is descended, can be found in Andrews and McIntyre (1976) and will, therefore, not be derived here but, instead, a description of its relevance is given.

The waves generated by topography, or any other sources, are able to transport momentum and energy from their source region to other regions of the atmosphere in the longitudinal, latitudinal and vertical directions. Generally, these waves are measured as a departure from the zonal mean circulation and their ability to impart changes to the zonal mean circulation gives rise to the concept of wave-mean flow interaction. A measure of this transport of momentum by waves in the atmosphere is the Eliassen-Palm flux ($\mathbf{F}$). Using quasi-geostrophic scaling of the zonal momentum and thermodynamic equations in log-pressure coordinates[3], it can be shown that $\mathbf{F}$ is related to the zonal mean zonal wind, $U(y,z)$, through:

$$\frac{\partial U}{\partial t} + \frac{1}{p}\nabla \cdot \mathbf{F} = C \tag{2.67}$$

where $\nabla = (\frac{\partial}{\partial y}, \frac{\partial}{\partial z})$ is the divergence operator in the meridional and vertical directions, p is the pressure at a given level, C contains negligible or non-conservative terms and $\mathbf{F}$ is the two-dimensional Eliassen-Palm flux vector given by:

$$\mathbf{F} = p(-[u^*v^*], \frac{f_0[v^*\theta^*]}{\frac{\partial \Theta}{\partial z}}). \tag{2.68}$$

The superscript * denotes a deviation from the background mean zonal flow, [..] denotes a zonal average and $\Theta(y,z)$ is the zonal mean potential temperature. Since this form of $\mathbf{F}$ is derived from the equations on a beta-plane, f_0 is the Coriolis parameter at some reference latitude. The relation (2.67) tells us that meridional fluxes of momentum (u^*v^*) and heat ($v^*\theta^*$) interact with the mean flow in a coupled manner, reflecting geostrophic balance.

It is possible to show that:

$$\frac{1}{p}\nabla \cdot \mathbf{F} = [v^*q^*] \tag{2.69}$$

where q^* is the quasi-geostrophic potential vorticity perturbation:

[3] $z = -Hln(\frac{p}{p_0})$, where $H = 7km$ is the scale height, $p_0 = 1000$hPa

$$q^* = \frac{\partial^2 \psi^*}{\partial x^2} + \frac{\partial^2 \psi^*}{\partial y^2} + \frac{f_0^2}{p}\frac{\partial}{\partial z}\left(\frac{p}{N^2}\frac{\partial \psi^*}{\partial z}\right) \tag{2.70}$$

ψ^* is the streamfunction perturbation and in quasi-geostrophic flow the following holds:

$$u^* = -\frac{\partial \psi^*}{\partial y},\ v^* = \frac{\partial \psi^*}{\partial x}. \tag{2.71}$$

Equations (2.69) and (2.67) show that the meridional flux of potential vorticity by the waves, which is equivalent to divergence of the Eliassen-Palm flux, leads to changes in the zonal mean zonal wind. The quantity $[v^*q^*]$ is also related to the wave activity density (A) through the relation:

$$\frac{\partial [A]}{\partial t} + p[v^*q^*] = S \tag{2.72}$$

where

$$A = \frac{1}{2}p\frac{q^{*2}}{\partial Q/\partial y}$$

Q is the background potential vorticity and S is the non-conservative sources and sinks of A. The wave activity density is a measure of the amplitude of the wave and its flux, given by $\mathbf{F}$, is used to understand the interactions between waves and the mean flow as well as the propagation characteristics of waves throughout the atmosphere. However, the fact that this flux is a zonally averaged quantity means that it cannot be used to gain information about the zonal propagation of waves. To amend this, Plumb (1985) derived a conservation relation for wave activity for quasi-geostrophic stationary waves on a zonal flow which is locally applicable and, therefore, a three-dimensional extension of the generalised Eliassen-Palm flux. His conservation relation for wave activity density is given by:

$$\frac{\partial A}{\partial t} + \nabla \cdot \mathbf{F_p} = S. \tag{2.73}$$

$\mathbf{F_p}$ is now the three-dimensional flux of A from stationary waves and will be explicitly defined later. An important property related to conserved quantities that are quadratic in wave amplitude, such as A, is their relation to the group velocity vector. Plumb (1985) showed that, under the WKB approximation, the stationary Plumb flux is parallel to the group velocity vector. This means that, since the group velocity indicates the direction of energy transport by the waves (Hayes, 1977), by diagnosing the sta-

tionary Plumb flux vector it is possible to visualise the source regions, propagation and dissipation of energy by stationary Rossby waves in the atmosphere. The focus on stationary waves, rather than transient atmospheric motions, will become apparent in chapter 6.

The wave activity flux diagnostics used in chapter 6 for stationary waves are calculated using (5.7) of Plumb (1985), which is an extension from the beta-plane to spherical geometry, and is given by:

$$\mathbf{F_p} = \frac{1}{2} p \cos\phi \begin{bmatrix} v^{*2} - \frac{\psi^*}{a\cos\phi}\frac{\partial v^*}{\partial\lambda} \\ -u^*v^* + \frac{\psi^*}{a\cos\phi}\frac{\partial u^*}{\partial\lambda} \\ \frac{f}{S}[v^*T^* - \frac{\psi^*}{a\cos\phi}\frac{\partial T^*}{\partial\lambda}] \end{bmatrix} \tag{2.74}$$

after using the hydrostatic relation ($\frac{\partial\psi^*}{\partial z} = RT^*/Hf$) and the definition of the streamfunction $(u^*, v^*) = -\frac{1}{a\cos}\frac{\partial\psi^*}{\partial\phi}, \frac{1}{a}\frac{\partial\psi^*}{\partial\lambda}$. In (2.74), $S = \frac{\partial\hat{T}}{\partial z} + \frac{\kappa\hat{T}}{H}$ is the static stability, $\hat{T}$ indicates an average over the area north of 20N and $\kappa = R/c_p$. (2.74) is calculated from the climatological values averaged over the length of the integration of u^*, v^*, T^* and ψ^* on pressure levels. The zonal and meridional derivatives are calculated as in (2.61) and (2.62), respectively.

Chapter 3

Models and data

The empirical results presented in chapters 4, 5 and 6 are based on data from a variety of existing and purpose generated sources. The general features of the models and data as well as the reasons for using them are described below.

3.1 Models

3.1.1 Met Office Unified Model

Experiments are performed with the Met Office Unified Model (MetUM) over a variety of different horizontal resolutions, time periods and setups. These range from global simulations at low horizontal resolutions to Limited Area modelling simulations at very high horizontal resolutions. This is a testament to the flexibility of the model and is in line with the 'seamless' approach taken by the Met Office. Their ethos is that, since the evolution of the weather and climate involve the same physical processes and the climate can be seen as the sum of weather phenomena (Brown et al., 2012), one can trace the evolution of error growth from short to long timescales and from high to low resolutions, a feature that is exploited in both chapters 4 and 5. There are also disadvantages to the seamless approach as a result of compromises that must be made on both complexity and parameter choices, the consequences of which are also discussed in chapter 4.

The model employs a semi-Lagrangian dynamical core, is non-hydrostatic and discretises the momentum, thermodynamic, mass continuity and moisture equations in

grid point space and accounts for unresolved processes through a variety of parameterization schemes. The model dynamics are fully described in Staniforth et al. (2006). The model is used operationally for numerical weather prediction (NWP) as well as making up part of the CMIP5 model ensemble.

All of the experiments performed with the MetUM are atmosphere-only experiments and the sea surface temperatures, sea-ice, land surface and radiation are prescribed from historical values.

3.1.2 ECMWF IFS

Output from experiments performed by Irina Sandu (ECMWF) using the European Centre for Medium Range Weather Forecasts Integrated Forecasting System (ECMWF IFS) (see the ECMWF 2016 documentation for details of the model formulation) is analysed in both chapters 4 and 5. This model is used as a point of comparison with the MetUM since it employs a hydrostatic spectral dynamical core and accounts for its resolved and unresolved orography differently.

The experiments performed with the ECMWF IFS are atmosphere-only experiments and sea surface temperatures, sea-ice, land surface and radiation are prescribed.

3.1.3 CanAM4

The fourth generation Canadian Atmospheric Model (CanAM4) is a general circulation model developed by the Canadian Centre for Climate modelling and analysis (CCCma). It is dedicated to climate research and its components are described in von Salzen et al. (2013). Relevant specifics of the model include: its orographic gravity wave drag parameterization, which is formulated as in Scinocca and McFarlane (2000); its dynamical core, which makes the hydrostatic approximation and computes horizontal advection in spectral space; and its resolution, which is at spectral truncation T63. The fact that this model makes use of three different parameterized orographic drag components makes it fit for our purposes. Furthermore, its relatively low resolution means that long time integrations can be performed.

The CanAM4 experiments analysed in chapter 6 are atmosphere-only experiments in which the sea surface temperatures (SSTs), sea-ice and land-surface boundary conditions are prescribed. The values for these boundary conditions are generated from cou-

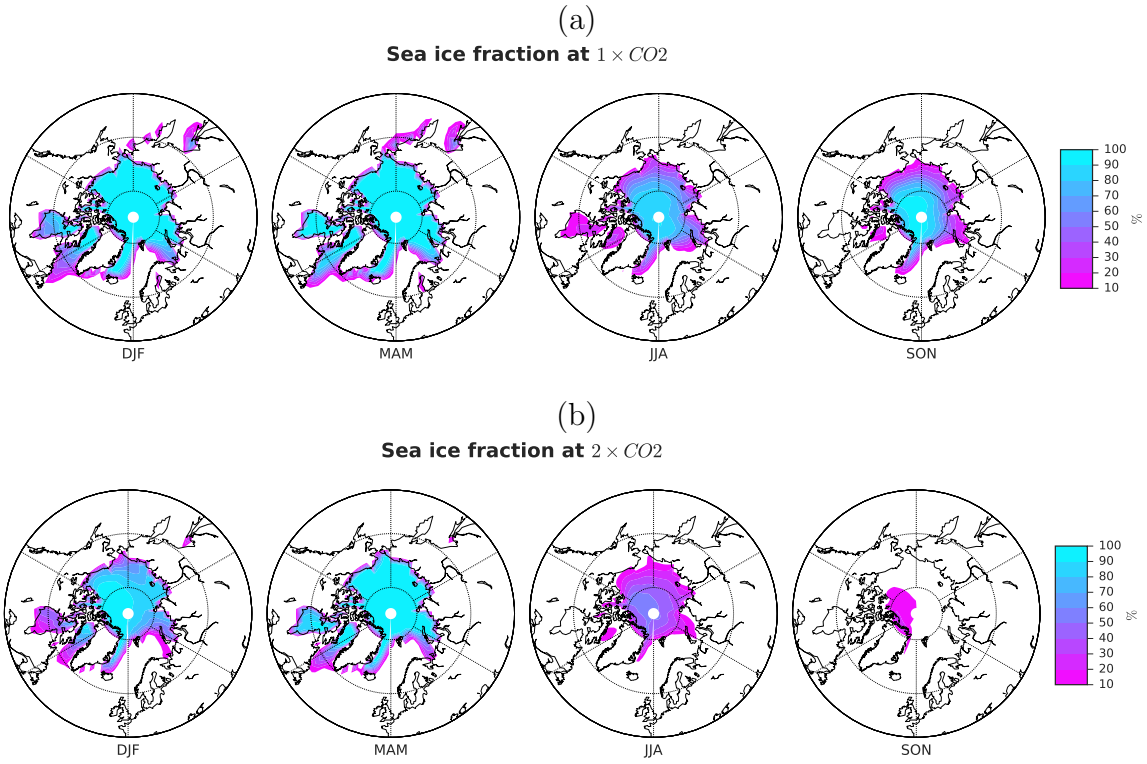

Figure 3.1: (a) Prescribed sea-ice fraction (as a %) at $1 \times CO_2$ and (b) $2 \times CO_2$ for experiments described in chapter 6

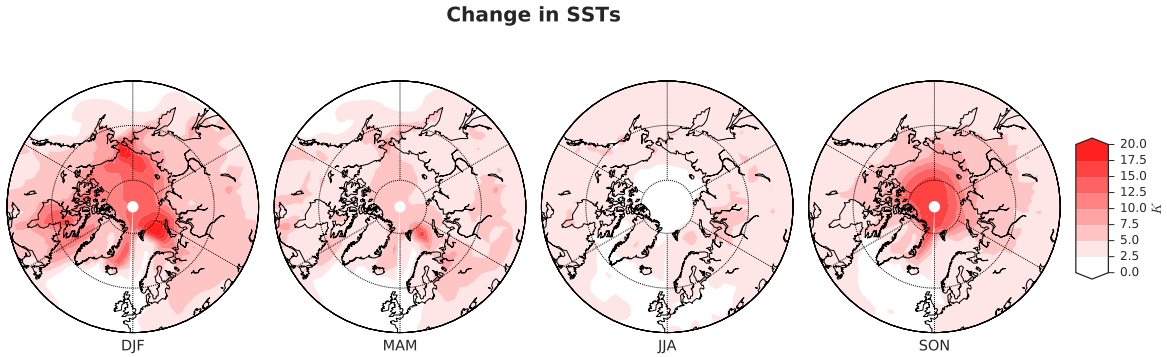

Figure 3.2: Sea-surface temperature change due to climate change (SSTs at $2 \times CO_2$ minus $1 \times CO_2$).

pled experiments that are performed with the Canadian Earth System Model (CanESM). There are two types of experiments performed. The first are referred to as $1 \times CO_2$ experiments, in which the CO_2, sea-ice and SSTs correspond to pre-industrial values. The second are referred to as $2 \times CO_2$ experiments, in which the CO_2 is doubled relative to pre-industrial values. Figures 3.1(a) and 3.1(b) show the values of the seasonal mean of the sea ice fraction, as a %, that is generated from the coupled experiments and are prescribed in the $1 \times CO_2$ and $2 \times CO_2$ atmosphere-only experiments, respectively. Figure 3.2 shows the corresponding change in prescribed seasonal mean SSTs that result from doubling CO_2. Note that the SST perturbations maximise and are located closer to the midlatitudes during the winter months (DJF). The analysis in chapter 6 is, therefore, focussed on the responses during the NH winter, since this is when the climate change signal maximises over the NH.

3.2 Analysis and reanalysis

3.2.1 Met Office operational analysis

Being an operational meteorological centre, the Met Office perform 6-hourly data assimilation cycles. They employ a 4-dimensional variational data assimilation system, whereby available observations and model output are used to derive a best-guess estimate of the atmospheric state, known as the analysis (Rawlins et al., 2007). This is used operationally to initialise the model for numerical weather prediction. In chapter 4 Met Office analysis is used to initialised the forecasts performed with the MetUM over the month of December 2015. In chapter 5 archived Met Office analysis data is used to initialise and assess the drift in the global and limited area short range forecasts that are performed with the MetUM.

3.2.2 ECMWF operational analysis

In chapter 4 ECMWF analysis is used to initialise the short-range forecasts performed with the MetUM over the month of January 2010. The ECMWF analysis is used instead of the Met Office analysis due to a lack of data availability during the time period required for comparison. As with the Met Office analysis, the ECMWF operational analysis is generated from the model and observations using a 4-dimensional data

assimilation system (Dee et al., 2011). The experiments performed with the ECMWF IFS in chapters 4 and 5 are also initialised with ECMWF analysis.

3.2.3 ERA-interim reanalysis

In chapter 4 the thermodynamic and dynamic variables within the MetUM are relaxed towards that of the ERA-interim re-analysis (Dee et al., 2011) as a means of constraining the large scale circulation and to diagnose model error. Additionally, December, January and February ERA-interim wind fields over the period of 1979 to 2016 are used in the validation of CanAM4 in chapter 5.

Chapter 4

Sensitivity of resolved and parameterized surface drag to changes in resolution and parameterization

The work in this chapter, excluding the comparison with a second model in section 4.4, has been published in van Niekerk et al. (2016) and is reproduced essentially unaltered here.

4.1 Introduction

The attribution of systematic errors can be especially difficult in climate models compared to numerical weather prediction, since we do not have the daily assimilation of data with which to validate the models directly. Comparison of global climate models at different resolutions becomes computationally expensive and problematic when long time integrations must be produced in order to determine model climatology. Even if we are able to compare long time integrations, the feedbacks that act in response to model errors mean that parameterizations are fed with unrealistic climatological states, making it difficult to disentangle model biases (Phillips et al., 2004). Although it may be possible to reduce model error at all resolutions as a result of the seamless modelling approach (Martin et al., 2010), the errors at lower resolutions may remain large and undetected, leading to a false sense of security about the quality of models

at lower resolutions. It is, therefore, important to evaluate models at low resolutions and the scaling of error with resolution.

The drift in short range forecasts has been used in previous studies to evaluate model error (Klinker and Sardeshmukh, 1992; Pope and Stratton, 2002; Brown, 2004): since the model is constrained by initial conditions from observations, this technique is useful for resolution and parameter sensitivity studies. However, performing such analysis can be difficult without access to operational infrastructure. A more accessible means of eliminating model feedbacks and constraining the model climatology is to relax the dynamic and thermodynamic variables towards analysis or reanalysis. Relaxation has been a popular method of diagnosing the influence of certain regions and their teleconnections (Jung, 2011; Hoskins et al., 2012), as well as being widely used in the chemistry and aerosol community as a method of reproducing the observed meteorological state of the atmosphere (van Aalst et al., 2005; Shepherd et al., 2014). Spectral nudging has also been used in regional climate modelling to address the problem of lateral boundary condition resolution mis-match, in which only the large scale fields within the RCM are nudged towards the driving GCM (Waldron et al., 1996; von Storch et al., 2000). This chapter seeks to investigate the sensitivity of surface torques to model resolution and parameterization using the nudging approach, in the hope that this will motivate further sensitivity studies and inter-model comparisons employing this method.

As well as introducing the nudging framework as a method of surface drag validation and systematic error identification, this chapter addresses the fundamental issue of orographic drag resolution and parameterization sensitivity and the modelling uncertainties they introduce.

The structure of this chapter is as follows. Section 4.2 describes the model setup, nudging sensitivity experiments, analysis and verifications against short range forecasts. The exchange between parameterized and resolved orographic torques with changes in resolution is discussed in section 4.3. Section 4.4 makes a comparison with the European Centre for Medium Range Weather Forecasts Integrated Forecasting System (ECMWF IFS). The impact of orographic drag on model bias is discussed in section 4.5. Section 4.6 looks at the compensation that occurs between the parameterized orographic torque, the boundary layer torque and resolved orographic torque when blocking is switched off. Finally, conclusions are drawn in section 4.7.

4.2 Methodology

The role of orographic torque in the momentum budget of the atmosphere is investigated using the Met Office Unified Model (MetUM) with the ENDGame dynamical core and Global Atmosphere 6 components integrated at resolutions N96 (130 km), N216 (60 km) and N512 (25 km), all of which have 85 terrain-following vertical levels extending to $85km$. The integrations were set up in an AMIP-style configuration with prescribed SSTs and sea-ice concentrations and were initialised from the same N96 initial fields. Details of the orographic blocking and gravity wave drag parameterizations can be found in appendix A of Vosper (2015) and are based on the blocking scheme of Lott and Miller (1997) and gravity wave saturation scheme of McFarlane (1987). See further discussion in chapter 2.1. As is desirable in a seamless modelling approach, the physics parameters are held constant across all three resolutions with values chosen based on the standard climate and global forecast configurations. The orographic drag parameterization has three free parameters that are poorly constrained by observations: the critical Froude number (set at $F_c = 4$), which determines the amount of blocking such that a higher value leads to increased blocking; the mountain wave amplitude (set at $G = 0.5$); and the flow blocking drag coefficient (set at $C_d = 4$). It is worth emphasising that the $C_d = 4$ value chosen in the MetUM is very large in the context of fluid dynamic theory and is indicative of a compensation of error, model tuning or a lack of theoretical understanding or observational constraint of orographic drag processes in the real atmosphere. The parameterization adjusts to the model resolution based on statistical aspects of the sub-grid scale orography, such as the standard deviation, slope and anisotropy, that are recalculated from a $1km$ resolution dataset at each resolution (Webster et al., 2003). As model horizontal resolution increases, the sub-grid orographic standard deviation and slope reduces across the major mountain regions and, since the parameterized orographic blocking and gravity wave drag are proportional to these, the parameterized orographic drag is expected to reduce with increasing resolution.

4.2.1 Experimental design

The framework of the angular momentum budget is a powerful tool for examining the contribution of surface drag to the large scale structure of the circulation. The vertically

integrated, zonally averaged axial component of the relative angular momentum of the atmosphere, $m = ur\cos\phi$, in the non-hydrostatic version of the MetUM is given by (Staniforth et al. 2006, see also chapter 2.3.1):

$$\begin{aligned}\frac{\partial\left[\int_{z_0}^{\infty} m\rho dz\right]}{\partial t} = -\frac{1}{r\cos\phi}\frac{\partial\left(\left[\int_{z_0}^{\infty} mv\rho dz\right]\cos\phi\right)}{\partial\phi} \\ -\left[\int_{z_0}^{\infty} 2\Omega wr\cos^2\phi\rho dz\right] + \left[\int_{z_0}^{\infty} fvr\cos\phi\rho dz\right] \\ -\left[p_0\frac{\partial z_0}{\partial\lambda}\right] - [F_0 r\cos\phi]\end{aligned} \tag{4.1}$$

where u is the zonal wind, v is the meridional wind, ρ is the atmospheric density, z_0 is the surface elevation, p_0 is the surface pressure, r is the height dependent radius of the Earth, ϕ is latitude, Ω is the rate of rotation of the Earth, f is the Coriolis parameter, F_0 is the surface stress from the parameterized processes and square brackets indicate a zonal average. The terms on the right hand side of the momentum equation are, from left to right: the angular momentum flux convergence (AMFC), which represents the angular momentum being advected into and out of a particular latitude band; the torque due to the non-hydrostatic component of the absolute angular momentum; the torque due to the Coriolis force; the resolved mountain torque (RES); and the parameterized sub-grid scale surface torques. Since the non-hydrostatic component and the Coriolis torque terms are negligible in the steady state limit, the dominant balance in this limit is between the surface terms and the AMFC. By constraining the AMFC at each model resolution through nudging, it is possible to determine the contributions of the resolved and individual parameterized surface terms towards balancing the AMFC.

The model's u, v and T (temperature) fields are relaxed towards the ERA-interim reanalysis variables (Dee et al., 2011) on terrain-following model levels within the altitude regions of maximum AMFC (Hartmann, 2007), above ∼700hPa, while allowing the low level flow to evolve freely. Nudging on terrain-following model levels means that the nudging will be applied at higher altitudes over orography. The nudging is applied through a Newtonian relaxation of the form (Telford et al., 2007):

$$X_F^n = X_M^n + \frac{\Delta t}{\tau}(X_A^n - X_M^n) \tag{4.2}$$

where $X = (u, v, T)$, τ is some relaxation timescale and the superscript n denotes the value at the current time-step. The subscripts are as follows: F denotes that the value is taken as the final variable after nudging; M denotes the variable before nudging but after the model dynamics and physics; and A denotes the variable from the ERA-interim reanalysis. The reanalysis comes from 6 hourly instantaneous values that have been linearly interpolated to the model time-step. The reanalysis data is spatially interpolated from a resolution of $\sim$50 km (N240) to the respective model resolutions using the reconfiguration package within the MetUM.

4.2.2 Nudging sensitivity experiments

If a systematic bias were present in the MetUM relative to the reanalysis, this would require a non-zero time mean zonal mean nudging to be applied within the free atmosphere. In accordance with the downward control principle (Haynes et al., 1991), this nudging could induce a meridional circulation extending to the surface below the nudged region and, since the strength of the nudging would change with resolution and parameter settings, the induced circulation and surface flow could also change. This would imply that different model configurations may have different surface flows that are not purely a response to the AMFC alone. Hitchcock and Haynes (2014) showed that the circulation induced from nudging of the zonal mean winds and temperatures was confined within the region of nudging. This alleviates concerns of spurious circulations occurring within the unnudged region in our experimental setup.

Several nudging sensitivity experiments were performed in order to determine appropriate parameter choices, such as the relaxation height, relaxation timescale and spin-up time. The ability of the nudging to constrain the model's low level flow through the AMFC was assessed by varying these parameters and looking at the evolution of the low level zonal winds between 30N and 50N. This region was chosen since it is likely to be the most problematic area for the low-level flow to be constrained as a result of differences in mean orography and parameterized drag across resolutions. The chosen periods for analysis were January 1998 and January 2010, with all nudging sensitivity experiments performed over the January 1998 period. It is worth mentioning that the model wind does not have the exact same amplitude as the ERA-interim wind due to the fact that the model has slightly different topography over this region and, as a result, different pressure levels near the surface. Overall, the low level winds

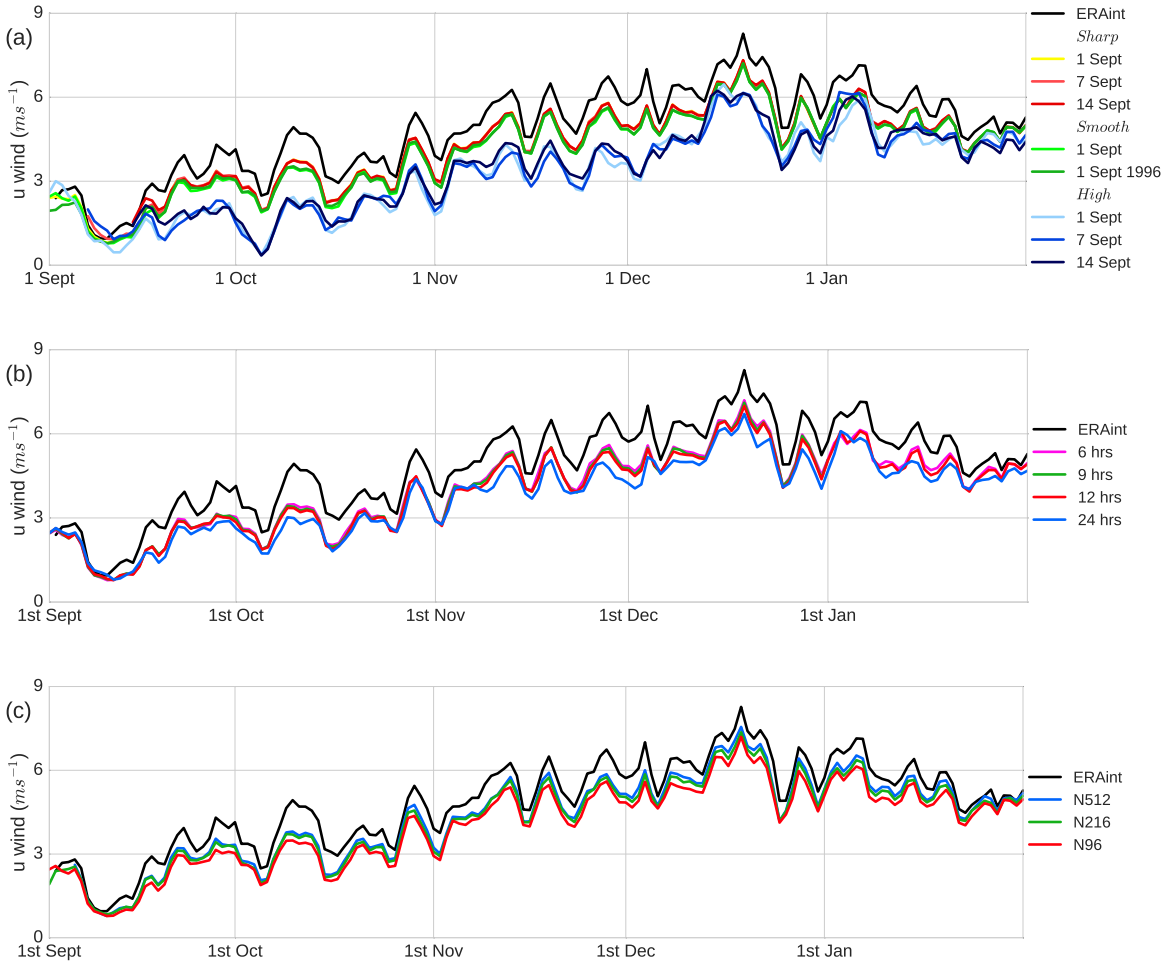

Figure 4.1: Time-series of the zonal mean zonal wind at 850hPa averaged between 30°N and 50°N over late 1997 and early 1998 for (a) experiments of varying nudging heights and smoothing over model levels initialised from different start dates (see section 4.2.2), (b) different nudging timescales (τ) and (c) resolutions N96, N216 and N512. In (a) *Sharp*, *Smooth* and *High* indicate experiments with smoothing over 2 model levels starting at model level 20, smoothing over 10 model levels starting at model level 20, and smoothing over 10 model levels starting at model level 30, respectively.

are less sensitive to initial conditions, nudging parameters and nudging height over the Southern Hemisphere (SH) mid-latitudes compared with the Northern Hemisphere (NH) mid-latitudes (not shown) but, as will be shown in the sections to follow, the final nudging parameters chosen give well constrained low-level winds even in the NH mid-latitudes relative to ERA-interim.

Nudging spin-up sensitivity

The spin-up time, initial-condition sensitivity and model drift were tested by initialising from five different start dates of the same free-running model. Figure 4.1a shows time series of the zonal mean zonal wind at 850hPa averaged between 30N and 50N for experiments with different nudging profiles initialised from the following start dates: the 1st of September 1996 (1 year and 4 months spin up); 1st of September 1997 (4 months spin up); 7th of September 1997 (3 months and 3 weeks spin up); and finally the 14th of September 1997 (3 months and 2 weeks spin up). For nearly all cases, the surface winds responded quite rapidly to the nudging and were very similar to the ERA-interim winds within about 4 days of initialisation. What is more, the longer spin-up period matched the reanalysis winds even after a year, indicating that there is little drift in the nudged model.

Nudging height and smoothing

As a test for imbalances at the nudging boundaries (i.e. regions directly below the nudging height) the smoothing of the nudging over terrain-following model levels was adjusted such that the strength of the nudging was linearly increasing with height over either 10 model levels or 2 model levels, starting at the 20th model level ($\sim 3km$ or 700hPa). From the vertical structure of the winds and temperatures (not shown), the 10 level smoothing was indistinguishable from the 2 level smoothing. Figure 4.1a shows the time series of the zonal mean zonal wind at 850hPa averaged between 30N and 50N for the experiments with 10 level smoothing ($Smooth$), and 2 level smoothing ($Sharp$) with different initial conditions. The 10 level smoothing and 2 level smoothing are almost indistinguishable. What is more, they are insensitive to initial conditions and follow the ERA-interim winds well. The 10 level smoothing was chosen due to the fact that the nudging terms were strong at the boundary of the 2 layer smoothing and any sudden discontinuities that may cause spurious imbalances in the model are to be

avoided.

The impact of nudging outside of the maximum AMFC region and the sensitivity of the surface winds to this aspect of the nudging was investigated. When applying smoothed nudging starting from the 30th model level ($\sim 7km$ or 400hPa) to full nudging at the 40th model level ($\sim 12km$ or 200hPa), the surface winds from ERA-interim were not accurately reproduced. Figure 4.1a shows that the experiments with nudging started at $7km$ ($High$) are quite far from those of ERA-interim and show strong sensitivity to initial conditions, since the three ensemble members have varying amplitudes and phase. As a result, the nudging was applied from the 20th model level ($\sim 3km$ or 700hPa) and smoothed up to the 30th model level ($\sim 7km$ or 400hPa); this allows for the nudging to be at full strength within the maximum AMFC region.

Nudging timescale sensitivity

The relaxation timescale (τ) was varied between 6 hours, 9 hours, 12 hours and 24 hours. Changing this parameter did not appear to have much of an impact on the evolution of the low-level winds (figure 4.1b) or the spatial distribution of the nudging tendencies, although the $\tau = 24$ experiment drifts further away from the ERA-interim winds relative to other timescales. A relaxation timescale of 6 hours was chosen to ensure that the model was not able to drift too far from the reanalysis. The sensitivity experiments performed on the MetUM by Telford et al. (2007) also suggest that this is the optimal choice for τ, given the temporal frequency of the reanalysis.

4.2.3 Momentum budget analysis

In our analysis of the MetUM momentum budget, (4.1), the tendency approach to closing the momentum budget was taken, which involves adding together all tendencies that contribute towards the total zonal wind tendency. Since the MetUM uses a semi-Lagrangian upwind advection scheme (Diamantakis et al., 2007), it can be problematic to calculate the momentum flux convergence term (first term on RHS of (4.1)) in a way that is consistent with the model numerics. As a result, the tendency due to semi-Lagrangian advection was output as 6 hourly instantaneous values on model levels and vertically integrated. It was then possible to deduce the angular momentum flux convergence term as a residual, by subtracting the middle three terms on the RHS

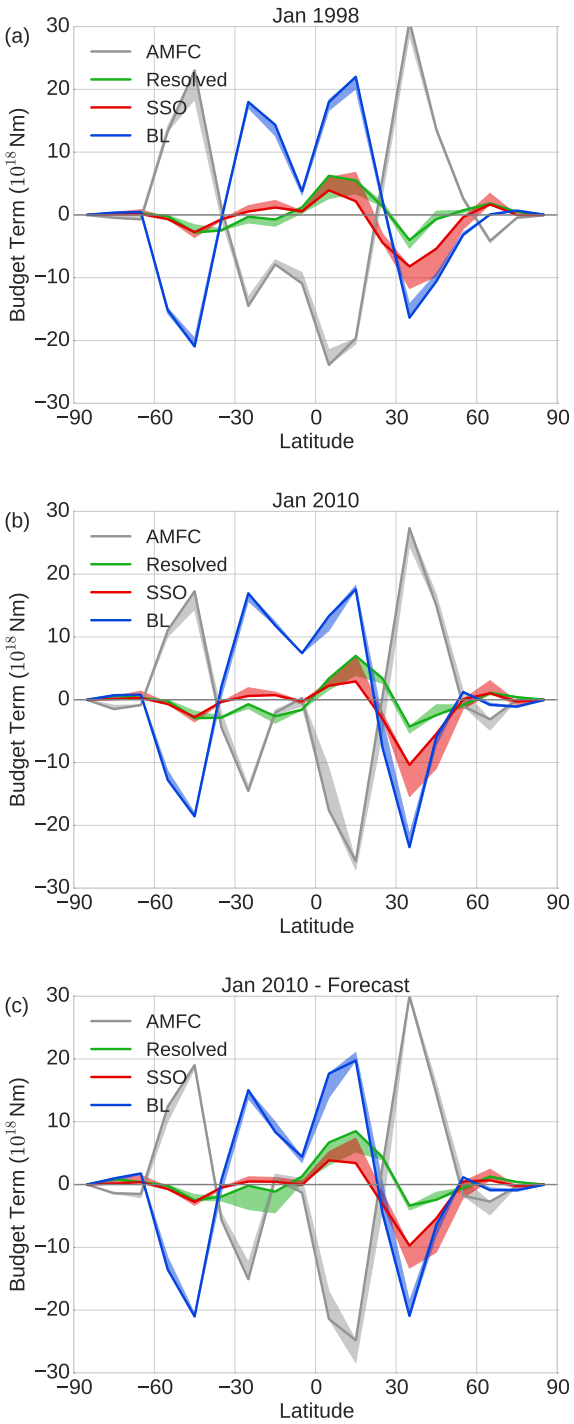

Figure 4.2: Dominant terms in the relative angular momentum budget (4.1) integrated over 10° latitude bands and averaged over the (a) January 1998, (b) January 2010 nudged experiments and (c) January 2010 short range forecast experiments. The solid line indicates the value of the N512 budget term and the shading indicates the range of the budget term over the N96, N216 and N512 resolution experiments.

of equation 4.1 from the advection tendency. The non-hydrostatic and Coriolis terms were calculated offline from 6 hourly values of w and v. The resolved mountain torque term was calculated both online and offline using various different methods including calculating the horizontal pressure gradient ($\partial p/\partial \lambda$) and vertically integrating, which, reassuringly, gave the same result as the online calculation. As in Huang and Weickmann (2008), this term was found to be sensitive to the differencing scheme used, and a centred difference scheme calculated online allowed us to close the angular momentum budget to within a negligible amount.

The $F_0 r \cos\phi$ term in (4.1) includes the vertically integrated tendencies from the following parameterizations: the boundary layer turbulent drag (BL); the sub-grid scale orographic drag (SSO), including gravity wave drag and blocking; the spectral gravity wave drag (which integrates to zero at the surface); the convective entrainment of momentum; and the tendencies generated from the nudging routine. All contributions to the $F_0 r \cos\phi$ term were calculated from 6 hourly instantaneous tendencies from parameterizations on 85 model levels.

Figures 4.2a and 4.2b show the dominant terms in the angular momentum budget averaged over January 1998 and January 2010 for the three nudged resolution experiments. Each term has been integrated over 10° latitude bands in order to make the resolutions comparable. The solid lines are the values for the N512 experiments and the shading shows the range between the three different resolutions. The width of the shaded region, therefore, indicates the extent of change with resolution of that particular term. The sign of the terms are such that a positive (negative) value contributes towards an acceleration (deceleration) of the atmosphere and a decrease (increase) in the Earth's angular momentum. The magnitude and latitudinal distribution of the terms match closely those of Brown (2004) and Huang et al. (1999), although they use a different sign convention. The resolutions used by Brown (2004) are T95, T159, T255 and T511, which corresponds to approximately 210, 125, 80 and $40km$, respectively, making the MetUM N96 and N216 comparable to their T159 and T255. There is disagreement in the sign of the parameterized and resolved torques between 20N and 30N, as was found in their studies, but, unlike them, this is also seen between 10S and 30S in these experiments. This suggests that there are large scale phenomena that impact the resolved pressure torques and not the parameterized torques, since the sign of the parameterized drag depends only on the sign of the grid-box mean winds. This can be problematic for determining the correct total orographic torque in these regions, since,

theoretically, either term can go to any magnitude in the opposite sign and still give the same total.

The angular momentum balance between the atmospheric torque and surface torque is larger in the NH than in the SH due to both the asymmetry of the land and the fact that in NH winter there is an enhanced midlatitude jet, which would interact strongly with the prominent orography in those regions. The torque coming from the boundary layer drag is the major contributor towards balancing the torque coming from the AMFC, since it acts over both land and ocean. Comparing the two years, there is a shift in the contributions to the budget between the boundary layer and the AMFC over the tropics in the region 0S to 20S. This may be due to the fact that January 1998 experienced a particularly strong El Niño, which would lead to redistribution of the mass in the atmosphere and, as a result, have a substantial influence on the angular momentum of both the atmosphere and the solid Earth (Chao, 1988). It is interesting to note that while both the BL torque and SSO torque are substantially larger over the NH extra-tropics in January 2010 compared with January 1998, the resolved orographic torque is relatively unchanged. This provides additional evidence that the resolved torques respond differently to the surface flow than do the SSO or BL torques.

4.2.4 Verification against forecasts

As a further means of verifying our method of constraining the climatology and reducing the variability in the AMFC between experiments of different resolutions, 31 short range forecasts initialised from ECMWF analysis at 00UTC for the month of January 2010 were performed. The idea is to confirm that the sensitivity of the resolved and parameterized torques to model resolution is not somehow connected to the nudging itself. These forecast experiments were performed using the same model setup, model physics and model resolutions as with the nudging experiments. The only difference between them is that the forecasts are run with 70 model levels extending to $80km$ instead of 85 model levels extending to $85km$, since the former is the standard global forecasting setup. Figure 4.2c shows the dominant terms in the angular momentum budget for the forecast experiments performed over January 2010, with the shading indicating the range over the three model resolutions as in figures 4.2a and 4.2b. Comparing the January 2010 forecast to its nudging counterpart, the overall shape of the

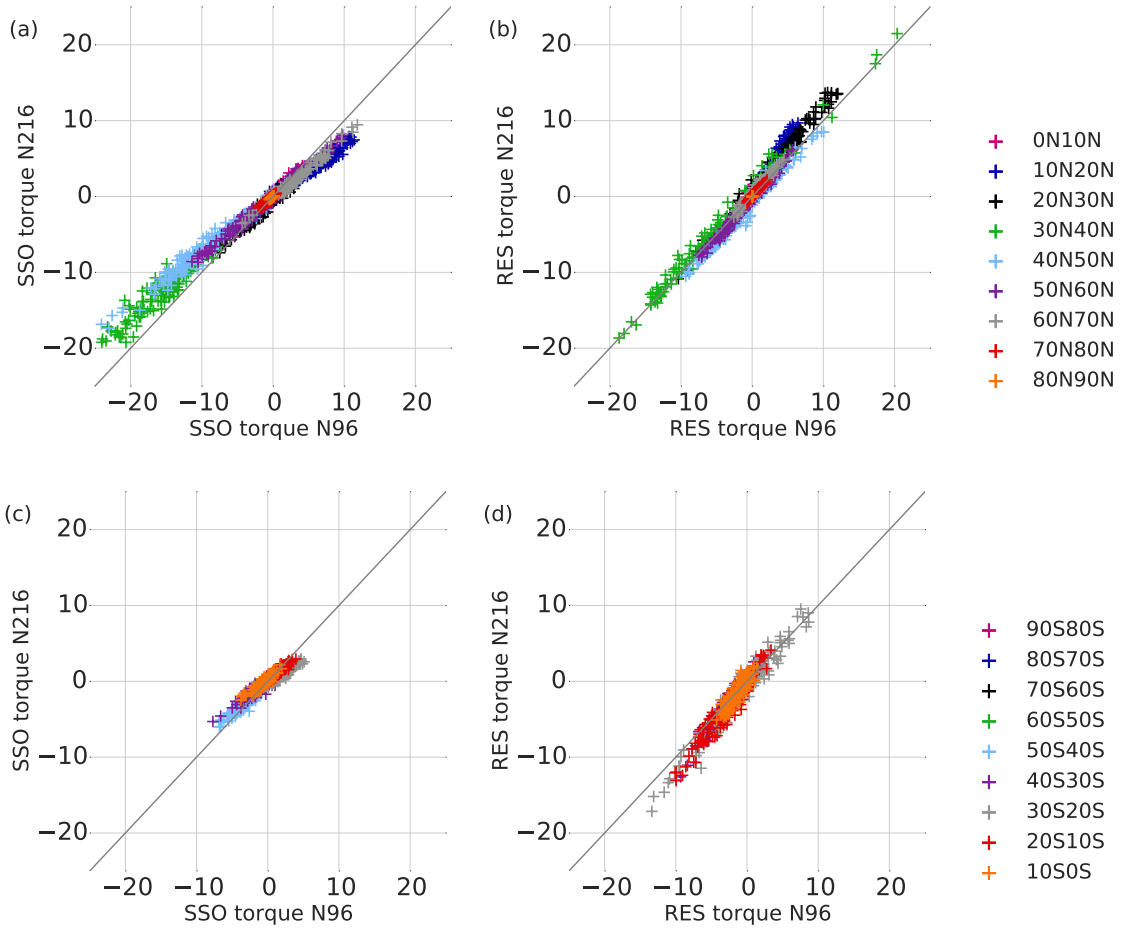

Figure 4.3: Scatter plots of (a),(c) sub-grid scale orographic (SSO) torques and (b),(d) resolved orographic torques for nudged experiments at resolutions N96 vs N216 for January 2010. Each point corresponds to a 6 hourly instantaneous value and colours indicate the 10° latitude band integrated over.

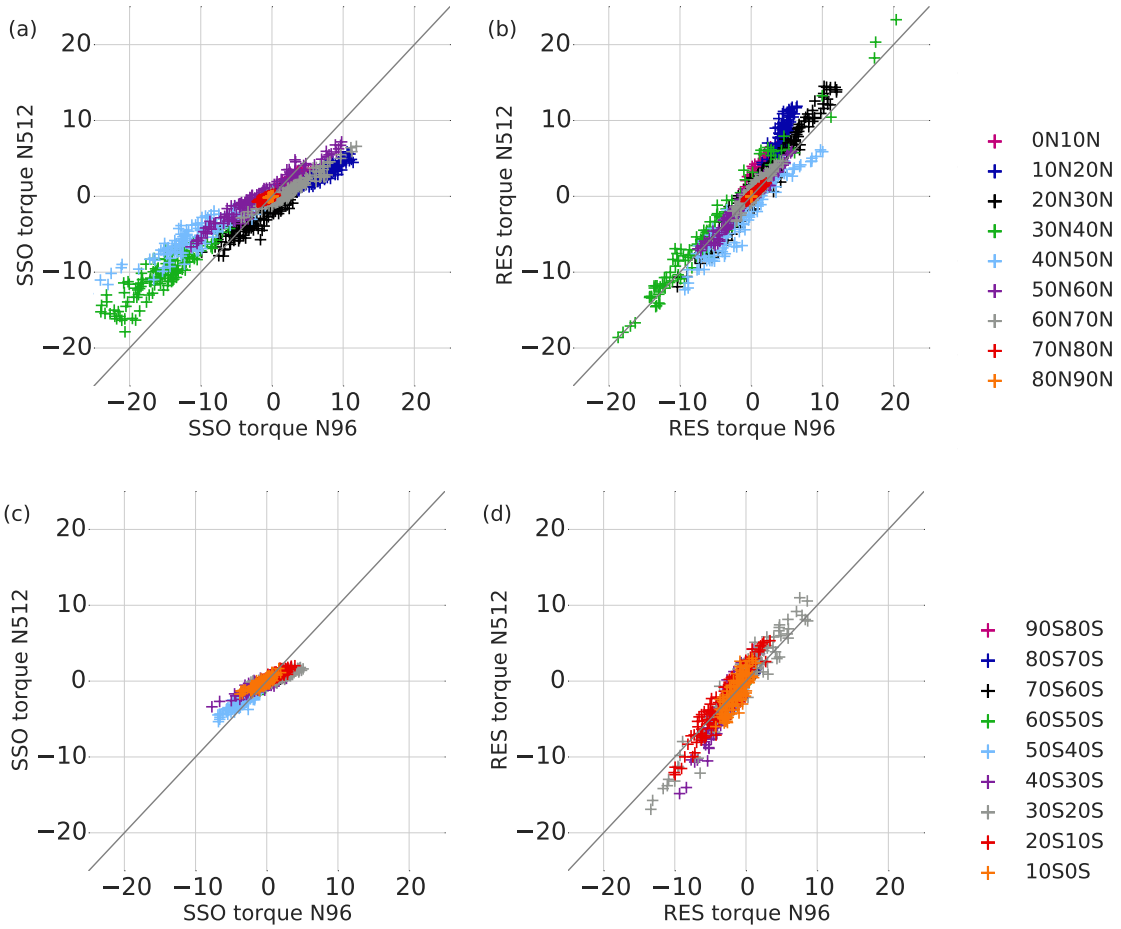

Figure 4.4: As in figure 4.3 but for resolutions N96 vs N512.

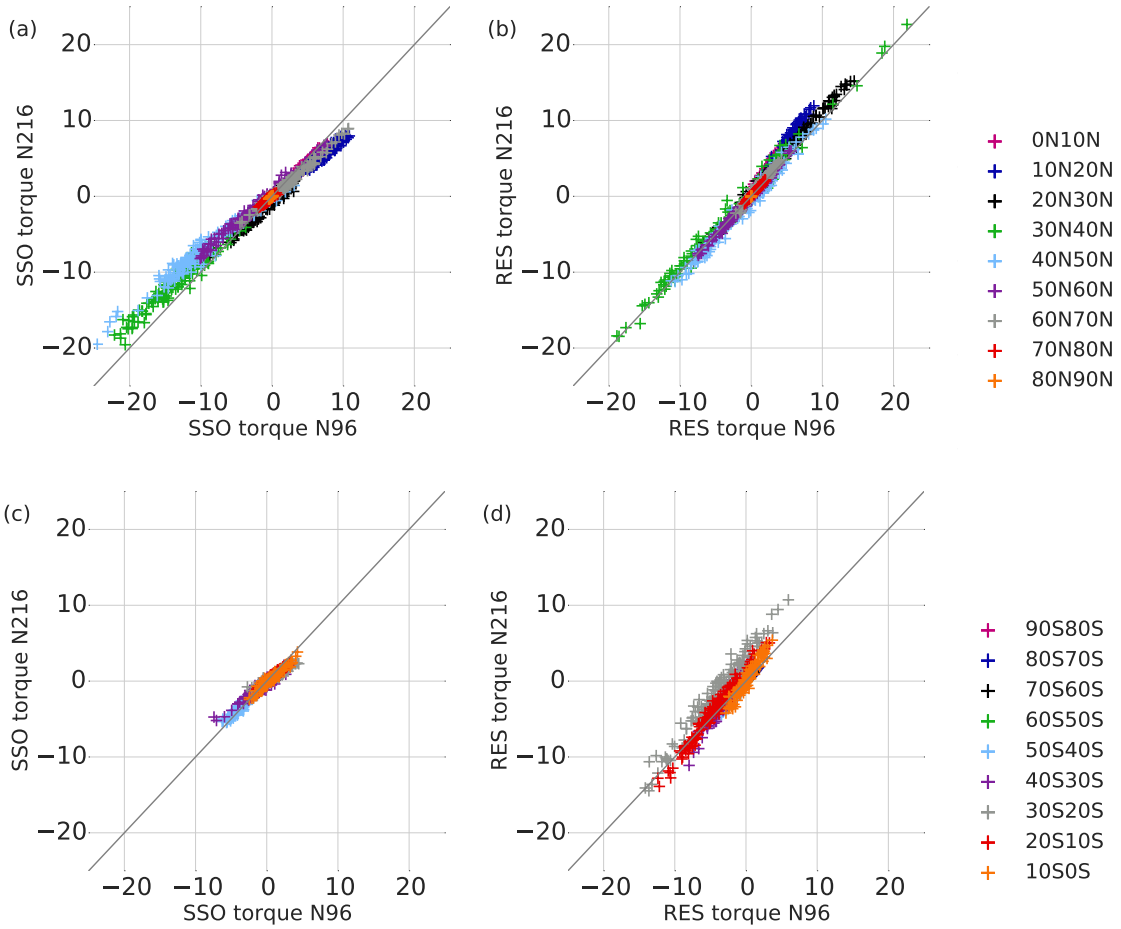

Figure 4.5: As in figure 4.3 but for the short range forecast experiments.

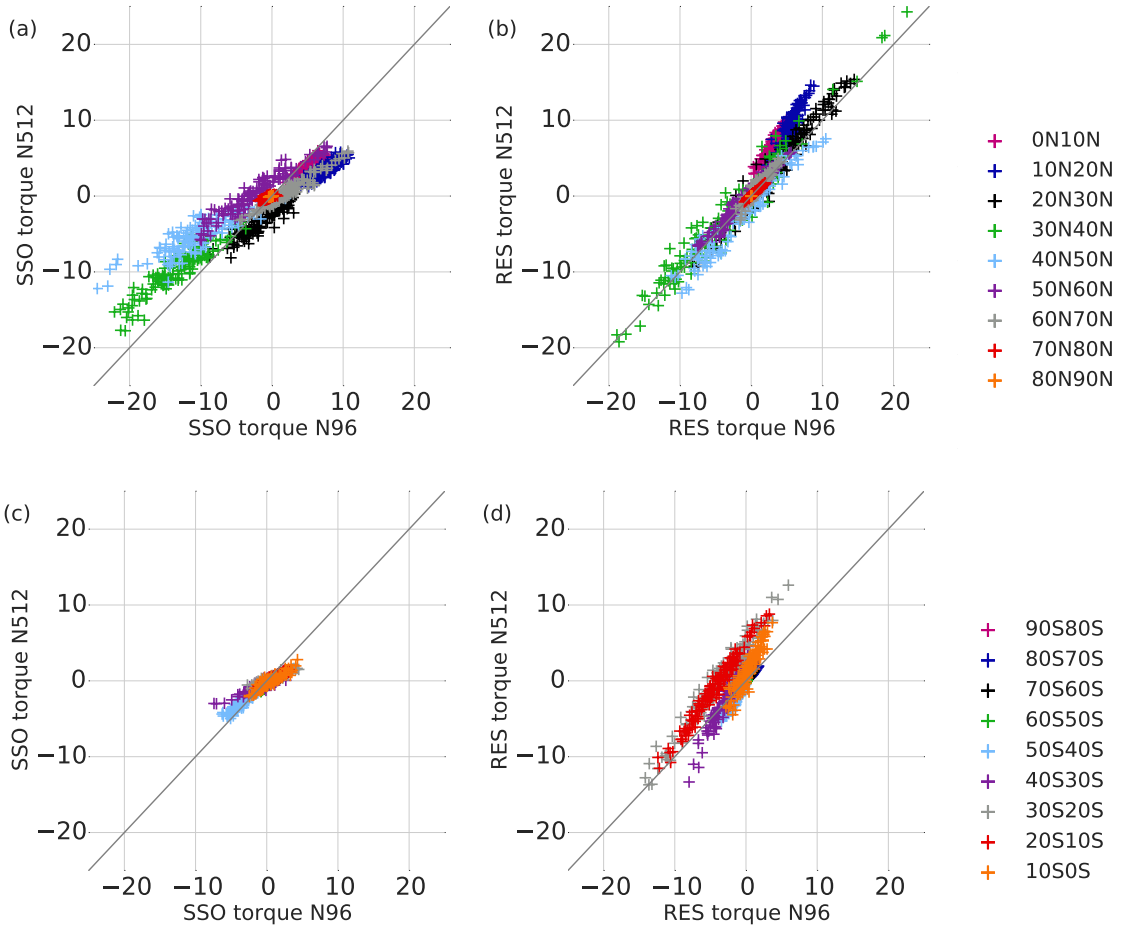

Figure 4.6: As in figure 4.5 but for resolutions N96 vs N512.

terms are relatively similar. There are some differences between the magnitude of the extrema of the AMFC and BL torques, which may arise due to differences between ERA-interim and the operational ECMWF analysis. However, the important point for our purposes is that the sensitivity of the different terms to horizontal resolution is very similar.

4.3 Sensitivity to model resolution

The shape, sign and maxima of the AMFC term does not change much across the three resolutions in figure 4.2. Along with the fact that the lower tropospheric winds at all three resolutions adjust to the ERA-interim winds (figure 4.1c), the similarity in the AMFC terms is a further indication that the nudging is constraining the climatologies at the different resolutions. Since the BL drag parameterizes scales smaller than $5km$, and we are not resolving those even at the highest resolution considered, the magnitude of this term sees little change between the resolutions. The parameterized SSO torque, however, varies substantially between the resolutions, most notably in the 30N to 60N and 0N to 20N regions, where it drops by more than a quarter between the N96 and N512 resolutions. Although there is an increase in the magnitude of the resolved torque to balance that of the decreasing SSO torque in the 0N to 20N region, there is very little change in the resolved torque relative to the SSO torque elsewhere. This resolution sensitivity is evident in both years shown in figure 4.2, as well as in the forecast experiments. Offline calculations of the blocking component of the SSO torque, when holding static stability, zonal wind and density constant across resolution, show a similar resolution sensitivity to that seen in the full model experiments (not shown). This suggests that, while static stability and zonal wind changes may play some role, it is the sub-grid orographic parameters that contribute most to the resolution sensitivity.

To further illustrate the exchange between the resolved and parameterized torques, scatter plots motivated by figure 3 in Brown (2004) of the orographic torques at different resolutions have been plotted in figures 4.3 and 4.4 for the nudged experiments. The left hand column of figures 4.3 and 4.4 compare the N96 parameterized orographic torques on the x-axis with those of the N216 and N512 resolutions on the y-axis. The right hand column of figures 4.3 and 4.4 then compare the N96 resolved orographic torques with those of the N216 and N512 resolutions. Each point corresponds to an instantaneous

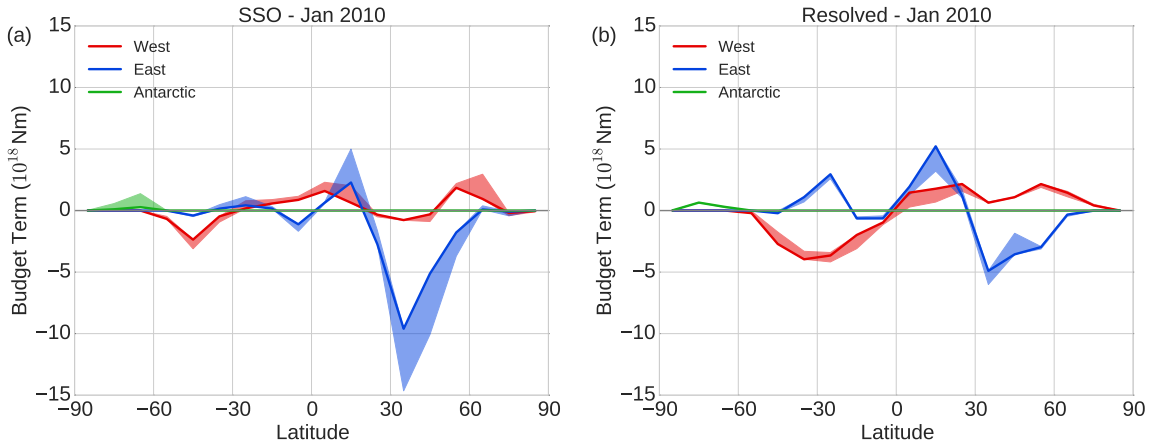

Figure 4.7: (a) Sub-grid scale parameterized (SSO) and (b) resolved orographic torques integrated over the Western Hemisphere (∼180 to ∼350 longitude, encompassing the Americas and Greenland), the Eastern Hemisphere (∼350 to ∼180, encompassing Eurasia and Africa) and the Antarctic, averaged over the January 2010 nudged experiment. The solid line indicates the value of the N512 experiment and the shading indicates the range over the N96, N216 and N512 resolution experiments.

value of the torque at 6 hourly intervals for the month of January and the colours indicate the 10° latitude band considered. In most regions of the NH, the magnitude of the resolved and parameterized torques in the N96 experiments are similar, although there is much larger variability in the resolved torque while the parameterized torque is of almost constant sign for each latitude band. The dependence of the resolved torque on differential heating and synoptic scale pressure systems passing over large topography means that there is a large variation in the sign of the resolved torque on daily timescales. The parameterization schemes, however, assume only a wind direction and static stability dependence, which is why this difference in sign between the resolved and parameterized torques over certain regions exists. This variability in the resolved torque also explains why there are smaller values of the resolved torques in the monthly mean picture, despite the instantaneous magnitude of the resolved torques being larger than the SSO torques in some instances.

The slope of the scatters in figures 4.3a,c and 4.4a,c show that there is a decrease in the magnitude of the parameterized torque with increasing resolution, as would be expected. However, figures 4.3b,d and 4.4b,d do not show a corresponding increase in the resolved orographic torque and, although some exchange is seen in the latitude

band between 10N to 30N, most of the points lie on the one-to-one line, indicating no resolution sensitivity. This implies that there is more total orographic torque, resolved plus parameterized, at lower resolutions, particularly in the 30N to 50N region. In the SH, the magnitude of the resolved torque is much larger than the parameterized torque, a feature that is not evident from the monthly mean budget plots. Compared to the NH, the SSO and resolved torques are also much smaller, since there is less land mass here and, although the torque from the Andes and the Antarctic Peninsula are substantial, they become diluted in the zonal mean. As in the NH, figures 4.3d and 4.4d shows that there is a one-to-one relationship between the resolved torques, indicating a lack of increased resolved orographic torque with increasing resolution. Figures 4.5 and 4.6 show scatter plots of the orographic torques at different resolutions, as in figures 4.3 and 4.4, but now for the experiments constrained by short range forecasts. The one-to-one relationship between the resolved torque at different resolutions in the 30N to 60N region is as evident in the forecast experiments as in the nudging experiments, as is the large reduction in the parameterized torque with increasing resolution. This confirms that this resolution sensitivity is not an artefact of the nudging and is a genuine property of the model at these resolutions. It is clear from the zonal mean scatter and momentum budget plots that each latitude responds differently to changes in resolution as a result of the circulation or orographic features in that region. Figure 4.7 shows the contribution to the zonal mean SSO and resolved torques integrated over the Eastern Hemisphere (from approximately 180 to 350 longitude), the Western Hemisphere (from approximately 350 to 180 longitude) and the Antarctic for the January 2010 nudged experiments. The integrations are performed over land masses so that the Eastern Hemisphere includes the entire African, Asian, European and Australian continents and the Western Hemisphere includes the Americas and Greenland. As resolution increases, there is very little change in the resolved torque over the Antarctic Peninsula, while the SSO torque reduces substantially. Similarly, the SSO torque becomes far less negative with increasing resolution over the Eastern Hemisphere between 30N to 60N, which encompasses the Alps, the Caucasus and the Himalayas, compared to the small increase seen in the resolved torque. The Western Hemisphere resolved and SSO torque are of opposite sign and do not change much with resolution over the Rockies between 20N to 40N. At lower latitudes, between approximately 0N to 20N, the change in the resolved and SSO torque across resolution is almost like-for-like over both the Western and Eastern Hemispheres. This latitudinal and longitudinal dependence of the resolution

sensitivity indicates that, although the parameterized and resolved orographic torques exchange well in certain regions, the different mountain massifs respond very differently and particular attention should be paid to the Eastern Hemisphere middle latitudes.

4.4 Comparison with ECMWF IFS

As part of the workshop 'Drag Processes and their links to large scale circulation' held at ECMWF in September 2016, there was a collaborative effort between Irina Sandu (ECMWF), Sylvie Malardel (ECMWF), Andy Elvidge (Met Office) and myself that set out to compare the resolution sensitivity and variability of the resolved and parameterized sub-grid orographic drag in the ECMWF IFS and the MetUM. The ECMWF IFS is a semi-Lagrangian, hydrostatic spectral model formulated on a terrain following vertical coordinate system that is dependent on surface pressure. As a result, the dynamical core employed in the ECMWF IFS varies dramatically from that of the MetUM and, therefore, makes for a good comparison when it comes to understanding resolution sensitivity. The angular momentum equation in the ECMWF IFS is calculated from the following (as in chapter 2.3.1):

$$\begin{aligned}\frac{\partial\left[\int_{p_0}^{0} m\frac{dp}{g}\right]}{\partial t} &= \frac{1}{a\cos\phi}\frac{\partial\left(\left[\int_{p_0}^{0} mv\frac{dp}{g}\right]\cos\phi\right)}{\partial\phi} \\ -\left[\int_{p_0}^{0} fva\cos\phi\frac{dp}{g}\right] &- \left[p_0\frac{\partial z_0}{\partial\lambda}\right] - [F_0 a\cos\phi]\end{aligned} \tag{4.3}$$

where $m = ua\cos\phi$, a is the mean radius of the Earth, g is the acceleration due to gravity and F_0 has contributions from the BL turbulent stress, the SSO stress and the TOFD stress.

Not only do the models differ in their dynamical formulation but they also differ in their treatment of sub-grid drag processes. Both modelling groups have recognised the benefits of low-level orographic drag parameterization schemes for forecast scores and employ the Lott and Miller (1997) scheme as a result. However, the degree to which each component of the sub-grid scale orographic drag plays a role within their momentum budgets varies greatly, as has been recognised by the WGNE drag intercomparison project. These differences are due to the tuning of free parameters, such

as drag coefficients, their calculation of vertically averaged static stability and winds for use in the low-level Froude number and the fact that the ECMWF IFS also incorporates a component of turbulent orographic form drag (TOFD). TOFD accounts for orographic drag processes at scales smaller than $\sim 5km$ and is described in Beljaars et al. (2004).

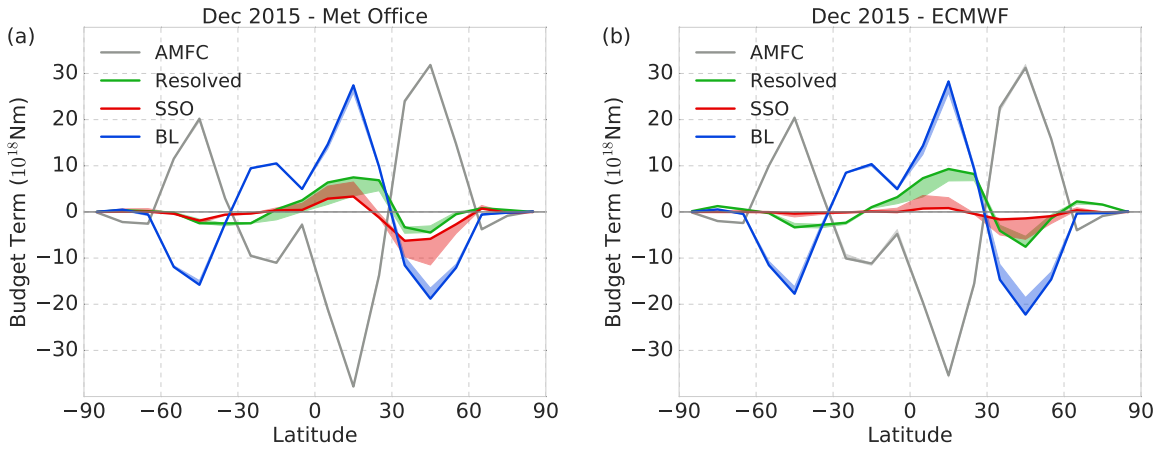

Figure 4.8: Dominant terms in the relative angular momentum budget, (4.1) and (4.3), integrated over 10° latitude bands and averaged over December 2015 short-range forecasts for (a) the MetUM and (b) the ECMWF IFS. The solid line indicates the value of the budget term in the highest model resolution and the shading indicates the range of the budget term over the highest and lowest model resolution (see text for model resolutions considered).

In the comparison performed here, the focus is on how the total orographic torque coming from the sub-grid scale orographic drag parameterization and the resolved orographic torque varies with resolution, so that it may be assessed whether the issues discussed in section 4.3 are model dependent. To ensure that the models have a similar AMFC, we perform 24 hour short range forecasts over the month of December 2015, as described in section 4.2.4, initialised from analyses. In the ECMWF IFS the horizontal resolutions chosen were linear triangular truncations TL159 and TL1279, which correspond to $\sim 1.132° \times 1.132°$ and $\sim 0.141° \times 0.141°$ in latitude and longitude, respectively. The MetUM resolutions chosen were N96 and N768, which correspond to $\sim 1.25° \times 1.875°$ and $\sim 0.15625° \times 0.234375°$ in latitude and longitude, respectively. In both cases the lowest resolution roughly corresponds to a typical climate model resolu-

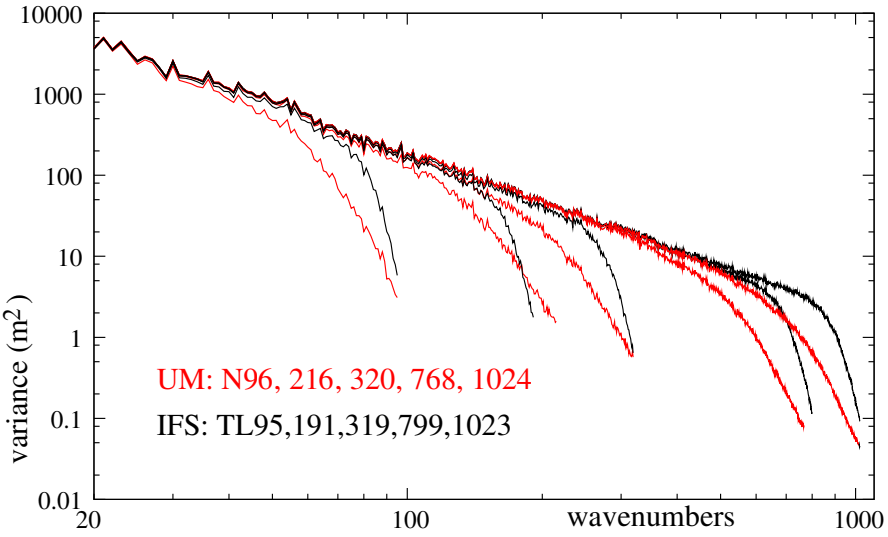

Figure 4.9: Variance versus wavenumber spectra of the mean orographic height used in the MetUM and ECMWF IFS at different horizontal resolutions and spectral truncations.

tion and the highest resolution is that used operationally for global numerical weather prediction, thus, spanning the range of resolutions over which the parameterizations are expected to perform.

Figure 4.8 shows the dominant terms in the angular momentum budgets for the MetUM and the ECMWF IFS for the short range forecasts performed over December 2015. The AMFC is well constrained by the short range forecasts, as had been shown previously in section 3.2.4. There is very little difference between the two models over the SH, particularly in the resolved orographic torque, apart from a pronounced peak in the SSO between 30S-60S in the MetUM, which is not present in the ECMWF IFS. Although small, the ECMWF IFS has slightly larger resolved and BL torque over this region, which accounts for it having less SSO torque. In the subtropics, between 0N-30N, there are striking differences between the two models, with the MetUM having a lot more SSO torque and slightly less resolved torque. There is, however, little difference in the BL torque over this region. The model budgets become distinct at the higher NH latitudes between 30N-60N. The resolved torque and the BL torque is larger in the ECMWF IFS, whereas the SSO torque is larger in the MetUM. The larger

resolved torque is to be expected given the fact that the ECMWF IFS has higher zonal resolution in these experiments.

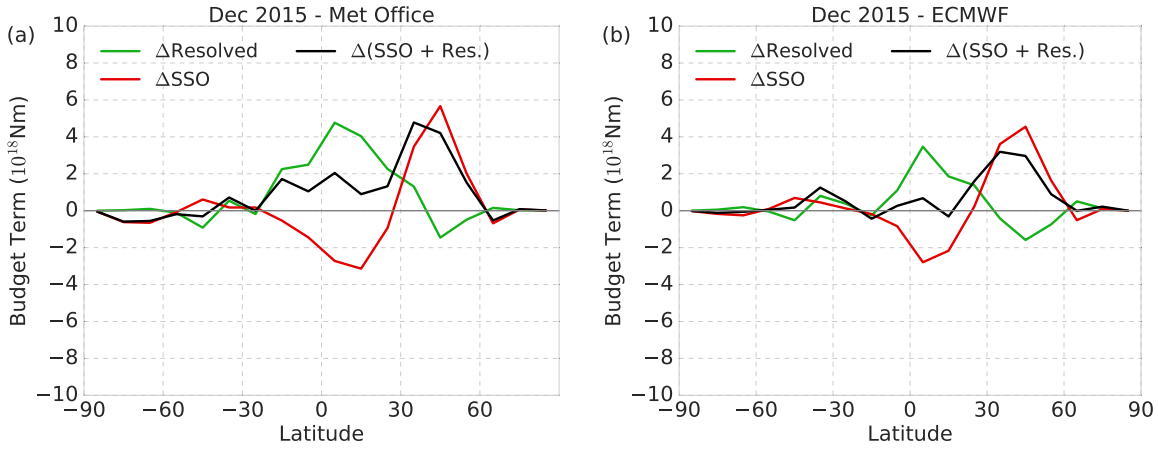

Figure 4.10: Change (high resolution minus low resolution) in the resolved (ΔResolved), parameterized (ΔSSO) and total (Δ(SSO + Res)) orographic torque with resolution in the (a) MetUM and (b) ECMWF IFS for short range forecasts performed over December 2015.

Although the differences in the parameterized torques between these models had been recognised previously in both the WGNE drag inter-comparison project and Sandu et al. (2016), the difference in the resolved torques have not. Apart from the difference in horizontal resolution, the differences in the resolved torques between the models may be due to the interplay between the parameterized and resolved torques described in section 3.5, but it is also possible that the treatment of the resolved orography plays some part. The filtering of orography in preparation for use in models is necessary for numerical stability but the choices made in this filtering can have an impact on the circulation (Irina Sandu, personal communication). Figure 4.9 (courtesy of Sylvie Malardel, ECMWF), shows the wavenumber power spectrum of the global orography for different resolutions of the MetUM and linear triangular truncations of the ECMWF IFS. The N value quoted in red refers to the MetUM resolution and the TL value quoted refers to the truncation of the ECMWF IFS, with higher resolutions having cut-offs at higher wavenumbers. The resolutions are chosen so that they are roughly equivalent. It is clear that the power drops off much more rapidly in the MetUM orography compared with the ECMWF IFS. At resolution N96 this drop off

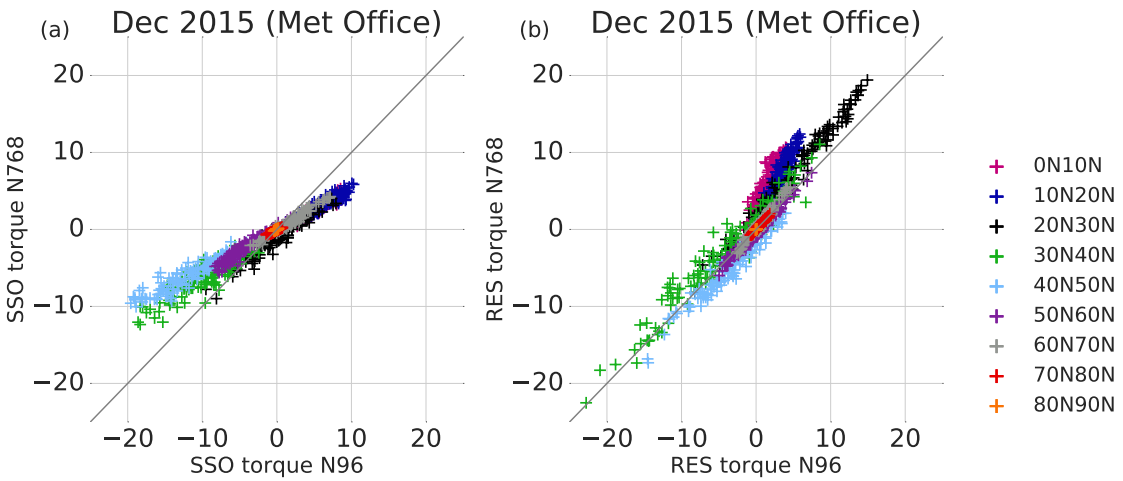

Figure 4.11: As in figure 4.3 but for the NH only and resolutions N96 vs N768 for short range forecasts performed with the MetUM over December 2015.

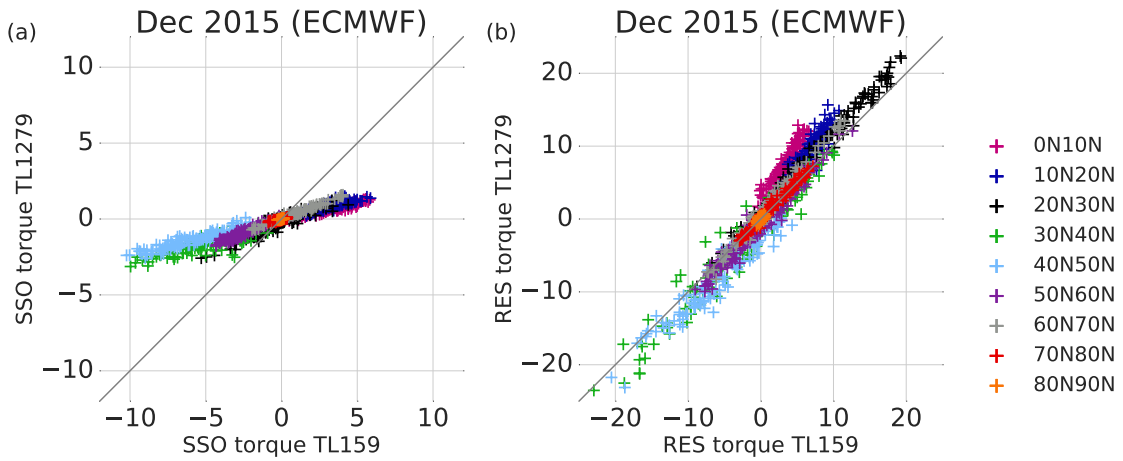

Figure 4.12: As in figure 4.3 but for the NH only and resolutions TL159 vs TL1279 for short range forecasts performed with the ECMWF IFS over December 2015.

occurs at large scales (approximately wavenumber 30), which may explain why the resolved torques are relatively small over the Himalayan region compared with the ECMWF IFS. The orographic spectrum may also indicate why the MetUM employs such large magnitudes of parameterized orographic drag, since it must account for the loss of variance at smaller scales in some other way.

Despite having varying magnitudes of total orographic torques within the two models, it is of interest to understand how this total changes when going to higher resolutions, since this will give some indication of the robustness to changes in resolution of the two models. Figure 4.10 shows the change (high resolution minus low resolution) in the resolved, parameterized and total orographic torque for the two models. The resolved torques show a similar resolution sensitivity at high latitudes, with some small differences in the subtropics, and the SSO torques also respond in a similar way across the two models. This means that the total orographic torque is also non-robust to changes in resolution in the ECMWF IFS, albeit to a lesser degree than the MetUM. This discrepancy is again more prominent in the northern high latitudes, suggesting that it is the Himalayan region that is the cause. It is not surprising that the two models show a similar resolution sensitivity given that they both employ the same orographic drag parameterization scheme that adapts to resolution based on the same sub-grid orographic statistics.

It is also of interest to consider how the variability of the orographic torques differ between the two models, since it is possible that the differences seen in their magnitudes are due to their treatment of the diurnal cycle. Figure 4.11 shows scatter plots, as in figure 4.3, of the orographic torques at low resolution versus high resolution in the MetUM. The same is shown in figure 4.12 but for the ECMWF IFS. Since each cross corresponds to a 6 hourly value, the range spanned by the points gives an indication of the daily and diurnal variability. Departure from the one-to-one line indicates a change with resolution. As was found previously in section 4.3 for the MetUM, both models have a strong resolution sensitivity in their SSO torques but little in their resolved torques between 30N-60N. Overall, the SSO torques show little variability in sign, whereas the resolved torques vary substantially with sign. This, again, indicates that there may be something about the treatment of the sub-grid orography, commonly shared in both models, that is leading to this resolution sensitivity over the NH mid-latitudes.

4.5 Impact on model bias

Figures 4.13a, 4.13b and 4.13d show the total orographic torque, resolved plus parameterized, for the January 1998 and January 2010 nudged experiments and the January 2010 forecast experiments in red. Although the total torque is very similar at most latitudes, implying that the model maintains a total orographic torque across resolutions in most areas, there are certain regions where the N96 experiments have much larger orographic torque than the higher resolutions. The most prominent of these is the 30N to 60N region, where the N96 resolution has in excess of a quarter more than that of the N512 experiments. This behaviour is seen in both the nudged and the forecast experiments.

The impact of this additional torque at lower resolutions on the large scale circulation may be substantial and could lead to large systematic biases in climate models. In order to quantify the drift that would have occurred in the nudged experiments if this model were free running the tendencies output by the nudging routine are analysed, which are proportional to the differences between the model and ERA-interim at every time-step. These tendencies have been vertically integrated and represented as a torque in figures 4.13a and 4.13b in blue, with the shading again indicating the range between the model resolutions. Both years show an overall decrease in the magnitude of the nudging tendencies with increasing resolution at most latitudes, as might have been expected based on the fact that we are parameterizing less and thus prone to less parameterization error. This monotonic reduction in the nudging tendencies with increasing resolution is consistent with the climatological biases in the free running version of the MetUM, which are found to reduce in amplitude but remain similar in structure and spatial distribution across resolutions (Martin et al., 2010).

In both the 1998 and 2010 nudged experiments, in the 30N to 60N region where this discrepancy in the total orographic torque is persistently identified, the nudging torque is of the opposite sign to the additional orographic torque at lower resolutions. There is a striking difference in the magnitude of the nudging torque in this region between the Jan 2010 and Jan 1998 experiments, with the 2010 values being more than double those of 1998. This is consistent with the fact that the Jan 2010 experiment has both larger orographic and BL torques, which may be acting to decelerate the flow in excess and, thus, the nudging has to respond more strongly. Figure 4.7 identifies this model error as being likely due to the SSO torques over the Himalayas.

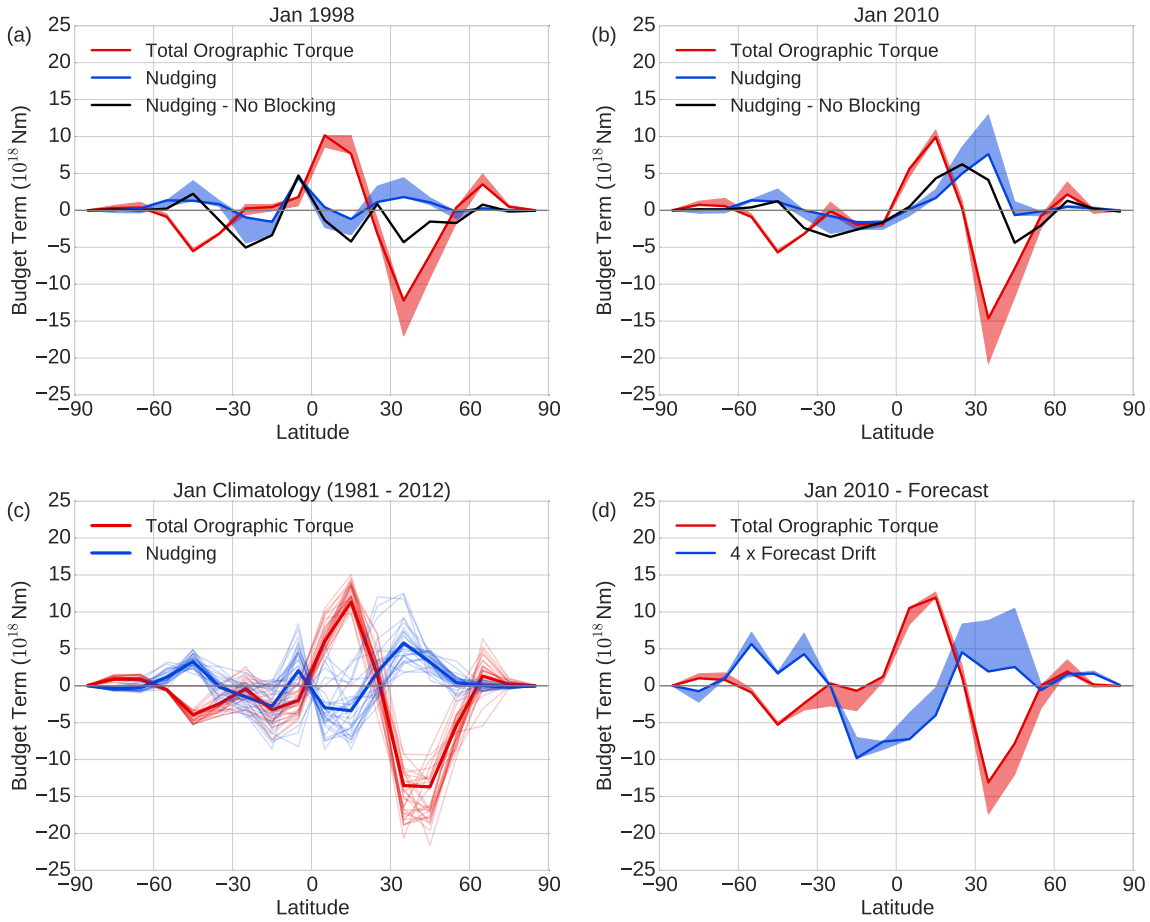

Figure 4.13: Vertically integrated nudging tendencies and total resolved plus parameterized orographic torque for (a) January 1998 nudged experiments, (b) January 2010 nudged experiments and (c) January climatology from 1981 to 2012. (d) shows the drift relative to the analysis in the vertically integrated angular momentum ($\times 4$) and the total orographic torque for short-range forecast experiments over January 2010. In (a), (b) and (d) the solid line indicates the value of the N512 experiment and the shading indicates the range over the N96, N216 and N512 resolution experiments. In (c) the thick line indicates the climatology and the thin lines are the individual years, at N96. The black lines in (a) and (b) indicate the nudging tendencies at N96 when the orographic blocking is set to zero (NoBLK).

The drift in the forecast experiments was calculated as the difference in the vertically integrated and zonally averaged rate of change of angular momentum, $\partial[\int_{z_0}^{\infty} m\rho dz]/\partial t$, between the model and analysis over the 24 hour forecasts. This is shown in blue in figure 4.13d and has been multiplied by a factor of four since the scale of the drift in the forecast is much smaller than the nudging. The reason for this amplitude difference comes from the fact that the forecasts are initialised throughout the entire depth of the atmosphere, whereas the nudging is applied only in the upper atmosphere. Besides their magnitude, there are several other differences between the forecast drift and the nudging tendencies, such as the large drift seen in the tropics and the double maxima seen between 30S and 60S. The drift in the tropics does not reduce with increasing resolution, as was also seen in the nudging tendencies for January 1998. Understanding the model bias in the tropics may be much more complex than in midlatitudes as a result of diabatic processes. The focus of this study, however, is the midlatitudes where the model drift reduces with increasing resolution, particularly between 30N and 60N. This supports the idea that excessive parameterized orographic torque at lower resolution may be leading to model bias in the NH midlatitudes.

In the assessment of nudging tendencies as an indication of the model bias, it is important that they are generally representative of the overall climatological biases in the model. By performing 32 separate experiments using the N96 setup for each January in the years 1981 to 2012, a climatology of the nudging tendencies at the N96 resolution was built. Figure 4.13c shows the total orographic torque for the individual Januaries from 1981 to 2012 in red and the corresponding vertically integrated nudging tendencies in blue, with the thick line indicating the mean January climatology. The positive torque from the nudging tendencies acting to accelerate the atmosphere in the region between 30N and 60N is quite robust across all of the years, with some years having very substantial values here. In addition to this easterly bias in the NH, there also appears to be a robust easterly bias in the SH midlatitude jet.

The effect of the additional parameterized torque at the N96 resolution is assessed by setting the orographic blocking term, the largest component in the SSO torque, to zero and looking at the resulting nudging tendencies, which are shown in black in figures 4.13a and 4.13b. The vertically integrated tendencies of the experiment without orographic blocking (NoBLK) are of similar magnitude and sign as those of the N96 control experiment (CNTRL) in most latitudes, apart from in this interesting 30N to 60N region, where the magnitude is substantially reduced or the sign is switched. This

implies that the low level blocking parameterization can have a significant impact on the large scale circulation over the NH extra-tropics. The change in sign of the nudging tendency indicates that the parameterized blocking term is needed but is too strong. Additionally, the lack of change in the nudging tendencies at other latitudes suggests that there may be compensation by other terms in the momentum budget occurring. The compensation by other terms within the momentum budget is discussed in the following section.

4.6 Compensation by other terms in the momentum budget

The nudging framework employed here is ideal not only for resolution sensitivity studies but also for parameter sensitivity studies. Since the AMFC is constrained through nudging, without the torque due to orographic blocking other terms in the momentum budget could increase or decrease in order to compensate for this. The way in which the BL torque, resolved torque and subsequently the nudging respond to this loss of orographic torque may give some insight into the suitability of using one parameterization scheme to compensate for the other and the consequences of such substitutions.

Figure 4.14 shows the major contributors to the zonal mean momentum budget at N96 resolution for the January 1998 and January 2010 CNTRL and NoBLK experiments. The SSO torque does not go to zero in the NoBLK experiment due to the gravity wave component of the parameterization, which was not set to zero so as to investigate its response to the loss of orographic blocking. In general there is little difference in the BL torque over the SH in figure 4.14 where the reduction in SSO torque leads to a decrease in the nudging tendency between 60S and 40S and a change of sign at 40S (Figures 4.13a and 4.13b). Within the 10S to 40S region the resolved torque decreases, but unlike in the NH this is a compensation since the resolved torque is of opposite sign to the SSO torque. The NH shows a strong response from the BL and resolved torques, where the loss of blocking is almost fully compensated by a combination of the two in the 0N to 30N region. However, despite the BL torque increasing substantially over the 30N to 60N region, the compensation is not large enough to account for the loss of the blocking term. What is more, the torque due to gravity wave drag increases from a negligible amount, which is indistinguishable from the zero

line, to the lower edge of the shaded region in the SSO term in figures 4.14a and 4.14b. This lack of compensation from the BL torque and parameterized gravity wave torque between 30N to 60N is evident in the vertically integrated nudging tendencies (4.13a and 4.13b), where they become less positive and/or change sign.

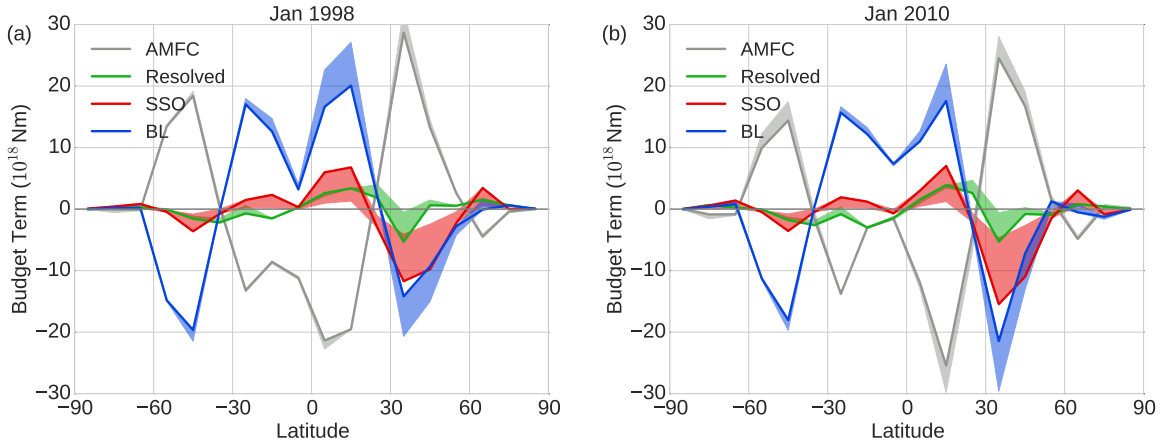

Figure 4.14: Dominant terms in the angular momentum budget of the N96 CNTRL experiments and N96 NoBLK experiments for (a) January 1998 and (b) January 2010 with nudging. The solid line indicates the values of the N96 CNTRL experiment and shading indicates the range of the term between the CNTRL and NoBLK experiments.

An increase in the parameterized gravity wave drag occurs due to an increase in the local wind speed and, as a result, an increase in energy available to scale the mountain and generate gravity waves. Both the turbulent mixing (Lock et al., 2000) and turbulent orographic form drag (Wood and Mason, 1993) component of the BL parameterization have a dependence on wind such that an increase in the local wind will lead to an increase in the total BL drag, which is why we see this compensating behaviour when the orographic blocking is switched off. One might also expect that increased winds would lead to larger pressure gradients acting on resolved orography and, as a result, larger resolved torques being exerted on the atmosphere. What is most surprising about these NoBLK experiments is that the resolved drag does not compensate for the orographic blocking between 20N to 60N and, instead, becomes more positive between 20N to 30N and less negative (or changes sign) over 30N to 50N. The change in the resolved torque acts in the same sense as the change in the SSO torque and together leads to the large decrease or change of sign seen in the

nudging tendencies over this region.

As discussed in section 4.3, the individual mountain massifs respond differently to changes in resolution and it is now evident from figure 4.14 that they also respond differently to removal of the blocking parameterization. In order to identify the response of the torques over specific regions of the globe to switching off the orographic blocking, latitude/longitude plots of the change in vertically integrated momentum budget tendencies between the N96 CNTRL and NoBLK experiments are plotted in figure 4.15, along with their hemispheric means on the left and right hand side of each panel. The contribution from integrating over the Antarctic continent is plotted in the bottom right-hand corner of each panel. The terms have not been area weighted and are expressed as a stress (Pa), in order to expose some of the finer details at higher latitudes (according to our sign convention, these stresses are actually the negative of the surface stress as conventionally defined). Figures 4.15a and 4.15b show the change in the SSO and BL stress and figure 4.15c shows the sum of these changes, so as to identify where the BL stress (and gravity wave drag) does not compensate for the loss of orographic blocking. Figure 4.15d shows the differences in the semi-Lagrangian advection tendencies; since the AMFC is constrained by nudging, these will be predominantly due to changes in the resolved pressure torques. The sum of the change in the SSO, BL and advection term is shown in figure 4.15e and the change in the nudging tendencies is shown in figure 4.15f, note the change in scale. The similarity of figures 4.15e and 4.15f confirms that the budget is well closed. The change in the surface pressure when blocking is switched off is plotted in figure 4.16 along with the 850hPa wind vectors from the CNTRL experiment. Comparing figure 4.15e and the wind vectors in figure 4.16, it is evident that the sign of the parameterized stress depends on the sign of the wind.

The responses seen over individual mountain regions are summarised in table 4.1 by stating the sign of the term in the CNTRL experiment, the degree to which each term is able to compensate and the change seen in the nudging tendency. If the sign of the nudging is opposite to (the same as) the blocking stress in the CNTRL experiment it suggests there is excessive (insufficient) surface stress in that region in the CNTRL experiment. Where there is excessive stress and removing the orographic blocking leads to a decrease in the magnitude of the nudging, the BL and resolved stress do not compensate fully for the loss of blocking and the model bias is reduced. Where there is insufficient drag and the magnitude of the nudging tendencies increase when blocking

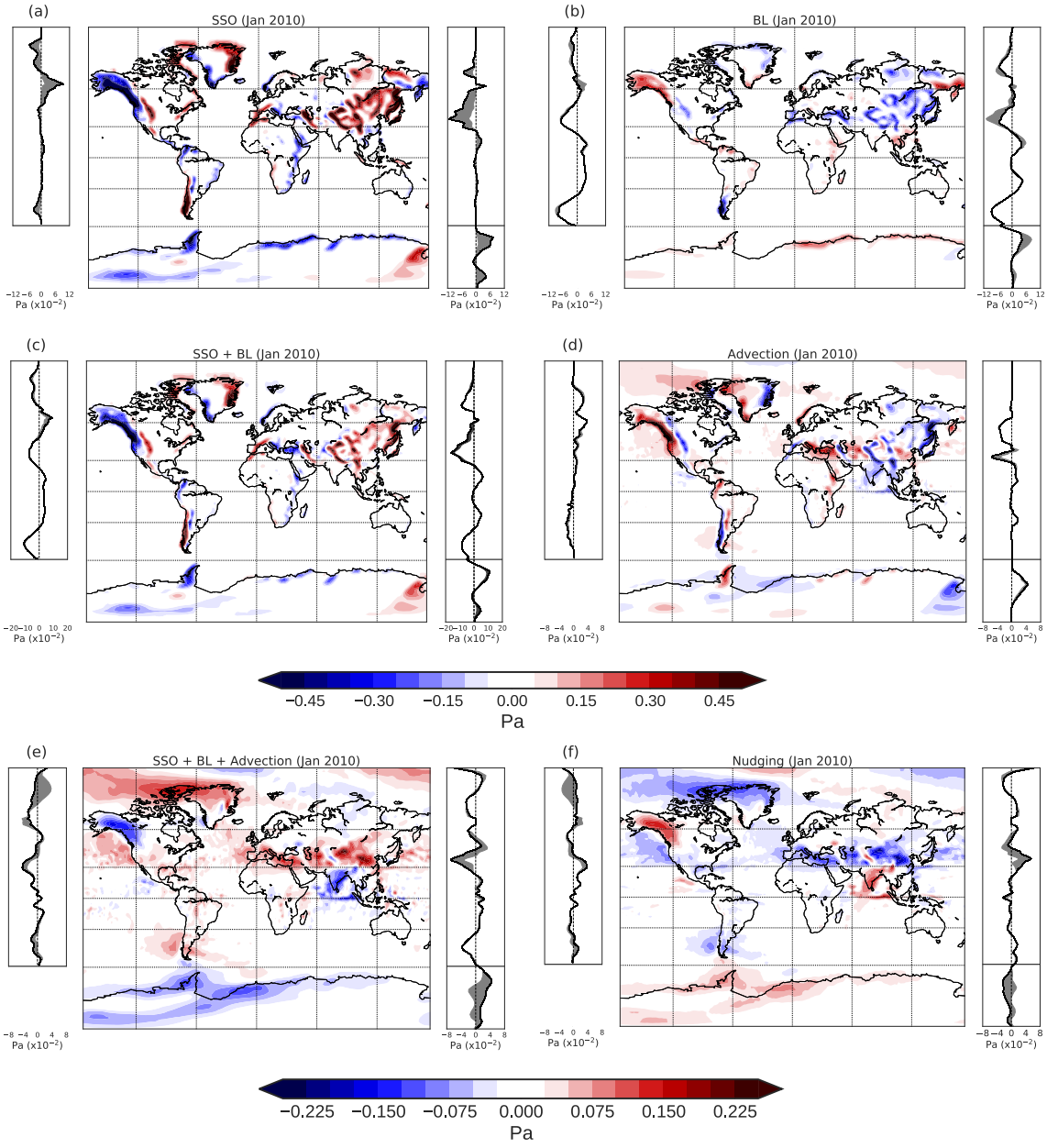

Figure 4.15: N96 NoBLK minus N96 CNTRL vertically integrated momentum budget tendencies for January 2010 for the (a) SSO, (b) BL, (c) sum of the SSO and BL, (d) semi-Lagrangian advection, mainly representing the resolved pressure torque, (e) sum of the SSO, BL and semi-Lagrangian advection and (f) nudging. Note the difference in scale between figures (a)-(d) and figures (e) and (f). Left and right side panels are the Western and Eastern Hemisphere zonal means, respectively. The lower right side panel is the mean over the Antarctic. The solid line indicates the values of the N96 CNTRL experiment and shading indicates the range of the term between the CNTRL and NoBLK experiments.

is switched off, the BL and resolved stress do not compensate fully and now the bias is increased. Where the magnitude of the nudging tendencies remain unchanged, the resolved stress and BL stress compensate for the loss of orographic blocking. We see that over the Antarctic, the Andes and Europe, the nudging is of opposite sign to the SSO in the CNTRL, indicating excessive drag, and the bias is reduced as a result of removing the parameterized blocking stress. Over East Asia, Central America and East Africa, there is little change in the nudging when blocking is removed, indicating that the BL and resolved stress compensate for the parameterized blocking over these regions. The only region over which there is insufficient drag in the CNTRL and the nudging tendencies increase in magnitude in NoBLK is over the Rockies, particularly to the North.

By far the most complex topographic region is the Himalayas and the Tibetan Plateau, which is why it is not included in table 4.1 and will be discussed here. The BL stress is able to compensate partially over the major regions of the Himalayas (fig. 4.15c) and, while the resolved stress compensates over the highest peaks (fig. 4.15d), the total stress reduces on the leeward side of the Himalayan mountain chain (fig. 4.15e), acting to reduce the drag on the westerlies in this region. Since the BL does not fully compensate for the loss of parameterized blocking and the resolved stress responds in the opposite sense to a compensation, the nudging tendencies reduce substantially or even change sign (fig. 4.15f).

Consistent with the large change seen in the resolved pressure torque when blocking is switched off, figure 4.16 shows that there is a large increase in the surface pressure on the leeward side of the Himalayan mountain chain. Similar magnitude changes can be seen over the Northern Rockies and Europe. The changes in surface pressure over the NH seen in these nudged experiments match closely with the forecast experiments performed by Sandu et al. (2016) after a 24 hour lead time in which the orographic blocking was increased. They looked at how the surface pressure responded to increasing the blocking over specific mountain regions using short range forecasts and found that all of the changes in the surface pressure in midlatitudes at a 24 hour lead time are local responses to changes in the blocking. This indicates that the changes seen in the surface pressure and, therefore, resolved pressure torques in the nudged experiments are also tied to the specific topographic features.

Table 4.1: Sign of momentum budget terms in CNTRL experiment and response in NoBLK experiment over specific mountain regions in figure 4.15.

	SSO	BL	Resolved	Nudging
Antarctic	Coast/Peninsula: >0	Coast: CNTRL>0 Partial compensation	Peninsula: CNTRL >0 Strong compensation	CNTRL <0 Large decrease in magnitude
	Ross Ice Shelf: <0	Ross Ice Shelf: CNTRL ∼0 No response	Ross Ice Shelf: CNTRL <0 Full compensation	Ross Ice Shelf: CNTRL >0 Little change
Andes	<0	CNTRL <0 Large compensation in south No response in north	CNTRL <0 Partial compensation	CNTRL >0 Large decrease in magnitude
E. Africa	>0	CNTRL >0 Little compensation	CNTRL >0 Localised compensation over Ethiopia and Tanzania	CNTRL <0 Little change
C. America	>0	CNTRL >0 Little compensation	CNTRL >0 Almost full compensation	CNTRL >0 Little change
Rockies	North: >0	North: CNTRL >0 Partial compensation	North: CNTRL >0 Partial compensation	North: CNTRL >0 Increase in magnitude
	South: <0	South: CNTRL <0 Little compensation	South: CNTRL <0 Almost full compensation	South: CNTRL <0 Increase in magnitude
Europe	Alps/Caucasus: <0	Alps: CNTRL <0 Little response Caucasus: CNTRL <0 Partial compensation	Alps/Caucasus: CNTRL <0 Almost full compensation	Everywhere: CNTRL >0 Large decrease in magnitude
	Turkey/Croatia: >0	Turkey: CNTRL <0 Compensation of opposite sign	Turkey: CNTRL >0 Increase in magnitude in response to BL	
E. Asia	<0	CNTRL >0 Change in sign for partial compensation	CNTRL <0 Full compensation	CNTRL ∼0 Little change

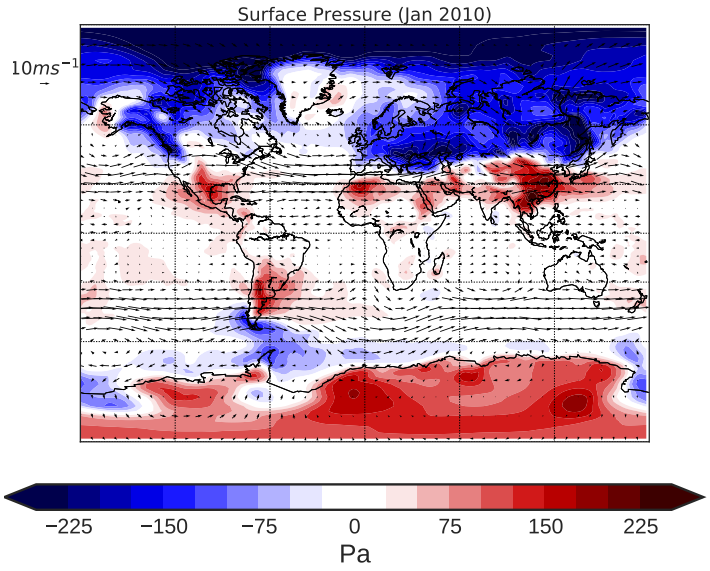

Figure 4.16: Difference in the surface pressure between the N96 CNTRL and N96 NoBLK nudged experiments, vectors are 850hPa wind for CNTRL.

4.7 Conclusions

The sensitivity of resolved and parameterized orographic torques to changes in model resolution and parameterization within the Met Office Unified Model and the ECMWF IFS was investigated in the context of the angular momentum budget. The methods employed in this study demonstrate that nudging techniques can be fruitful in diagnosing errors in the parameterized surface stresses and have illuminated the impact that orographic parameterization schemes have at lower (climate) horizontal resolutions. By nudging the MetUM towards ERA-interim within the regions of maximum momentum flux convergence in the free atmosphere, we were able to constrain the angular momentum flux convergence term within the momentum budget across model resolutions and reproduce the ERA-interim low level winds. The boundary layer torque did not change substantially across resolutions, while the parameterized orographic torque (SSO) saw the largest change. Although there was good agreement in the total orographic torques at varying resolutions in most regions, there was a large discrepancy over the 30N to 60N region. This difference is attributed to the additional parameterized orographic torque at the lower resolutions, which is not balanced by a decrease in the resolved torque. Deconstructing the zonal mean SSO torque and resolved torque into their

Eastern and Western Hemispheric contributions, it was shown that the resolution sensitivity of the SSO torque came largely from the Eastern Hemisphere. This resolution sensitivity was validated using short range forecasts, which were shown to support the orographic torque resolution sensitivity in our nudged experiments.

Tendencies from the nudging routine corroborate the findings of Brown (2004) who suggest that the parameterized orographic torque within the 30N to 60N region at lower resolutions may be excessive. This was done using the ECMWF forecast model of the time, which is a completely different model to the MetUM but was run at resolutions comparable to those used here. The vertically integrated nudging tendencies in this study exhibited a tendency towards accelerating the atmospheric flow in the NH in the region where the parameterized orographic torque (which acts as a drag) is the largest. The magnitude of the nudging tendencies reduced as the parameterized torque reduced within this region when the resolution was increased, indicating that it may be the additional parameterized orographic torque that is the cause of the larger model error at lower resolution. The drift over 24 hours in short range forecasts also showed that the forecast winds were too weak in the 30N to 60N region, with this drift decreasing with increasing resolution. What is more, the climatological nudging tendencies show a large acceleration of the atmosphere at the low resolution within both the NH and SH jets, which suggests this could be linked to a robust model bias. Previous studies have shown that many systematic biases in climate models develop over short timescales and, since these errors remain local over these timescales, the analysis of nudging tendencies within constrained models can provide a means of understanding the origins of these biases (Ma et al., 2014).

A comparison was made with the ECMWF IFS model using short range forecasts. The results suggest that, while the total orographic drag may be very different in the two models, its non-robustness to resolution over the NH mid-latitudes (over the Himalayas) is present in both models. With the ECMWF IFS and MetUM both employing the same orographic drag parameterization scheme, it is not surprising that the resolution sensitivity and diurnal variability of the parameterized torques are similar across the two models. The variance spectra of the mean orographic height in the MetUM and the ECMWF IFS reveals that smoothing of the orography at higher wave numbers, a common procedure in model ancillary preparation, is very different for the two models, with the MetUM having much less power at high wavenumbers. This suggests that the additional parameterized drag employed in the MetUM may be a

means of accounting for the loss of these smaller scales in the resolved orography.

The resolved orographic torque may be insensitive to model resolution in the regions over the Himalayas and the Rockies at the resolutions considered in this study due to the large scale nature of these features. If the large scales were dominating at these resolutions, there may not be an increase in the resolved drag until a resolution is reached in which additional small scale processes can be represented. Power spectra of the resolved pressure drag over East Africa and the Himalayas (not shown) indicate that the model does respond to changes in resolution, since there is additional small scale variance when going to higher resolution. However, the peak of the power spectrum over the Himalayas is at much larger scales, which are already well represented at N96, whereas the peak of the power spectrum over East Africa occurs at smaller scales. This explains why we see little additional resolved drag over 30N to 50N, but an increase in resolved drag over 10N to 20N, when going to higher resolutions. This may also explain why the parameterization scheme does not perform well over the Himalayas at the lower resolutions, since the large sub-grid scale mountains that are fed into the parameterizations at lower resolutions may not be suited to parameter choices made when optimising the schemes for results at higher resolutions. The lack of a scale separation in the orographic spectrum makes the modelling of orographic effects a challenge in seamless modelling and validation. Further work is required to fully understand the behaviour of the flow in the presence of orography with increasing horizontal resolution.

The blocking component of the orographic drag parameterization scheme was switched off so that the sensitivity of the nudging tendencies and other terms within the momentum budget to this parameterization may be investigated. Whilst in most regions the zonal mean nudging tendencies were similar to that of the N96 control experiment when blocking was switched off, a large change was seen over the 20N to 60N region in both the January 1998 and 2010 experiments. A lack of change in the nudging tendencies elsewhere indicated that there must be compensation by other terms in the momentum budget when the blocking is switched off. Zonal mean responses of each term within the momentum budget to the loss of orographic blocking suggests that it is predominantly the BL torque that compensates in most regions, although the resolved torques did aid the compensation to some extent. The resolved torques were found to compensate in the opposite sense to that of the SSO torques over the 20N to 30N region, however, and the BL response was found to be incomplete over this region,

leading to a decrease or a change in sign of the positive nudging tendencies.

Global maps of the latitudinal and longitudinal distribution of the change in the various terms in the momentum budget in response to switching off the orographic blocking parameterization show that, while a combination of the resolved and BL stresses compensate for the orographic blocking in many regions, they can also yield an opposite response. The complex mixture of positive and negative stress over Eurasia between 20N to 40N coming from the BL, SSO and resolved stress lead to an overall decrease in the zonal mean drag over this region. This large change can be attributed to a change in the surface pressure on the leeward side of the Himalayas and an overall strengthening of the meridional pressure gradient to the north of the Eurasian mountain chain along 20N to 60N, which is also seen in the experiments of Sandu et al. (2016). The response of the resolved torque to variations in the strength of the sub-grid scale orographic torque raises questions in regards to the feedbacks between resolved and parameterized orographic processes. It is also clear that a substitution of the BL parameterization for the orographic blocking parameterization is not suitable in all regions.

Overall, we see that the behaviour of the resolved and parameterized surface drag does not agree over the Himalayan region, which indicates that the parameterized component may not be dealing with this complex topography and atmospheric flow in a realistic manner at climate model resolutions. This motivates the more detailed investigation of this region in the next chapter.

Chapter 5

Response to parameterized vs. resolved orographic drag over a region of complex topography: high resolution simulations over the Himalayan Plateau

5.1 Introduction

Tibaldi (1986) demonstrated that it is not only the large scale orographic features but also the additional smaller scales of orography that maintain the quasi-stationary circulation in the Northern Hemisphere. That work motivated the need to represent the smaller, unresolved orographic scales within models, inititially through the use of envelope orography and, subsequently, through parameterization schemes, beginning with a parameterization for gravity wave drag (Chouinard et al., 1986; Palmer et al., 1986; McFarlane, 1987). Atmospheric modelling groups now implement more complex parameterization schemes that account for various different orographic drag processes. For example, the Lott and Miller (1997) parameterization scheme, variations of which are employed in several NWP and climate models, accounts for drag due to vertically propagating gravity waves and low-level flow blocking. As discussed in chapter 2.1, theoretical studies of idealised mountains in idealised flows have provided analytical expressions for use in these parameterization schemes (e.g. Phillips 1984; Smith 1980;

see Teixeira 2014 for a review). Numerical simulations (for example Carissimo et al. 1988; Kim and Arakawa 1995) and laboratory tank experiments (see Boyer and Davies 2000 for a review), also mostly in idealised conditions, have lead to a wealth of development in the field of orographic drag parameterization. They have helped to constrain the variables that determine the transition between orographic drag processes, such as the transition from blocked flow to gravity wave generation (e.g. Stein 1992). The resulting parameterization schemes have also been extensively validated against observational campaigns, most notably the PYRenees field EXperiment (PYREX) (Bougeault et al. 1992; Lott and Miller 1997; Georgelin et al. 2000 and references within Bougeault et al. 1997), and have been shown to perform well in these regions and flow regimes. However, the suitability of these parameterization schemes to realistic, more complex flows and topographic features is not well documented or understood.

Deriving analytical expressions for and performing field experiments over more complex topography with large horizontal scales and complex flows has inherent difficulties. We therefore appeal to high resolution models, in which the orography and interacting dynamics have smaller errors in their approximations of the orographic and atmospheric gradients. This chapter aims to validate the model's parameterization scheme by comparing the impacts of additional resolved orography with the addition of parameterized orographic drag over one of the NH's largest and most complex topographic features: the Himalayan Plateau. With a maximum elevation of more than $8km$ and a longitudinal and latitudinal extent of approximately 2,500km and 1,000km, respectively, the Himalayan Plateau serves as a demanding test for the parameterization scheme. What is more, as a result of its horizontal extent, elevation and close proximity to the mid-latitude jet, it leads to substantial deflection of the impinging winds and results in the generation of complex flow.

Motivated by our findings in chapter 4 we attempt to answer the following questions using high and low resolution simulations from two comprehensive operational forecasting and climate models that simulate realistic flow:

1. How does the impact on the large scale circulation differ between adding parameterized orographic drag and adding small scales to the resolved orography?

2. How does the additional resolved orography and parameterized orographic drag affect the model drift?

3. In chapter 4 it was discovered that the resolved orographic drag does not change substantially with increasing resolution over the mid-latitudes. However, the highest resolution considered was approximately $25km$ and the question remains: does the resolved orographic drag increase substantially going from a low ($150km$) to a very high ($5km$) horizontal resolution?

4. How well do the vertical momentum fluxes from the parameterized gravity wave drag compare with the resolved momentum fluxes?

5. Why is the parameterized orographic blocking drag so large over the Himalayas (see chapter 4)?

6. Given that the schemes are based on very simple flows over simple topography, are the approximations made in the parameterization scheme appropriate for this complex flow and topography?

7. Is the response to parameterized orographic drag a general feature of the parameterization scheme or is it model dependent?

The structure of this chapter is as follows. We begin by describing the models and experimental setup in section 5.2. Section 5.3 then goes on to discuss the impacts of the resolved versus parameterized orographic drag on the large scale circulation in the Met Office Unified Model (MetUM). The drift, relative to the Met Office analysis, in the MetUM experiments is then compared in section 5.3.1. The magnitudes of the resolved and parameterized surface stresses in our high and low resolution global and limited area experiments are diagnosed in section 5.3.2 using momentum budget calculations. The suitability of the parameterization scheme to the complex flow over the Himalayas is investigated in section 5.4. The impact of the resolved versus parameterized drag on the circulation over the Himalayas is then compared in a second fully operational model, the ECMWF IFS, in section 5.5. Finally, a summary of our findings and remarks on the questions listed above are given in section 5.6.

5.2 Experimental setup

A comparison between the addition of high resolution orography versus that of an orographic drag parameterization scheme is performed using Limited Area Modelling

(LAM) simulations over the Himalayan Plateau. Simulations were performed using the Met Office Unified Model at version 10.2 with ENDGame dynamics (Wood et al., 2014), which employs a semi-Lagrangian, non-hydrostatic dynamical core with a geometric hybrid height vertical coordinate system. The global driving model used was that of the current operational climate model at resolution N96 which has a longitudinal and latitudinal grid point resolution of 1.87x1.25 degrees, respectively, approximately equivalent to $150km$ in the longitudinal direction in mid-latitudes. The global model was reinitialised every 24 hours with Met Office operational analyses so as to prevent the large scale circulation from drifting too far from our best guess of the atmospheric state, thus allowing the orography to interact with realistic flows and removing the added complexity of internal variability. The LAM, however, is free-running in the sense that it is not re-initialised from the analysis and is constrained only through the boundary conditions.

In order to get as high resolution as computational constraints would allow, without restricting our area of interest too much, our high resolution LAM experiments are performed at a grid-point resolution of 0.06x0.04 degrees, giving a spatial resolution of approximately $5km$ in the longitudinal direction over our domain. Both the LAM and the driving model have 70 vertical levels extending to $80km$ and have prescribed SSTs and sea-ice. The procedure used in applying the lateral boundary conditions is described in Davies (2014). The lateral boundary conditions from the global driving model to the LAM are applied gradually over 24 grid boxes using linear blending weights such that at the very edge of the LAM domain the prognostic variables are exactly equal to the driving model's. This allows the high resolution flow to develop gradually while ensuring that the incoming circulation is comparable to what is present in the global model. The boundary conditions are updated 6 hourly and the experiments are run from the 1st to 7th of January 2015. Denis et al. (2002) showed that one-way nesting has skill in downscaling large-scale information to the regional scales, reassuring us that the small scales that develop in the LAM experiments are representative of a high resolution global simulation. A full list of the experiments performed along with their reference names is given in table 5.1 but a detailed description of their setup is given below.

Our LAM domain extends from 54E to 126E in the longitudinal direction and from 16.5N to 48.5N in the latitudinal direction, so as to ensure that the boundaries are sufficiently far from the centre of the domain for the high resolution flow to develop.

Figure 5.1 shows the mean resolved orographic height over the domain considered at both low ($150km$) and high ($5km$) resolution. Clearly, the low resolution is much smoother than the high resolution orography and, although there are only small differences over the flat topped Plateau itself, there are much larger differences, of several kilometres altitude, north of 40N between 70E and 90E and over the southern edge over the Himalayan mountain range. Overall, the orography is much more complex in the high resolution. The impact of this additional resolved orography on the circulation over this region is assessed in a consistent manner such that any additional impacts on the circulation that occur as a result of changes in atmospheric resolution are precluded. This is done by performing two experiments at high ($5km$) resolution using our LAM. In the first, the orography is generated from the Global One-kilometre Base Elevation (GLOBE) $1km$ resolution orography dataset using the standard operational method described in Webster et al. (2003), referred to as HR Orog UM. In the second, the orography is interpolated from the climate model resolution orography onto the high resolution LAM domain, referred to as LR Orog UM. This means that any differences seen in the circulation are solely a result of adding small scales to the orographic spectrum.

The impact of the parameterization scheme on the circulation over the Himalayan region is then investigated using an additional short-range forecast experiment with the low resolution global model. In this experiment (NoSSO UM) the sub-grid scale orography is removed only over the Himalayan region using a Gaussian function to allow for a smooth transition over the boundary between the region with and without sub-grid scale orography. Differences between the global low resolution driving model (CNTRL UM) and NoSSO UM will give a consistent comparison between the impact of additional resolved orography over the Himalayas versus the addition of parameterized orographic drag, without the impacts from removing SSO drag over other regions. Output from the global and LAM MetUM simulations are analysed 3-hourly. The high-resolution simulations allow an evaluation of the explicit impact of small-scale orography on the atmosphere, whereas the low-resolution simulations allow an evaluation of the impact of the (supposedly equivalent) parameterized drag.

Since we know that the MetUM employs the same parameterization scheme as the ECMWF IFS, it is instructive to consider whether the impact of the additional parameterized drag on the circulation is similar between the two models so that we may make more general statements about the parameterization scheme. A set of global short-

range forecast experiments, courtesy of Irina Sandu (ECMWF), was performed with the ECMWF IFS over the period of the 1st to 7th of December 2015. The set of experiments consist of the following: resolution TCo199, which equates to approximately $50km$ in mid-latitudes, with operational settings (CNTRL IFS); resolution TCo199 with SSO drag removed globally (NoSSO IFS); resolution TL1279, which equates to approximately $16km$, with operational settings (HR IFS); and resolution TL1279 with SSO drag removed globally (HR NoSSO IFS). TLXX denotes a linear (reduced) Gaussian grid with triangular truncation XX and TCoXX denotes a cubic octahedral mesh with triangular truncation XX (see Hortal and Simmons (1991) and Wedi et al. (2015) for more details on the different grids). The differences between the HR NoSSO IFS and NoSSO IFS experiments will give the impact of the additional resolved orography, without feedbacks from the changes in the orographic drag parameterization scheme. The CNTRL IFS minus NoSSO IFS experiments will give the impact of the parameterized orographic drag. Output from the global ECMWF IFS simulations are analysed 12-hourly. The ECMWF IFS experiments do not exactly parallel those of the MetUM but provide another means of evaluating the impacts of the resolved and parameterized orographic drag on the atmospheric circulation.

Table 5.1: List of experiments analysed over the Himalayan Plateau. Columns are, from left to right: name of experiment; horizontal resolution; whether or not experiment has parameterized sub-grid orographic drag turned on; whether experiment is global or limited area; and dates of the 24-hour short range forecasts.

Experiment	Resolution	SSO drag?	Global/ LAM?	Dates
CNTRL UM	1.875°x1.25° ($150km$)	Y	Global	1-7/01/2015
NoSSO UM	1.875°x1.25° ($150km$)	N[1]	Global	1-7/01/2015
HR Orog UM	0.06°x0.04° ($5km$)	Y	LAM	1-7/01/2015
LR Orog UM	0.06°x0.04° ($5km$)	Y	LAM	1-7/01/2015
HR IFS	TL1279 ($16km$)	Y	Global	1-7/12/2015
HR NoSSO IFS	TL1279 ($16km$)	N	Global	1-7/12/2015
CNTRL IFS	TCo199 ($50km$)	Y	Global	1-7/12/2015
NoSSO IFS	TCo199 ($50km$)	N	Global	1-7/12/2015

[1] SSO drag removed only over the Himalayan Plateau in NoSSO UM.

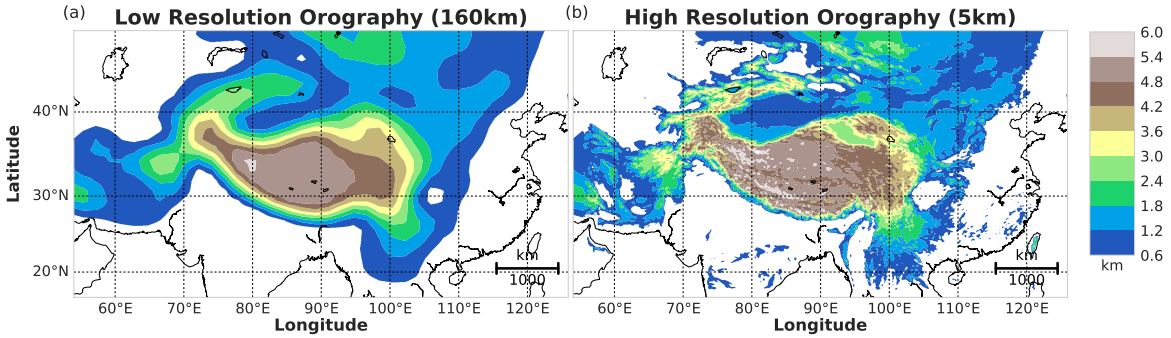

Figure 5.1: Mean resolved orographic height in (a) LR Orog UM and (b) HR Orog UM.

5.3 Impact of resolved versus parameterized orographic drag

We begin by looking at the experiments performed with the MetUM. The impact of the additional resolved orographic drag (HR Orog UM minus LR Orog UM) on the longitudinally averaged zonal winds over the Himalayan region is shown in figure 5.2(a) and the impact of the SSO drag (CNTRL UM minus NoSSO UM) in figure 5.2(b). Despite the simple formulation of these parameterization schemes and the fact that they are based on highly idealised flow, there are several gross similarities in their impacts. The latitudinal position of the peaks in the low-level response are co-located and the drag due to gravity waves is roughly at the right altitude.

There are, however, also several immediately discernible differences to the impacts on the large scale circulation. Most notably, the magnitudes over the latitude range of 25N to 45N are very different, where the SSO drag acts much more strongly on the westerly flow when compared with the additional resolved orography. The depth over which the SSO drag acts is also much larger, extending far up into the northern flank of the jet. The SSO drag acts very strongly at lower altitudes, whereas the largest impact from the resolved orography is predominantly over the peaks of the maximum orography. Although the low-level westerly flow is strongly decelerated by the SSO drag, the low-level easterly flow in the sub-tropical region is not as strongly decelerated when compared with the effect of the additional resolved orography. In the upper atmosphere, where the momentum deposition due to the vertical propagation of gravity waves will dominate, deceleration from the additional resolved orography is

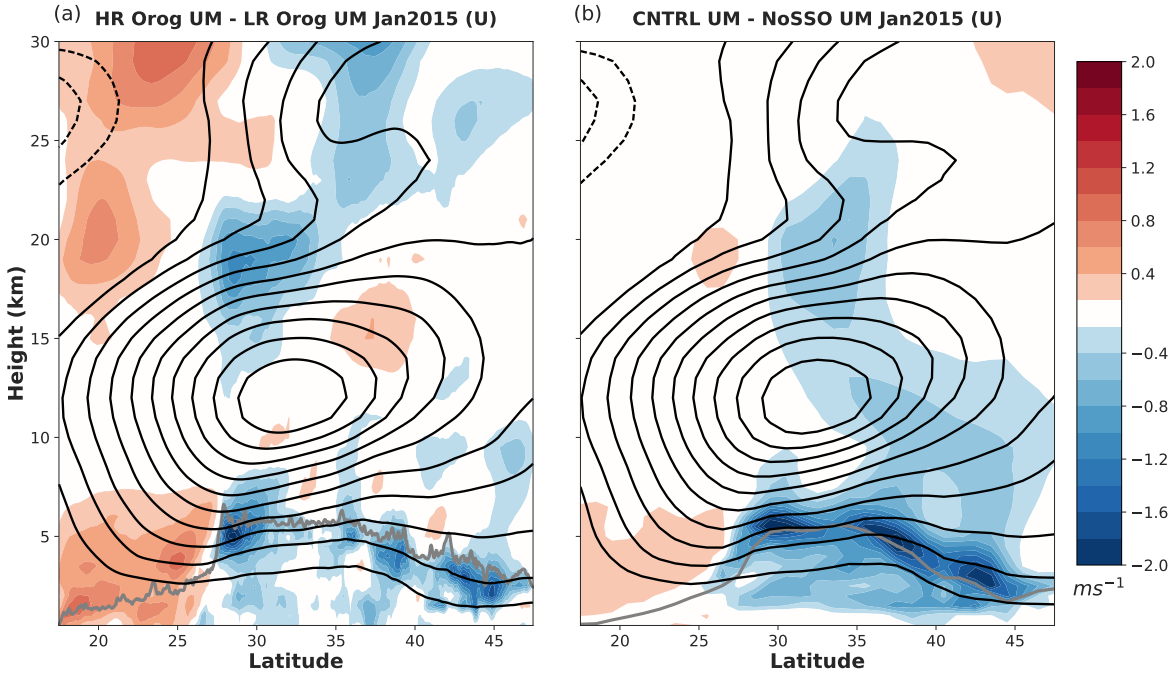

Figure 5.2: Impact on zonal winds averaged over the Himalayan region from (a) additional resolved orographic drag (HR Orog UM minus LR Orog UM) and (b) additional parameterized orographic drag (CNTRL UM minus NoSSO UM). The grey lines indicate the maximum resolved orographic height within a given latitude band. Black contours are the zonal wind in LR Orog UM, with $5ms^{-1}$ contour interval.

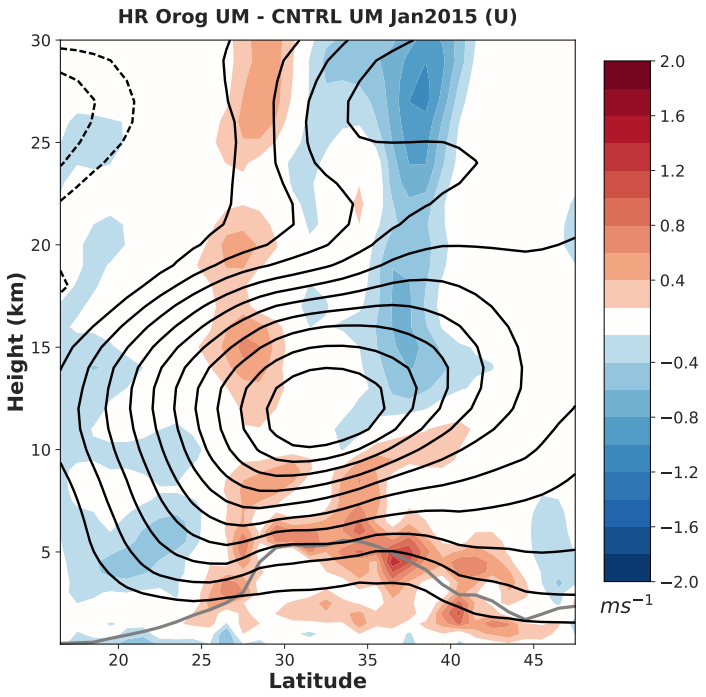

Figure 5.3: Impact on zonal winds averaged over the Himalayan region from increasing horizontal resolution (HR Orog UM minus CNTRL UM). The grey lines indicate the maximum resolved orographic height within a given latitude band. Black contours are the zonal winds in CNTRL UM, with $5ms^{-1}$ contour interval.

slightly larger than that of the SSO drag. The location of the maximum gravity wave deceleration from the parameterized drag, which occurs just above the jet maximum, is also displaced slightly to the north relative to the deceleration from the additional orography. There is very little deceleration from the SSO drag in the upper atmosphere above $25km$, suggesting that the parameterized gravity waves saturate and deposit all of their momentum too low down. Essentially none of the deceleration of the easterlies in the upper atmosphere due to the addition of resolved orography is reproduced by the SSO drag.

Figure 5.3 presents the full response of the zonal winds over the Himalayas going from low to high resolution in the MetUM (i.e. HR Orog UM minus CNTRL UM). This shows the impact of both the additional resolved orography and the change in the parameterized orographic drag on the zonal winds. If the modelled circulation were robust to changes in resolution and the parameterized orographic drag was performing exactly like the resolved orography, there would be no impact of increasing horizontal

resolution and the values in this figure would be small. In fact, the upper level difference in the region of gravity wave breaking is quite small, apart from the large difference in the lower stratosphere between 35N-40N. The impact on the low-level winds, however, is counter to what might be expected from increased resolved orography but not surprising considering the results presented in chapter 4 and figure 5.2. The positive anomaly between 25N-45N in figure 5.3 is due to the large reduction of the SSO drag that is not balanced by an increased in the resolved orographic drag when going to higher resolution, resulting in an acceleration of the low-level winds with increasing resolution.

5.3.1 Short range forecast drift

In order to establish whether the additional resolved orography and the additional parameterized orographic drag are beneficial for the forecasting ability of the model at short lead times, we analyse here the drift relative to the MetUM analysis that is used to initialise the model. This is done by taking the model output for the different MetUM experiments at a lead time of 24 hours and subtracting it from the analysis valid at the same time. Figure 5.4 shows the drift of the zonal winds averaged over the LAM domain in the LR Orog UM and HR Orog UM experiments. The additional orography acts to reduce the magnitude of the drift almost everywhere, excluding the region between $10km$ and $15km$ altitude on the northern side of the jet maximum. The drift indicates that the near surface winds are too strong in the LR Orog UM experiment and this is almost entirely eliminated over the northern most regions with the addition of resolved orography.

The impact of the additional resolved orography (figure 5.2(a)) shows quite good spatial agreement with the drift we see in figure 5.4(a). For example, the negative maximum seen over and above the orographic peak at 28N in figure 5.2(a) acts to oppose the positive drift seen in figure 5.4. However, the negative drift seen on the northern flank of the jet maximum, between $10km$ and $15km$ altitude, is not altered by the additional orography and is perhaps due to some other underrepresented process within the model. It is also possible that this drift is coming from the large scale driving model. Since the boundary conditions of the LAM are those of an imperfect low resolution global model, which itself will have a drift relative to the analysis, the drift over this region may be a symptom of the global model's drift.

Figure 5.5 shows the drift in the NoSSO UM and CNTRL UM experiments. As

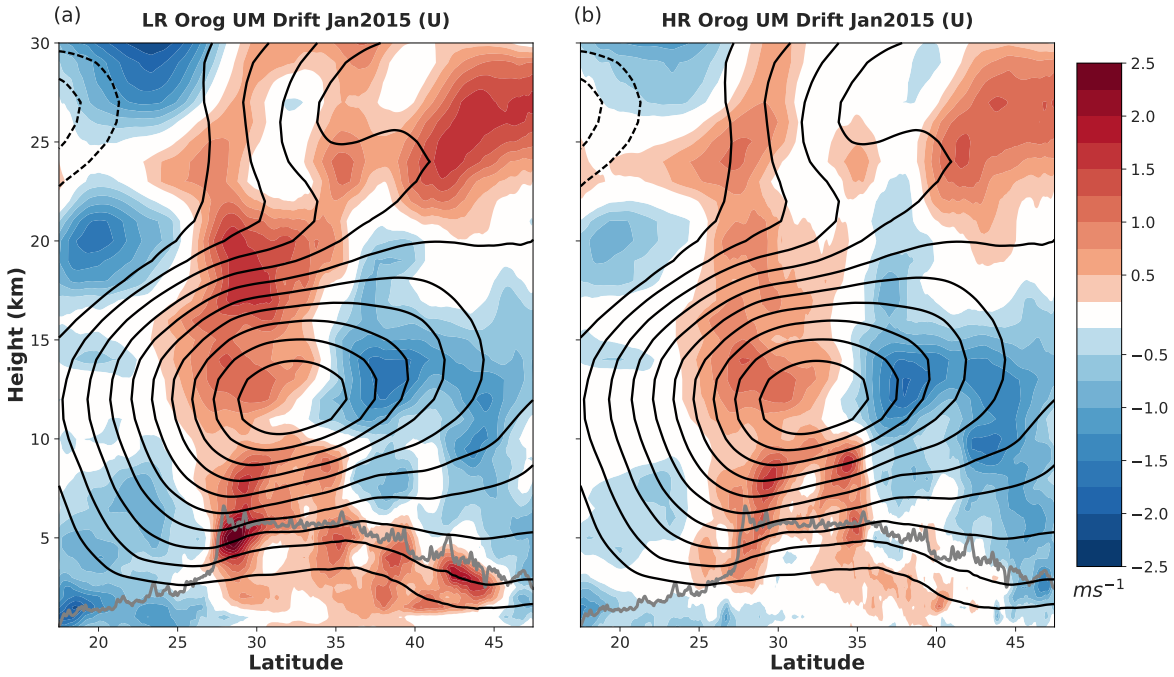

Figure 5.4: Drift in zonal winds at 24 hour lead time for (a) LR Orog UM and (b) HR Orog UM averaged over the Himalayan region. The grey lines indicate the maximum resolved orographic height within a given latitude band. Black contours are the zonal winds in (a) LR Orog UM and (b) HR Orog UM, with $5ms^{-1}$ contour interval.

was the case in the LR Orog UM experiment, without additional orographic drag the low-level flow appears to become too strong over the large orography and directly above the mid-latitude jet maximum. The addition of SSO drag over the Himalayan region acts to reduce the drift substantially, particularly near the surface. However, the drift now becomes negative at the surface over the higher latitudes, suggesting that the SSO drag is acting too strongly there. This is consistent with the findings of chapter 4. In the lower stratosphere, the drift in CNTRL UM indicates that the winds are too westerly just above the jet maximum, where we also found the deceleration due to parameterized gravity wave drag to be too weak when compared with the drag from additional resolved orography (figure 5.3).

We alluded to the idea that some of the drift present in HR Orog UM and LR Orog UM may be coming from the large scale. The fact that the CNTRL UM, which is the driving model for the LAM, also exhibits the larger negative drift to the north of the jet maximum gives us reason to believe that some of the drift seen in the LAM experiments are coming from the large scale. Nevertheless, the main point to take away

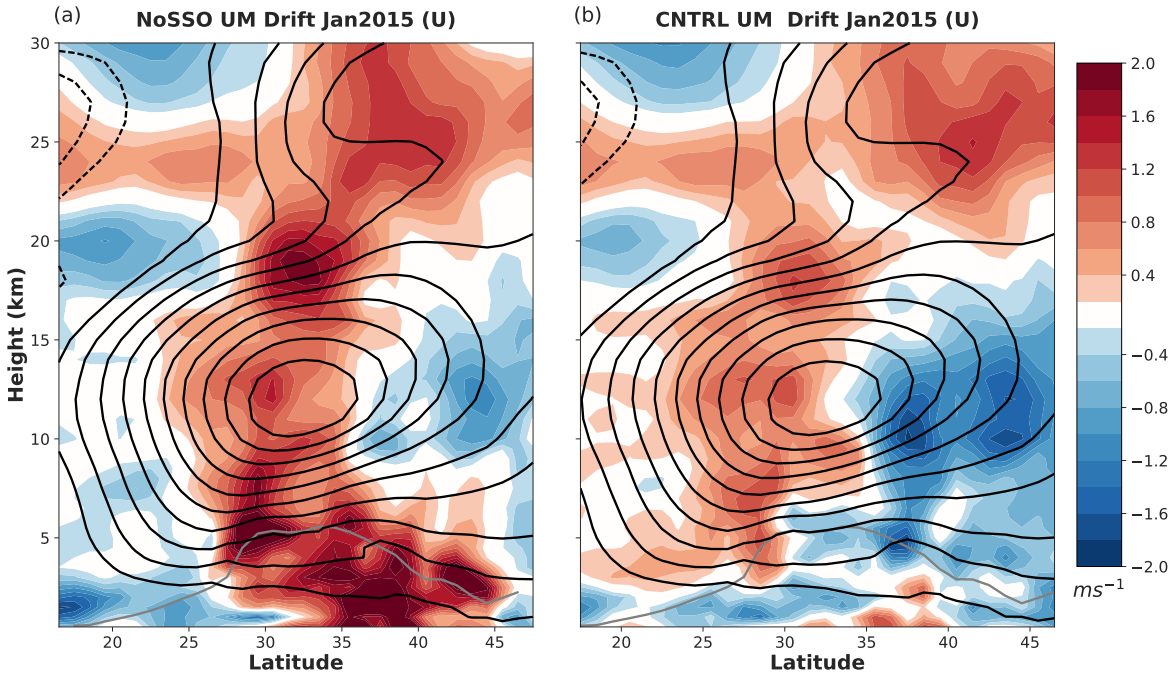

Figure 5.5: Drift in zonal winds at 24 hour lead time for (a) NoSSO UM and (b) CNTRL UM averaged over the Himalayan region. The grey lines indicate the maximum resolved orographic height within a given latitude band. Black contours are the zonal winds in (a) NoSSO UM and (b) CNTRL UM, with $5ms^{-1}$ contour interval.

from these drifts is that the additional resolved orography is reducing the model drift and the SSO drag is too large in CNTRL UM, which leads to a drift in CNTRL UM of the opposite sign to NoSSO. We note, however, that the relative improvement seen when adding additional resolved orography versus adding SSO drag over the Himalayas is quite similar. This is consistent with several other studies that have demonstrated the benefits of implementing parameterizations for orographic drag in models.

5.3.2 Momentum budgets

To understand how the circulation responds to the increased resolved orography, we diagnose the zonal momentum budget over the Himalayan region using the LAM output. The vertically integrated zonal momentum budget is given by:

$$\overbrace{\frac{\partial < \rho u >}{\partial t}}^{\text{dudt}} = \overbrace{-\frac{1}{r\cos\phi}\frac{\partial < \rho uu >}{\partial \lambda} - \frac{1}{r\cos^2\phi}\frac{\partial < \rho uv > \cos^2\phi}{\partial \phi}}^{\text{Fluxes}}$$
$$\overbrace{-\frac{1}{r\cos\phi}\left[\frac{\partial < p >}{\partial \lambda} + p_0\frac{\partial z_0}{\partial \lambda}\right]}^{\text{Pdrag}} + \overbrace{< fv\rho >}^{\text{Cor}} - < \rho 2\Omega w\cos\phi > + \overbrace{< \rho F_\lambda >}^{\text{Param}} \quad (5.1)$$

where u is the zonal wind, v is the meridional wind, w is the vertical wind, ρ is density, r is the distance from the centre of the Earth, ϕ is latitude, p is pressure, f is the Coriolis parameter, Ω is the rotation rate of the Earth and F_λ is the sum of the tendencies from parameterized processes. F_λ contains tendencies from the boundary layer, the orographic drag, the convective entrainment of momentum and the spectral gravity wave drag schemes, with the latter two being negligible when (5.1) is evaluated at the surface. The notation $< .. >= \int_{z_0}^{ztop} dz$ indicates a vertical integral from the model lid to the surface. At the surface, $< \rho 2\Omega w\cos\phi >$ and $< fv\rho >$ are small. In a periodic domain, the first term in Pdrag and Fluxes disappears.

Figures 5.6(a) and 5.6(b) show the momentum budget terms evaluated at the surface and averaged in the longitudinal direction over the Himalayas for the LR Orog UM and HR Orog UM experiments, respectively. The Pdrag and Coriolis terms are summed to represent the ageostrophic contribution to the momentum budget. While the overall shape of the terms is very similar across the two experiments, as one would expect given that they are fed with the same large scale boundary conditions, HR Orog UM clearly has a lot more fine scale structure. This is particularly noticeable in the Pdrag term. There is also a large difference in the Fluxes term, which is coming predominantly from the meridional flux term (ρuv), since the zonal term is identical in the two experiments when an average over the domain is taken. This is also the case for the $\frac{\partial <p>}{\partial \lambda}$ term in Pdrag, due to the boundary conditions being identical in the two experiments. The parameterized drag changes between the two experiments act to damp the response from the additional resolved orographic drag slightly but these differences are negligible.

Differences between the terms will give us an indication of how large the impact of the additional resolved orography is and should give a better understanding of how large the parameterized orographic drag terms that are output by CNTRL UM should be. The additional resolved orography is likely to increase the amplitude of the verti-

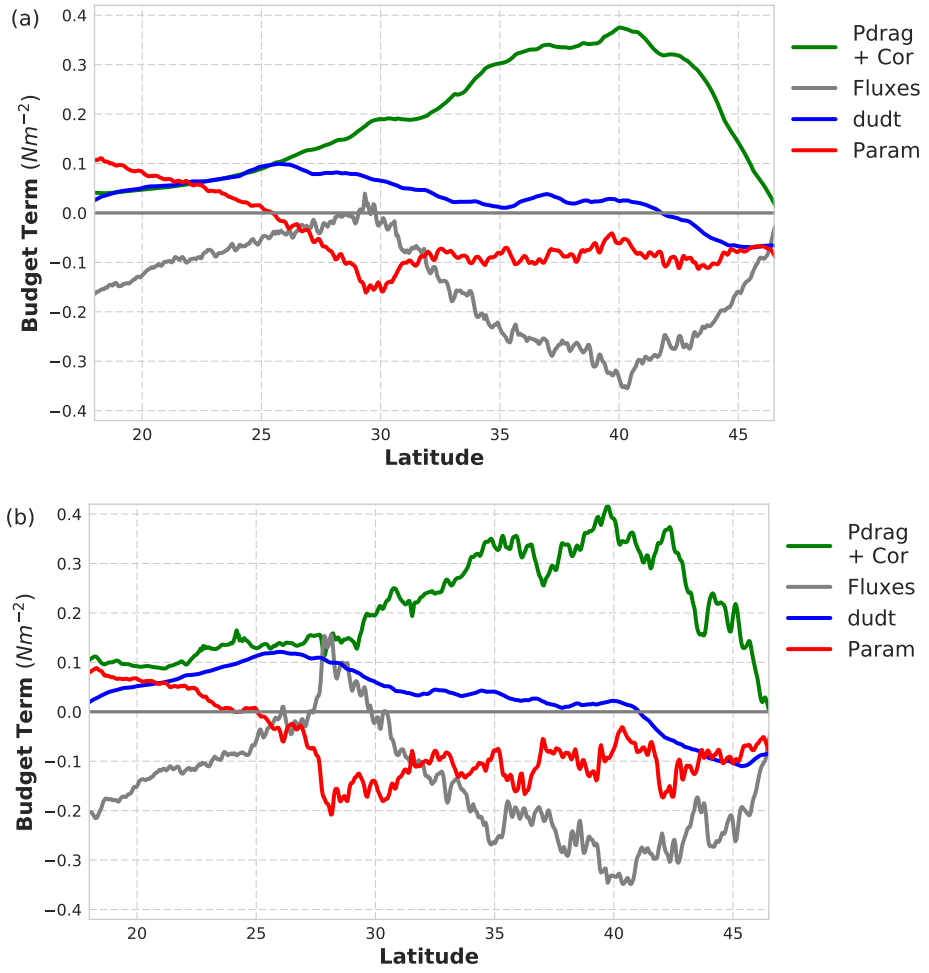

Figure 5.6: Dominant momentum budget terms in (5.1) for (a) LR Orog UM (b) HR Orog UM.

cally propagating gravity waves generated by topography. Since the amplitude of the mountain has increased, the amplitude of the vertical displacement of the flow will also increase. Typically, these vertically propagating waves, although they also propagate substantial distances in the horizontal, saturate and deposit their momentum in regions where their amplitudes become too large due to a decrease in the wind speed and density with height. This means that they are likely to break above the jet maximum, as is seen in figure 5.2, where the winds weaken and the density is low. In the interior of the atmosphere this vertical transport of momentum from the surface by gravity waves is given by ρuw.

Figure 5.7(a) shows the change (HR Orog UM minus LR Orog UM) in the term ρuw

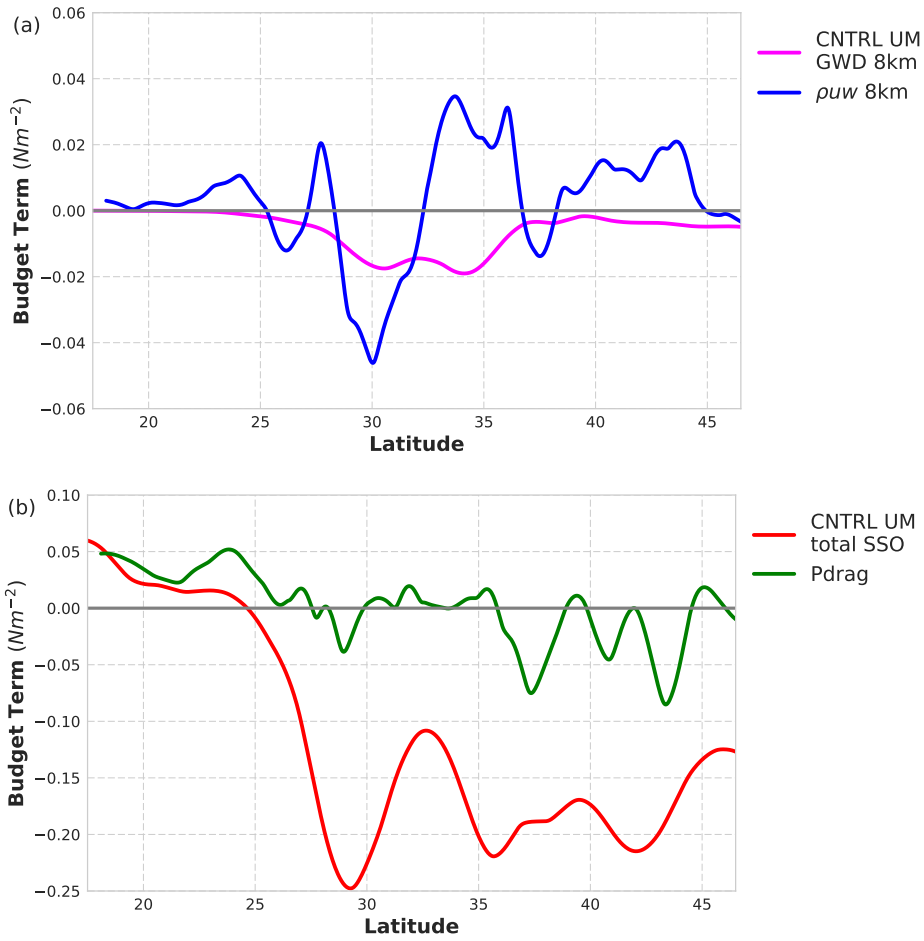

Figure 5.7: (a) Change in ρuw (HR Orog UM minus LR Orog UM) and the parameterized orographic gravity wave drag from CNTRL UM evaluated at $8km$. (b) Change in Pdrag (HR Orog UM minus LR Orog UM) and the total parameterized orographic drag from CNTRL UM evaluated at the surface.

from additional resolved orography evaluated at $8km$, coarse grained onto the CNTRL UM grid. Also shown is the stress from the gravity wave drag component of the SSO parameterization scheme in CNTRL UM evaluated at $8km$. Firstly, we note that the additional resolved orography leads to a vertical transport of negative momentum (i.e. $\rho uw < 0$) in the latitude band 28N to 32N, which is consistent with what is seen in figure 5.2 where we saw a deceleration of the flow in the upper atmosphere over this region. The positive vertical momentum flux between 32N and 37N shows up as an acceleration of the flow at $\sim 14km$. Comparing now the resolved momentum fluxes with the parameterized stress we see that the positive fluxes are not represented and

that the resolved fluxes are generally of a larger magnitude, as well as the maximum of the parameterized drag being displaced to the north.

Figure 5.7(b) shows the difference (HR Orog UM minus LR Orog UM) in the Pdrag term evaluated at the surface, coarse grained onto the CNTRL UM grid, along with the total parameterized orographic drag at the surface from CNTRL UM. The parameterized SSO drag at the surface, which comes predominantly from the drag due to blocked flow, is much larger than the resolved drag, with differences as large as a factor of ten at approximately 29N, as was seen earlier in section 5.3. This confirms that the change in the surface drag coming from the resolved orography, even at very high resolutions, is not nearly as large as the parameterized orographic drag at the climate model resolution. What this suggests is that there is something about the formulation or settings of the parameterization scheme that is not representative of the unresolved flow or topography in such complex terrain.

5.4 Suitability of the parameterization scheme for complex flow

The shortcomings of the parameterization scheme over this region may be due to the complex nature of the flow and the proximity of the mountain range to the strong upper level westerlies. We will briefly describe the relevant aspects of the parameterization formulation here but for a full explanation of its implementation in the MetUM see Vosper et al. (2016) and section 2.2.

The surface stress from vertically propagating gravity waves is parameterized using the expression:

$$\mathbf{F}(x, y) \propto \rho \mathbf{U} N h_{eff}^2 b \tag{5.2}$$

where b is the half width of the mountain in the direction of the wind vector, $\mathbf{U}$ is the wind vector, N is the static stability and h_{eff} is the portion of the mountain that is able to generate gravity waves. h_{eff} is given by $h_{eff} = h - Z_b$ with h being the height of the sub-grid mountain and Z_b being the depth, measured from the surface, over which the flow is blocked.

Z_b is calculated from the depth averaged Froude number, $F_{av} = U_{av}/N_{av}h$. The

parameterization scheme assumes height independent background flow and, as a result, F_{av} is a function of the vertically averaged winds (U_{av}) and static stability (N_{av}) over the height of the sub-grid mountain (h). The blocking depth is then calculated using:

$$Z_b = h\left(1 - \frac{F_{av}}{F_c}\right). \tag{5.3}$$

F_c is the critical Froude number and determines the threshold between completely blocked flow and gravity wave generation. F_c takes a value of 4 in the MetUM, although it is often treated as a tuneable parameter. If the winds are strong and the static stability is small, there will be more gravity wave generation and less low-level blocking, and vice versa. This method of calculating the Froude number is not identical to the original formulation (see eq. 9 of Lott and Miller (1997)), in which the blocking depth is defined as the height at which the integral of $\int_{Z_b}^{3\sigma} \frac{N(z)}{U(z)} dz \geq H_{crit}$ is solved for Z_b, where H_{crit} is some critical value. While this may treat the problem of wind shear at low-levels, it does not account for discontinuities in N and U or strong wind shear at upper levels.

In the MetUM, the drag (on the atmosphere) from the low-level parameterized orographic blocking is then determined via:

$$D_b(z) = -C_d \rho l(z) \frac{\mathbf{U}|\mathbf{U}|}{2} \tag{5.4}$$

where C_d is a tuneable drag coefficient and $l(z)$ is the horizontal extent of the sub-grid mountain along the direction of the wind vector and is given by:

$$l(z) = 2b\left(\frac{Z_b - z}{z + \sigma}\right)^{1/2} \tag{5.5}$$

where z is the height from the surface and σ is the standard deviation of the sub-grid orography. This formulation means that the parameterized gravity wave drag and blocking drag are intimately linked through the Froude number, with larger blocking meaning less gravity wave generation. To first order, in the presence of large blocking the low level winds decelerate and lead to a positive feedback that would inhibit gravity wave generation further. In sections 5.3 and 5.3.2 we showed that the low-level parameterized drag coming from the blocking was too large and that the drag from gravity waves in the upper atmosphere was too small when compared with the corresponding

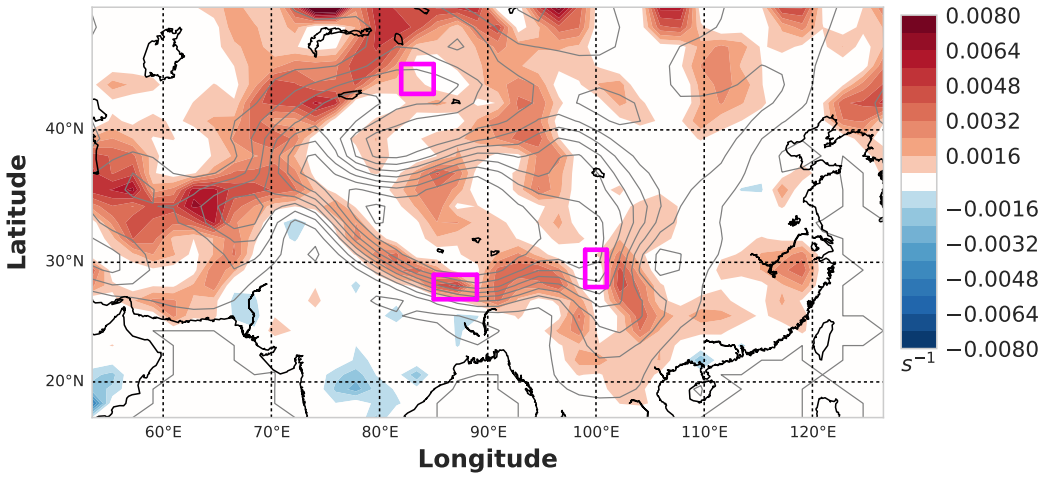

Figure 5.8: Vertical shear of the zonal wind in regions where winds change direction over the height of the sub-grid orography, given by $[u(z) - u(0)]/h$, for CNTRL UM. Magenta boxes indicate regions of vertical profiles evaluated in figures 5.10, 5.11 and 5.12.

result obtained with the additional resolved orography. This suggests that the gravity wave drag deficiencies are potentially due to the overly large blocking drag near the surface.

The overly large blocking drag may be due to the unsuitability of the approximation that the flow is independent of height over this region. This seems an inconsistent approximation when we consider the fact that, in models with low horizontal resolutions, the sub-grid mountain heights may be several kilometres over the Himalayan region and the wind shear may be very large. This is compounded by the prospect that the flow may not be single signed over the depth of the sub-grid orography. As an illustration of this and to indicate the regions over which this approximation might be most problematic, figure 5.8 shows the shear of the time mean zonal wind over the height of the sub-grid orography ($du/dz = [u(h) - u(0)]/h$) only in grid-boxes where the wind changes direction over the depth of the sub-grid orography (i.e. where $u(0)u(h) < 0$). We see that there are several regions over which this is the case, particularly on the slopes of the Himalayas. Looking at the mean blocking depth (Z_b) calculated by the parameterization scheme (figure 5.9) it becomes clear that the blocking depths are very large over the regions where the wind shear is large. In fact, over some of these regions almost all of the sub-grid flow is blocked such that no gravity wave generation occurs. Of course the winds are not the only aspect controlling the depth of the blocking layer,

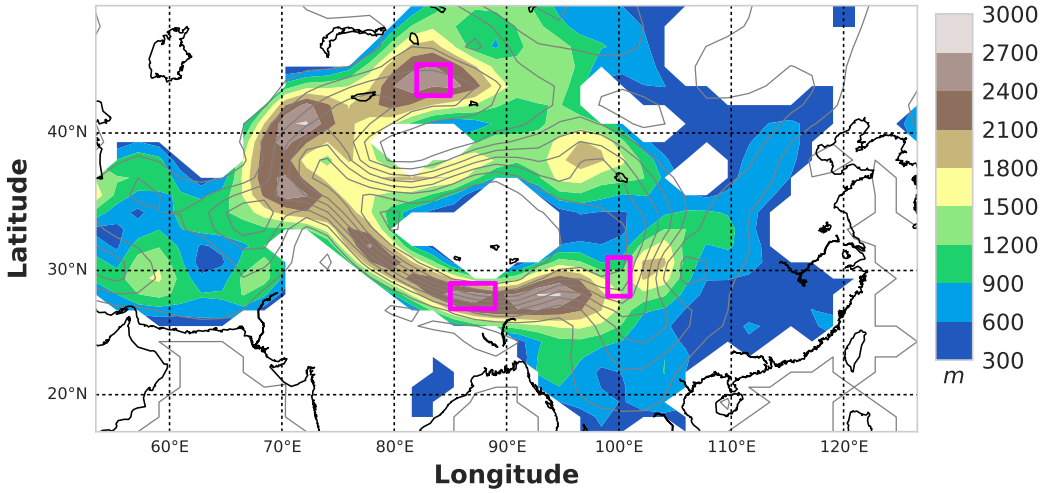

Figure 5.9: Diagnosed blocking depth as given by (5.3) for CNTRL UM.

since it depends also on the height of the sub-grid orography and the static stability, through the Froude number. One can see that there are certain regions where the large wind shear and deep blocking are not co-located. Over these regions, we generally see that either the winds are weak and single-signed (an example of which is shown later in figure 5.11) or the static stability is high.

It becomes clear why the blocking depths are large over these regions of strong wind shear if we consider that, when the winds change direction rapidly, the vertical average of the winds (U_{av}) will be very small compared with the winds aloft causing F_{av} to become small and, thus, the blocking depth to be large. To test this hypothesis, we consider three different scenarios: one in which the winds change sign over the sub-grid mountain height, leading to large blocking depths and, thus, large blocking drag; one in which the wind shear is weak but the winds are single signed and weak and, thus, the blocking depth is large; and, finally, one in which the wind speeds are strong, the blocking depth is small but, as a result of the large wind speeds, the blocking stress is large. Figure 5.10(a) shows the vertical profile of the wind as a function of height above the surface for grid-boxes within the region 27N-29N, 91E-97E, as indicated by the southern most magenta box in figure 5.9. This is the case with large wind shear. The location of the circles indicate the depth of the blocked layer. Many of these wind profiles show a very strong wind shear going from weak easterlies at the surface to strong westerlies in the upper atmosphere, as is expected from the location of the topography relative to the mid-latitude jet. We also note from the height of the blocked layer within

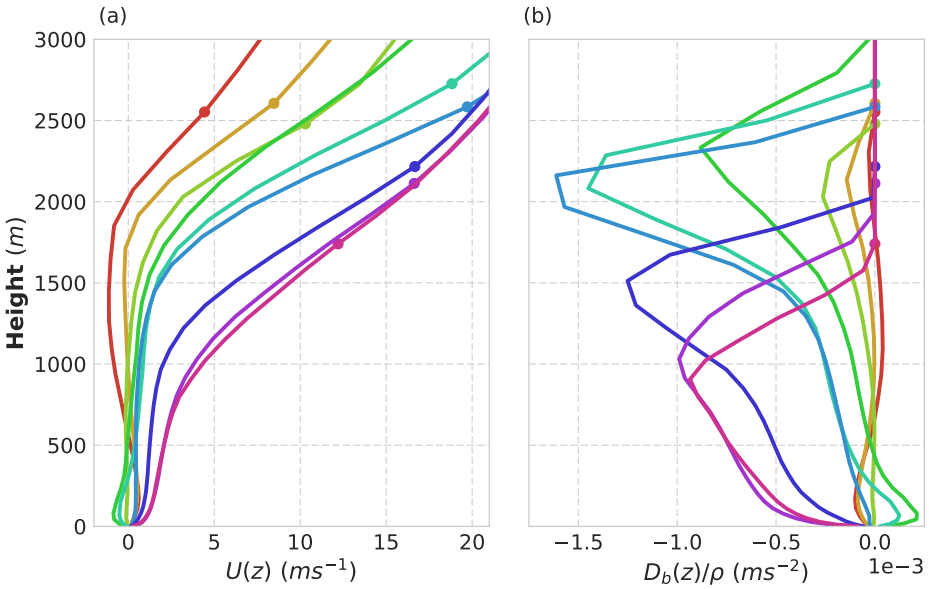

Figure 5.10: Vertical profiles of (a) zonal winds and (b) blocking tendencies (given by (5.4)) in grid-boxes over the region 27N-29N, 85E-89E for CNTRL UM.

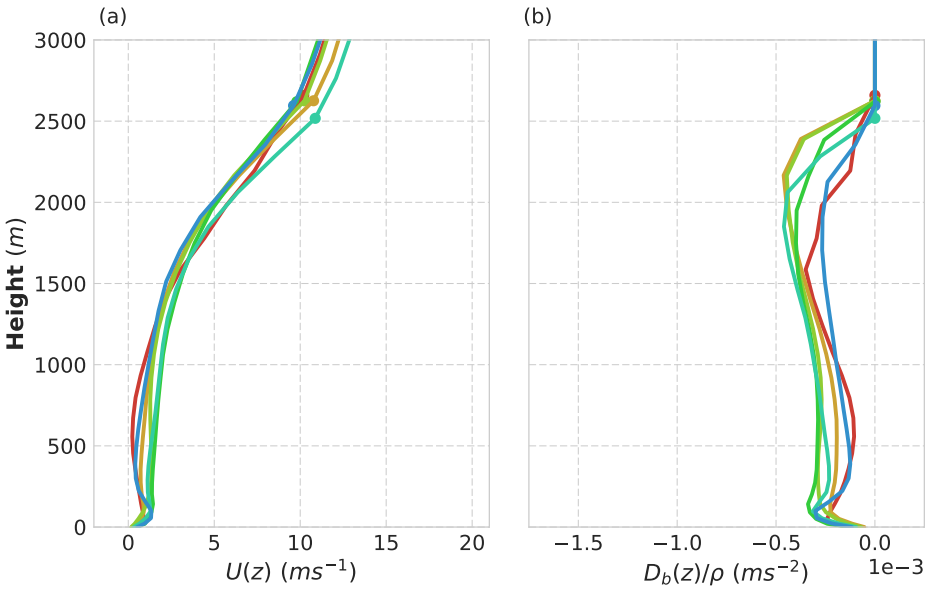

Figure 5.11: Vertical profiles of (a) zonal winds and (b) blocking tendencies, given by (5.4), in grid-boxes over the region 42.5N-44.5N, 82E-85E for CNTRL UM.

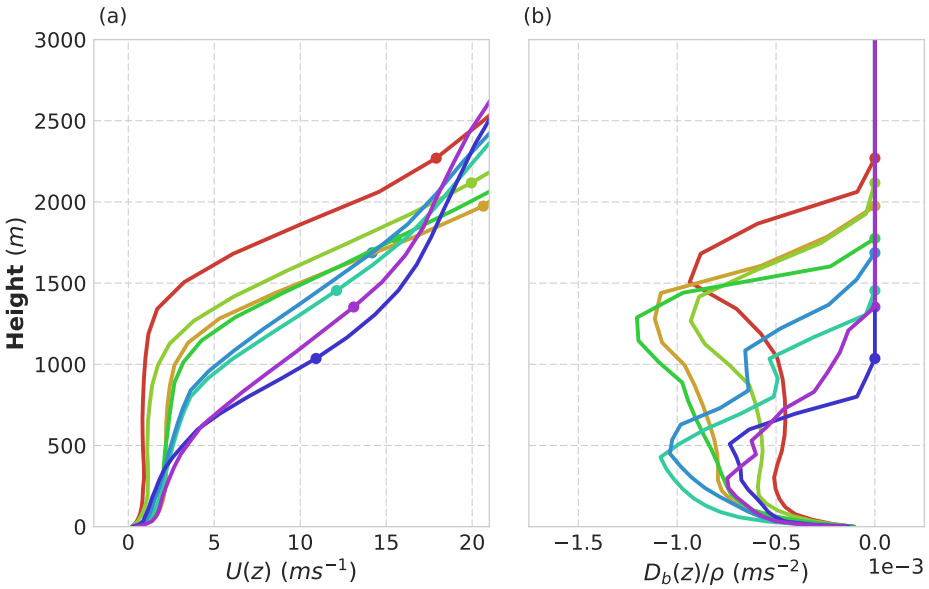

Figure 5.12: Vertical profiles of (a) zonal winds and (b) blocking tendencies in grid-boxes over the region 28N-31N, 99E-101E for CNTRL UM.

each grid-box that the blocking depth scales with the wind-shear such that grid-boxes with large wind shear going from negative to positive values have large blocking depths. Figure 5.10(b) shows the corresponding blocking tendencies ($\frac{\partial u}{\partial t} = D_b(z)/\rho$) from the parameterization scheme. What we find is that the parameterized drag in some of the grid-boxes is weakly positive within the lower levels, such that it is decelerating the easterlies, and then becomes very large and negative in the upper levels, where the winds become strong and westerly. This behaviour leads to an overemphasis of the drag at upper levels due to the overestimation of the blocking depth.

Figure 5.11 shows the same as in figure 5.10 but for a region in which there is weaker wind shear and the winds are generally single signed, indicated by the northern most magenta box in figure 5.9. The blocking tendencies are much smaller and more constant with height compared with 5.10. The blocking depth is large over this region as a result of the weak westerly winds near the surface. In contrast, figure 5.12 now shows the profiles for a case with strong winds and we immediately see that the blocking depths are much smaller, which would indicate more gravity wave generation. The latter two cases are more in line with what is expected from the parameterization scheme and the assumed flow. Over regions such as these, we would, therefore, expect the scheme to be behaving in a more physically consistent manner. In regions of

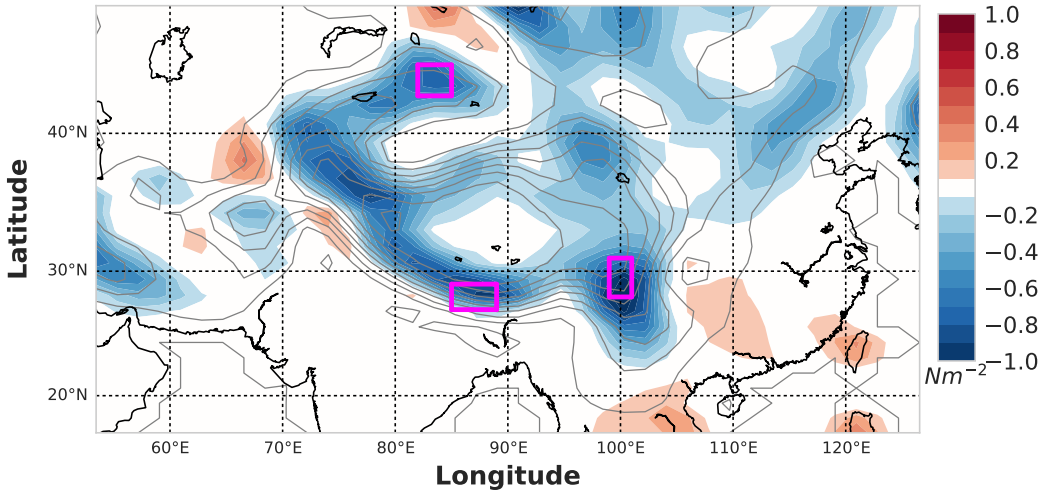

Figure 5.13: Vertically integrated parameterized orographic blocking drag from CNTRL UM.

strong vertical wind shear (particularly where the winds change direction), however, the blocking depths may be overestimated, resulting in the very large surface stress from parameterized orographic blocking drag seen over the Himalayan regions, the longitudinal and latitudinal structure of which is shown in figure 5.13.

The work presented in chapter 4 also highlighted the large resolution sensitivity of the parameterized orographic drag in mid-latitudes, with values of orographic surface drag decreasing rapidly with increasing resolution. This large change may also be due to the large wind shears over these topographic regions. Any decrease in the sub-grid mountain height will reduce the blocking depth and, since the wind shear is so large at the top of the blocked layer, even small changes in the blocking depths will have a substantial impact on the magnitude of the drag due to blocking.

5.5 Comparison with ECMWF IFS

We now consider the impact of resolved versus parameterized orographic drag in the ECMWF IFS. Figures 5.14(a) and 5.14(b) show the impact of additional resolved orography (HR NoSSO IFS minus NoSSO IFS) and the SSO drag (CNTRL IFS minus NoSSO IFS), respectively. Firstly, we point out that the magnitude of the differences in the IFS are much smaller than those of the MetUM; note that the contour interval is

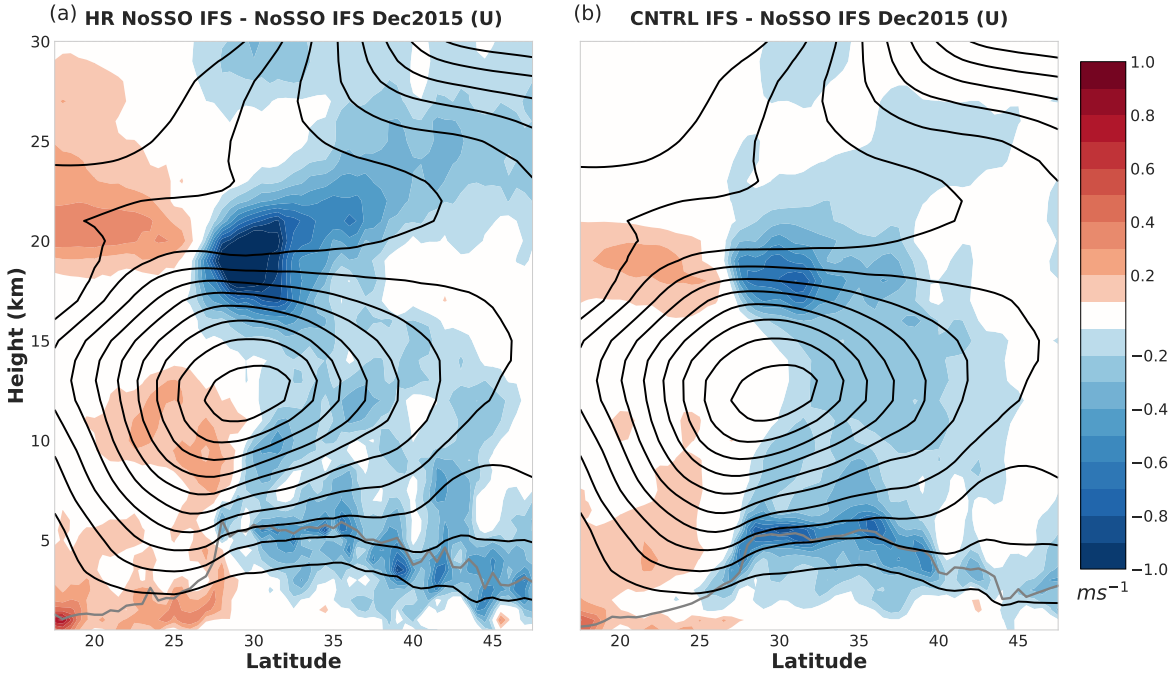

Figure 5.14: Impact on zonal winds averaged over the Himalayan region from (a) additional resolved orographic drag (HR NoSSO IFS minus NoSSO IFS) and (b) parameterized orographic drag (CNTRL IFS minus NoSSO IFS). The grey lines indicate the maximum resolved orographic height within a given latitude band. Black contours are the zonal winds in CNTRL IFS, with $5ms^{-1}$ contour interval.

halved. The weaker impact due to additional resolved orography, although the upper level response is of a similar magnitude to the MetUM, can be explained by the fact that the change in resolution is much smaller going from $\sim 50km$ to $\sim 16km$ than going from $\sim 150km$ to $\sim 5km$. As for the weaker impact from the parameterization scheme, this supports the findings of chapter 4.4 and the findings from the WGNE drag inter-comparison, which showed that the vertically integrated parameterized orographic drag was much smaller in the ECMWF IFS compared with the MetUM at comparable resolutions. This difference was partially balanced by larger vertically integrated boundary layer drag employed in the ECMWF IFS. CNTRL IFS is also at a higher resolution compared with CNTRL UM and will, therefore, have less SSO drag to begin with.

Overall, the response from resolved orography versus parameterized orographic drag is very similar in the ECMWF IFS. However, like in the MetUM (figure 5.2), the low-level parameterized orographic drag is larger than what is produced from the additional

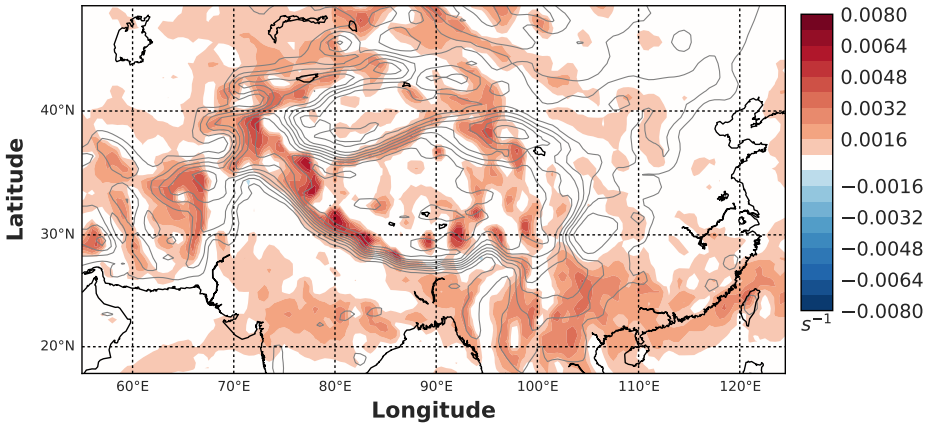

Figure 5.15: Vertical zonal wind shear in regions where winds change direction over a height of $2km$, given by $[u(2km) - u(0)]/2km$, for CNTRL IFS.

resolved orography over the region 25N to 30N, although the discrepancies are much smaller and the resolved orography actually leads to larger drag over the northern parts of the topography. The SSO drag in the IFS also lacks some of the positive near-surface and upper level anomalies over the subtropical region, even acting in the opposite sense to the additional resolved orography over ∼25N to 30N. As in the MetUM, the deceleration directly above the jet maximum coming from the gravity wave drag is much larger for the increase in resolution compared with the parameterized orographic drag. This is consistent with the notion that, if the low-level parameterized orographic drag is large the gravity wave drag component will be small. In both models the gravity wave drag parameterization scheme is able to deposit momentum in roughly the correct vertical and latitudinal position, when compared with the additional resolved orography, giving us confidence that the theory and implementation of this part of the scheme is in accordance with the full set of resolved equations.

For completeness, figure 5.16 presents the full response of the zonal winds over the Himalayan Plateau going from low to high resolution in the ECMWF IFS (i.e. HR IFS minus CNTRL IFS). The increased resolution leads to increased gravity wave drag above the jet maximum, indicative of the parameterized gravity wave drag in CNTRL IFS being less than that coming from the additional resolved orography. Similarly to the MetUM, the surface winds increase with increasing resolution as a result of the large resolution sensitivity of the parameterized orographic drag. The formulation of the Froude number in the ECMWF IFS is more inline with the method presented in

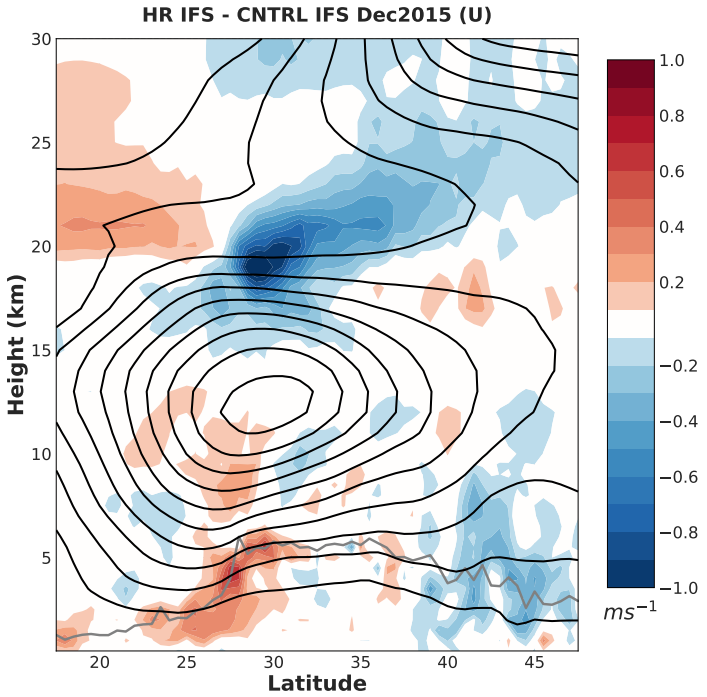

Figure 5.16: Impact on zonal winds averaged over the Himalayan region from increasing horizontal resolution (HR IFS minus CNTRL IFS). The grey lines indicate the maximum resolved orographic height within a given latitude band. Black contours are the zonal winds in CNTRL IFS, with $5ms^{-1}$ contour interval.

Lott and Miller (1997), which may explain why the discrepancies between the high resolution and low resolution simulations are smaller when compared with that of the MetUM.

Figure 5.15 shows the vertical wind shear over regions in which the winds are changing direction from the surface up to $2km$, similarly to figure 5.8. We again see that the winds turn substantially with height, particularly on the slopes of the Himalayan Plateau. Figure 5.15 also demonstrates that some of the strongest wind shear occurs over the southern edge of the Himalayan Plateau, where we also see the large positive wind anomaly in figure 5.16. It is, therefore, likely that the large reduction of the parameterized drag with increasing resolution over these mid-latitude regions are a result of the complexity of the flows.

5.6 Conclusions

Using high resolution global and LAM simulations analysed over the Himalayan Plateau we were able to address some of the questions that arose from chapter 4 and that are listed in the introduction of this chapter. We showed that the addition of small scale orography in a high resolution limited area model led to a deceleration of the mean flow at the surface as well as a deceleration of the flow aloft, which can be attributed to the momentum transport by propagating gravity waves generated by orography. Broadly speaking, the impacts on the circulation from resolved orography were reproduced by the orographic drag parameterization scheme implemented in a low resolution model. The magnitude of the parameterized drag near the surface, however, was substantially larger and the deceleration of the sub-tropical easterly flow was not reproduced by the parameterization scheme. This meant that increasing the model horizontal resolution, including both the change in resolved orography and the change in the parameterized orographic drag, lead to an acceleration of the low-level winds.

Differences between the starting analysis and the model at a lead time of 24 hours support the findings of chapter 4. The parameterized orographic drag at the surface is too large in the MetUM, leading to a drift in the model identifiable over short timescales. Nevertheless, the drifts indicate that the parameterized orographic drag significantly improves the forecast when compared to an experiment without any drag. This improvement is similar in nature to, but weaker than, that seen from increasing the orographic resolution.

Using momentum budget diagnostics over the limited area domain, we were able to quantify the differences in the surface drag coming from the individual components of the parameterization scheme and the additional resolved orography. A comparison of the change in the vertical momentum fluxes (ρuw) when adding high resolution orography with the parameterized gravity wave stress suggests that the parameterized orographic gravity wave drag is too small and displaced to the north relative to the resolved drag. The total resolved orographic drag at the surface changes very little with increasing resolution, even when going to very high resolutions, and the magnitudes are consistent with both chapter 4 and Brown (2004). This suggests that the resolved orographic drag is not a linear function of resolution over these regions but, instead, approaches some limit at relatively low resolutions. This is to be expected to some extent due to the intrinsically mesoscale nature of the drag. For example, short,

evanescent mountain waves produce substantially less drag for a number of reasons (including non-hydrostatic effects) than longer, vertically propagating mountain waves (Gill, 1982).

Looking at the complexity of the flow, specifically the vertical wind shear, we hypothesised that the blocking depths may be unrealistically large over regions where the winds change direction with height. Our reasoning is as follows. A vertical average of the wind over a region of strong vertical wind shear, in particular where the winds change sign in the vertical, leads to small depth-averaged wind values. This causes the blocking depths to become large, despite the winds being large aloft. The blocking drag is, therefore, applied over a deep layer intersecting westerlies aloft and dramatically decelerating them. We concluded that this may partly explain why the blocking stress is so large (and unrepresentative of the resolved orographic drag) over the Himalayas, as well as why the parameterization scheme is so sensitive to model resolution over this region.

Finally, we used another comprehensive operational model, the ECMWF IFS, to determine whether the differences between the impact of resolved versus parameterized drag that were found in section 5.3 are model dependent. While the periods of integration are different, we found that, as with the MetUM, the ECMWF IFS low-level blocking parameterization also over-estimates the drag relative to the resolved drag and that the blocking parameterization is not able to capture the drag on easterly winds sufficiently. The total impact of increasing the model's horizontal resolution again reveals the inability of the parameterization scheme to reproduce the drag from the resolved orography and to maintain an equivalent total orographic drag across resolutions, particularly over regions with strong vertical wind shear.

This work motivates the need for further investigation into how best to deal with regions of strong vertical wind shear over complex topography. An obvious first step may be to reduce the factor by which the sub-grid mountain height is multiplied, which would reduce the depth over which the winds are average and, in turn, reduce the wind shear over the sub-grid mountain. However, Vosper et al. (2016) showed that, whilst this parameter can control the accuracy of the parameterized orographic drag, its optimal value differs for different topographic regions. This means that, while altering this parameter may be beneficial for the Himalayas, it may degrade the accuracy of the parameterization scheme over another region. It is, therefore, desirable to seek a

more physically based solution, in which the parameterization scheme is re-formulated to better account for the vertical wind shear.

Chapter 6

The modulation of stationary waves, and their response to climate change, by parameterized orographic drag

All of the work in this chapter has been published in van Niekerk et al. (2017).

6.1 Introduction

It is well known that the wide range of sea surface temperatures (SST) and sea-ice changes seen across climate models play a major role in the spread seen in the circulation response to climate change (Manzini et al., 2014). The role of the climatological basic state, and biases therein, however, is less clear. Previous studies have recognised the importance of model fidelity for predictive skill on seasonal timescales (Kharin and Scinocca, 2012; Delsole and Shukla, 2010) and have shown that there are relationships between the climatological basic state and the response to climate change (Sigmond and Scinocca 2010, Shepherd 2014 and references therein). It is therefore a worthwhile exercise to investigate the sensitivity of the circulation response to climate change to a reduction in model bias in a controlled way, such as changes in the climatological basic state brought about by changes in orographic drag parameterization. This chapter aims to address this issue by first investigating the impact that varying orographic drag parameters has on the circulation within a comprehensive global circulation model and

then asking the question: does the circulation sensitivity to parameterized orographic drag matter for the climate change response?

The structure of this chapter is as follows. In section 6.2 we describe the experimental design, model setup, experiments performed and the details of diagnostics used in our analysis. In section 6.3 the response of the climatological zonal and meridional winds to systematic variations in the magnitude of parameterized drag is investigated. The response of these two wind components are tied together by looking at the relationship between the latitudinal position of the zonal winds and the stationary wave amplitudes in both reanalysis and our experiments. The implications of this for the response to climate change in our experiments are described in section 6.4. Finally, the conclusions are synthesised and implications are discussed in section 6.5.

6.2 Experimental setup

We perform controlled experiments with a single model, the Canadian Fourth Generation Atmospheric Global Climate Model (CanAM4.1). CanAM4.1 has a spectral dynamical core and uses a hybrid vertical pressure coordinate system (Laprise and Girard, 1990). Providing the atmospheric component to the Canadian Earth System Model (CanESM), it makes up part of the CMIP5 ensemble. The configuration employed in this study is that of a triangular truncation at T63, resulting in a (Gaussian) grid point resolution of 192×96 with a physics grid at a resolution of 128×64 in the longitudinal and latitudinal directions, respectively, and 49 levels in the vertical extending to 1hPa. Full details of the model dynamics and physics can be found in Scinocca et al. (2008) and von Salzen et al. (2013).

Repeated annual cycle boundary conditions of SSTs and sea-ice are prescribed so as to remove atmosphere-ocean and sea-ice feedbacks as well as the additional interannual variability of the climate system that arises from these. In what we refer to as the $1 \times CO2$ experiments, the atmospheric concentration of CO_2 is fixed at pre-industrial levels and sea-ice and SST fields are generated using 100 years of data from a preindustrial ocean-atmosphere coupled simulation performed with CanESM4.1. In the climate change experiments, referred to as the $2 \times CO2$ experiments, CO_2 is doubled and SSTs and sea-ice are also derived from coupled simulations, in which CO_2 is doubled relative to pre-industrial levels. The doubled CO_2 coupled simulations

are run for 140 years and a climatological annual cycle of SSTs and sea-ice is derived from the final 30 years, at which point global mean SSTs have reached approximate equilibrium.

The global mean annual mean surface temperature perturbation is $\sim 3.5K$ in these experiments, placing it near the 8.5 representative concentration pathway (RCP8.5) response in the CMIP5 multi-model mean at the end of the 21st Century (Golledge et al., 2015). Both the response to climate change and the response to perturbations in the parameterized drag are largest during Northern Hemisphere (NH) winter, which is why this study is focused on the mean over December-January-February (DJF) and all analysis is performed over this period.

6.2.1 Orographic drag parameterization

CanAM4.1 employs the orographic drag parameterization scheme described by Scinocca and McFarlane (2000, hereafter SM00), which accounts for unresolved orography through three processes: vertical fluxes of momentum from topographically forced freely propagating gravity waves; drag enhancement due to low-level wave breaking (i.e. downslope windstorm behaviour); and, finally, low-level flow blocking. Transitions between these processes are discerned through the inverse Froude number, a nondimensional measure of the nonlinearity of the topographic forcing, given by $Fr = Nh/U$, where h is the sub-grid mountain height and N and U are bulk measures of the buoyancy frequency and wind speed upstream of the sub-grid topography. It should be noted that while the treatments of each of these three processes are distinct, there is considerable overlap of the Fr values over which they are operable (SM00). Idealised modelling studies and observational campaigns have provided an approximate characterisation of the response to orographic forcing under different Fr forcing regimes. In regions where the flow is blocked ($Fr \geq Fr_{crit}$, with $Fr_{crit} = 1$) the drag over the height of the blocked layer is parameterized in the form:

$$D(z) \propto -\frac{\sigma_x}{\sigma}\rho_0 C_d U|U|$$

where σ_x is the slope of the sub-grid orography, σ is the standard deviation of the sub-grid orography, ρ_0 is the low-level density, C_d is the drag coefficient and U is the low-level wind. C_d is a free parameter and takes on different values for the 2-

Table 6.1: Description of perturbed parameterized orographic drag experiments. Columns are, from left to right: name of experiment; value of 2D and 3D blocking coefficient used; whether or not experiment has downslope wind drag turned on; and length of experiment at both 1xCO2 and 2xCO2.

Experiment	Blocking Coefficient CD = (2D,3D)	Downslope Wind?	Length
$[0, 0]$	CD = (0,0)	N	60yrs
$[B, 0]$	CD = (1.0,0.5)	N	60yrs
$[0, D]$	CD = (0,0)	Y	80yrs
$[B, D]$	CD = (1.0,0.5)	Y	80yrs
$[B+, 0]$	CD = (7.0,2.0)	N	60yrs
$[B+, D]$	CD = (7.0,2.0)	Y	80yrs

dimensional and 3-dimensional properties of the sub-grid orography (see SM00 for exact formulation).

In this study we focus primarily on the impact of low-level flow blocking on the circulation response by systematically varying the C_d parameter within the blocking component of the orographic drag scheme. The C_d values used in our experiments are within the range of what is found from laboratory experiments (Vosper, 2000) and is used in other models. The sensitivity of its impact to the presence of low-level wavebreaking is evaluated by switching the downslope drag enhancement on and off in the SM00 scheme. This leads to the set of 6 model configurations listed in Table 1, which were executed at both $1 \times CO2$ and $2 \times CO2$. Taken together, the set of 6 SM00 configurations may additionally be viewed as systematically increasing the total low-level drag and they have been ordered in Table 1 to reflect increasing drag moving down the table. While systematic, this increase in drag is not completely linear over all regions due to compensation by other surface drag processes, such as the boundary layer drag, and the Froude number dependence of the parameterized components. For reference, the configuration labelled [B,D] in Table 1 is the default setting of the SM00 scheme in CanESM4.1.

Delineating the sensitivity of the atmospheric circulation to the different configurations in Table 1 can be difficult due to internal variability of the climate system. This is particularly the case for processes that have an impact over regions with large variability, such as the impact that parameterized orographic drag has on storm tracks (Pithan et al., 2016). This motivated the use of cyclostationary $1 \times CO2$ preindus-

trial and $2 \times CO2$ perturbed AGCM-only simulations that could be executed for a period of time deemed necessary to separate such circulation sensitivities from the internal variability of the climate system. The length of integrations employed for each configuration in this study are also listed in Table 1.

6.2.2 Momentum budget calculation

The zonal mean vertically integrated momentum budget of the atmosphere on pressure levels is given by:

$$\frac{\partial}{\partial t}\left\langle [u] \right\rangle = -\frac{1}{a\cos^2\phi}\frac{\partial}{\partial \phi}\left\langle [uv] \right\rangle \cos^2\phi - \left[\frac{p_s}{a\cos\phi}\frac{\partial h_s}{\partial \lambda}\right] + \left\langle [fv] \right\rangle + \left\langle [F_\lambda] \right\rangle \tag{6.1}$$

where u and v are the zonal and meridional winds, respectively, a is the radius of the Earth, ϕ is latitude, p_s is the surface pressure, h_s is the surface elevation, λ is longitude, f is the Coriolis parameter and F_λ is the tendency from parameterized processes. In (6.1) $\left[(..)\right]$ indicates a zonal mean and $\left\langle (..) \right\rangle = \int_{p_{top}}^{p_s} (..) dp/g$ is the vertical integral from the surface to the model top. In CanAM4.1 F_λ has contributions from boundary layer turbulent mixing and parameterized orographic drag as well as negligible contributions from convective entrainment of momentum and horizontal diffusion. Momentum budget terms are calculated from 6 hourly output on model levels and spatial derivatives are calculated in spectral space, so as to be consistent with model numerics.

The time mean momentum flux convergence (MFC), the first term on the right hand side of (6.1), can be broken down into transient and stationary components:

$$\frac{1}{a\cos^2\phi}\frac{\partial}{\partial \phi}\left\langle [\overline{uv}] \right\rangle \cos^2\phi = \frac{1}{a\cos^2\phi}\frac{\partial}{\partial \phi}\left\langle \left[\overline{u'v'}\right] \right\rangle \cos^2\phi + \frac{1}{a\cos^2\phi}\frac{\partial}{\partial \phi}\left\langle [\overline{u}\,\overline{v}] \right\rangle \cos^2\phi \tag{6.2}$$

where overbars indicate a time mean and primes indicate a departure from the time mean. The stationary component can be further broken down into its zonal and eddy components, such that:

$$\frac{1}{a\cos^2\phi}\frac{\partial}{\partial\phi}\left\langle[\overline{u}\,\overline{v}]\right\rangle\cos^2\phi = \frac{1}{a\cos^2\phi}\frac{\partial}{\partial\phi}\left\langle[\overline{u}^*\overline{v}^*]\right\rangle\cos^2\phi + \frac{1}{a\cos^2\phi}\frac{\partial}{\partial\phi}\left\langle[\overline{u}]\,[\overline{v}]\right\rangle\cos^2\phi \tag{6.3}$$

where an asterisk denotes a deviation from the zonal mean. The first term on the right hand side of (6.3) is the stationary eddy momentum flux convergence (SEMFC) and the second term is the stationary zonal momentum flux convergence. While we do not calculate the contribution from the transient component explicitly, the stationary component is derived from climatological DJF mean values of u and v on pressure levels.

The motivation for looking at the momentum budget comes from the fact that the interaction between the surface drag and the momentum fluxes is two-way, such that, in the steady state limit, the predominant balance is between the momentum flux convergence and the surface drag. Understanding the extent to which low-level orographic drag plays a role in the structure of the circulation is, therefore, best aided by looking at how the momentum fluxes, and their stationary and transient contributions, are balanced or affected by surface drag.

6.2.3 Jet latitude calculation

The jet latitude is calculated using:

$$\phi_{max} = \frac{\sum_{\phi([u]\geq 0)}^{\phi_{pole}}\left[u(\phi)\right]^2\phi}{\sum_{\phi([u]\geq 0)}^{\phi_{pole}}\left[u(\phi)\right]^2} \tag{6.4}$$

where $[u]$ is the zonal wind averaged over some sector, $\phi([u] \geq 0)$ is the latitude at which the zonal winds over that sector become positive and ϕ_{pole} is the most poleward latitude considered, set as 75N over the NH and 75S over the SH.

Relative to the usual latitude of the jet maximum that is often quoted in the literature, ϕ_{max} provides a bulk measure of the structure of the jet and its response since it integrates over the entire jet structure and so is able to account for regions in which there may be a bimodal distributions or a tilt in the jet, as is found over the North Atlantic (NA) (Woollings et al., 2010). The sectors discussed in what follows

are defined as the average zonal winds over: the NH 0E-360W, 15N-75N; NA sector 30W-30E, 15N-75N; NP sector 150E-240E, 15N-75N; and SH 0E-360W, 15S-75S. The NP and NA sectors are chosen to correspond with the regions of the largest changes seen in response to increasing the parameterized orographic drag.

6.2.4 Regression analysis

It is understood from theoretical, observational and modelling studies that the amplitude, phase and location of low-frequency waves are strongly related to the modes of jet variability within the atmosphere (Rossby, 1939; Wallace and Hsu, 1985; Ting et al., 1996), with anomalous stationary wave momentum fluxes over the NA being associated with a more poleward tilted NA jet, relative to its climatology (Limpasuvan and Hartmann, 2000; DeWeaver and Nigam, 2000). The internal variability of the atmosphere can therefore be exploited to understand the relationship between the stationary wave forcing on the mean flow, its location and amplitude, and the jet latitude. We use regression analysis over different sectors of the NH to capture the spatial structure of the low-frequency wave forcing under different jet latitude regimes. To do this, we first generate a jet latitude index as a function of time by normalising the monthly jet latitude anomalies by the maximum anomaly:

$$\alpha(m) = \frac{\phi_{max}(m) - \overline{\phi}_{max}}{max(|\phi_{max}(m) - \overline{\phi}_{max}|)} \tag{6.5}$$

where $\phi_{max}(m)$ is calculated from the monthly mean zonal winds at 850hPa using (6.4) and $\overline{\phi}_{max}$ is the average of $\phi_{max}(m)$ over all months considered. Thus, $\alpha(m)$ is generated for each December, January and February between 1979 and 2016 from ERA interim monthly mean data.

Regressing the stationary Plumb flux vector $\mathbf{F_p}$ (see section 2.3.2), given by (5.7) in Plumb (1985), onto α gives:

$$\mathbf{R} = \overline{\alpha(m)\mathbf{F_p}(m)}. \tag{6.6}$$

α can be calculated for different sectors of the globe and gives an indication of the strength of the jet latitude anomaly. The time mean covariance between α and $\mathbf{F_p}$, given by $\mathbf{R}$, can be seen as the difference between the stationary Plumb flux at anoma-

lously high jet latitudes and anomalously low jet latitudes.

6.3 Response to orographic drag at 1xCO2

6.3.1 Zonal wind response to drag

We begin by looking at the circulation response to systematically increasing total parameterized orographic drag (i.e. [0,0] to [B+,D] in Table 1) at $1 \times CO2$. The primary behaviour of the response will be illustrated by focussing on the difference between the experiments [B+,D] and [0,0]. The spatial structure of the response to increased drag remains very similar across the configurations listed in Table 1 and, unless stated otherwise, the response amplitude increases as the low-level parameterized drag is increased. An example of the increasing amplitude of the response with increased drag is shown later in figure 6.6. This scaling of the response to drag, although not entirely linear, implies that the circulation response is robust and that configuration [B+,D] relative to [0,0] is representative of this sensitivity. Figure 6.1a shows the $1 \times CO2$ climatological momentum flux convergence, MFC, (divided by 10) for experiment [0,0] in black and the total parameterized orographic drag (freely propagating wave drag, blocking drag and downslope wind drag) acting on the zonal winds for experiment [B+,D] in grey. The change in the MFC in response to increasing the parameterized drag is plotted in solid blue. As is to be expected from the hemispheric distribution of land, the momentum flux response to increased orographic drag is larger in the NH than the SH. There is, however, large parameterized orographic drag located at ∼65S, which is the latitude encompassing the Antarctic Peninsula. Large low-level drag over this region may be explained by the fact that the cold Antarctic region, with strong stratification, will have more flow trapped near the surface.

The climatological zonal mean zonal wind at 850hPa for [0,0] is plotted in black in figure 6.1b, along with its response to increased drag in blue. The climatological surface winds and their response correspond well with the momentum fluxes and their response. There is an overall poleward migration of the circulation, as indicated by the jet latitude change quoted in blue. The values quoted in black are the climatological values in [0,0] and the values in brackets are the jet latitudes calculated from ERA interim reanalysis (Dee et al., 2011) using DJF climatology from December 1979 to January 2016. From these jet latitude values, it can be concluded that the [0,0] experiment has jets placed

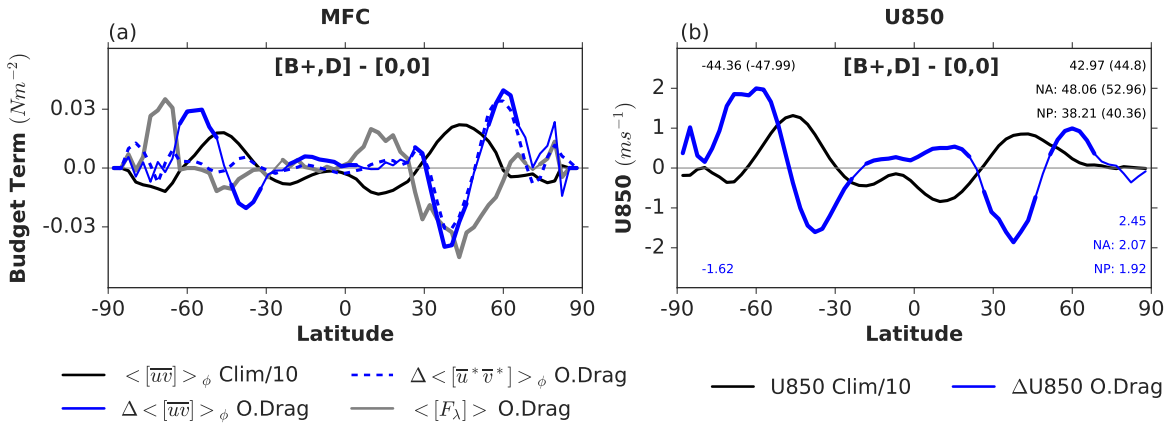

Figure 6.1: (a) DJF 1xCO2 MFC climatology divided by 10 (solid black line) and response to parameterized orographic drag (solid blue line). Solid grey line: zonal mean total (freely propagating, blocking and downslope wind) parameterized orographic stress at 1xCO2. Dashed blue line: SEMFC response to drag. (b) DJF 1xCO2 u 850hPa climatology (solid black line) and response to drag (solid blue line). See text for description of values quoted in (b). Regions of statistically significant differences (at the 95% level based on a two sided independent student's t-test) are indicated by a thickening of the line.

preferentially towards the equator in all sectors considered, relative to ERA interim. Across the experiments, the additional orographic drag shifts the jet towards the pole in all sectors with the magnitude of the shift increasing with increasing low-level drag. This acts to mitigate the jet biases, roughly cutting it in half in the SH and NA, and essentially eliminating it in the NH and NP. For comparison, Bracegirdle et al. (2013) showed that the SH zonal mean jet latitude bias could be reduced by 28% when observed SSTs and sea-ice are prescribed in place of coupling between the ocean/ice and atmosphere models. Here, the SH zonal mean jet latitude bias is reduced by 44% when the low-level parameterized orographic drag is included, further demonstrating the large role of atmospheric processes in the SH jet latitude bias.

Although the deceleration felt by the atmosphere from the additional parameterized drag acts only near the surface, the response may not necessarily be confined to the lower part of the atmosphere. A similar poleward migration of the circulation within the troposphere can be seen in figure 6.2, which shows the 1xCO2 climatological zonal mean zonal winds for [0,0] in figure 6.2a and their response to increased drag in figure 6.2b as a function of pressure. The response to the increased drag is vertically coherent

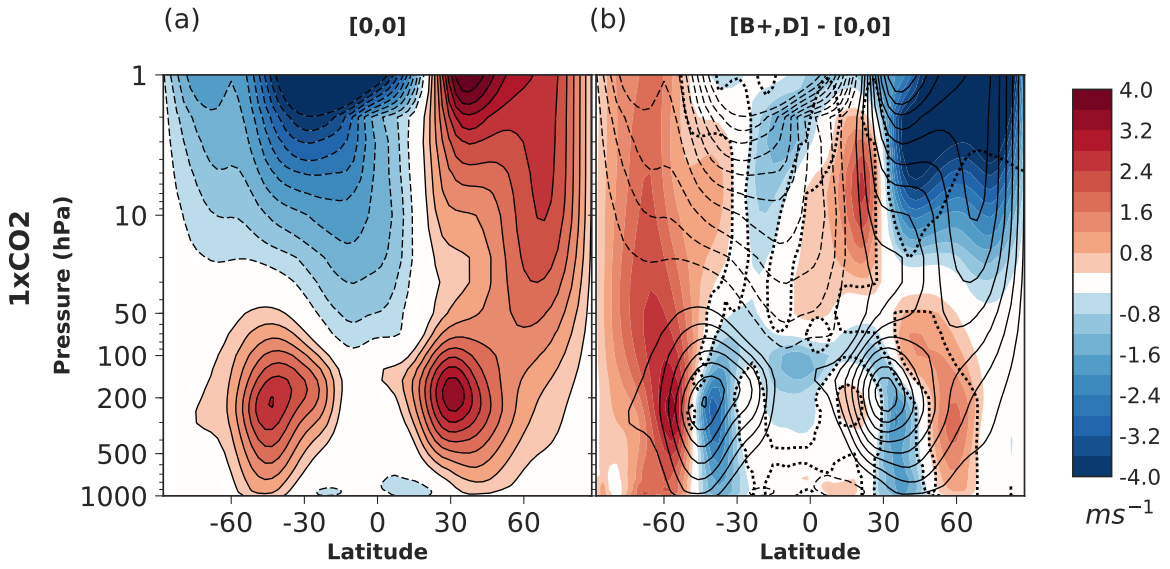

Figure 6.2: DJF $[u]$. (a) [0,0] $1 \times CO2$ climatology, contour interval is $5ms^{-1}$. (b) Line contours indicate [0,0] climatology and coloured contours are the response to drag ([B+,D] minus [0,0]) with contour interval given by colorbar. Regions of statistically significant differences (at the 95% level based on a two sided independent student's t-test), are encompassed by dotted black lines, as is also the case in figures to follow.

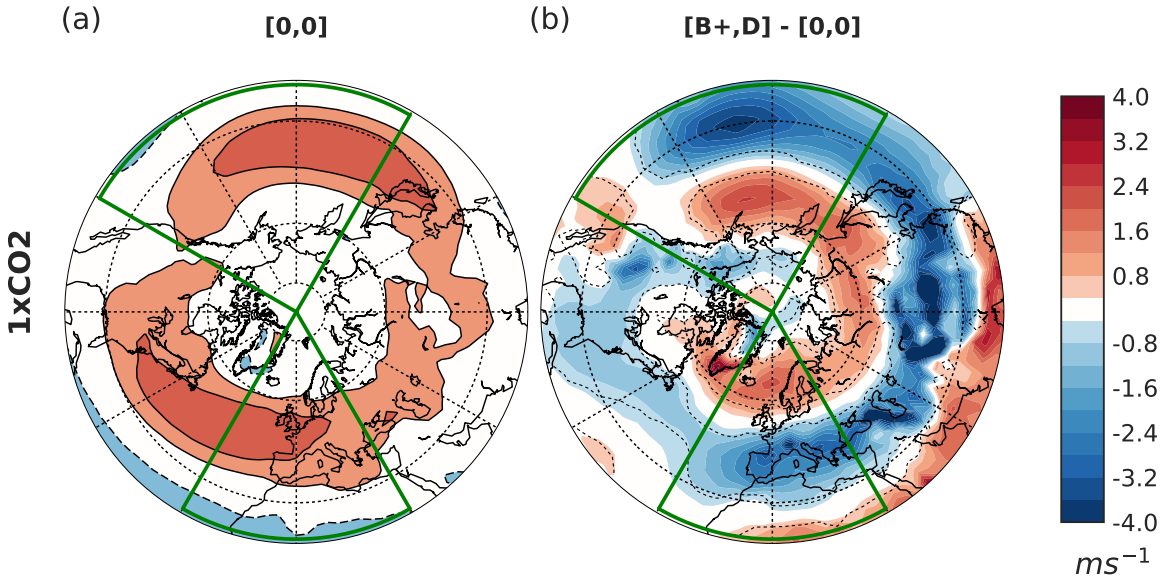

Figure 6.3: DJF u 850hPa. (a) $1 \times CO2$ climatology in [0,0], contour interval is $5ms^{-1}$. (b) Response to drag, with contour interval given by colorbar.

within the mid-latitude troposphere. The date of the transition to easterlies in the SH stratosphere has been shown to be hastened by an increase in the freely propagating wave component of the parameterized orographic drag (McLandress et al., 2012), the magnitude of which is reduced as the low-level drag is increased (not shown). This may explain why, in the SH, the response extends far up through the atmosphere and appears as a deceleration of the easterlies in the SH polar stratosphere.

In contrast to the SH, the NH polar stratospheric winds decelerate with increasing low-level blocking drag, with only [B,D] exhibiting an acceleration of the polar stratosphere (not shown). There is, however, a lack of statistical significance over this region in [B,D] which suggests that this may be due to the large variability that is seen in the stratosphere during the NH winter season as a result of sudden stratospheric warmings. The deceleration of the stratospheric winds in response to increased low-level drag is similar to that found by Sandu et al. (2016), in experiments where the parameterized low-level orographic blocking was increased. This, as well as the four experiments that show a deceleration within the stratosphere, supports the idea that there is an increase in the wave forcing reaching the NH polar stratosphere when low-level drag is increased.

The longitudinal structure of the 850hPa zonal wind response to drag is shown

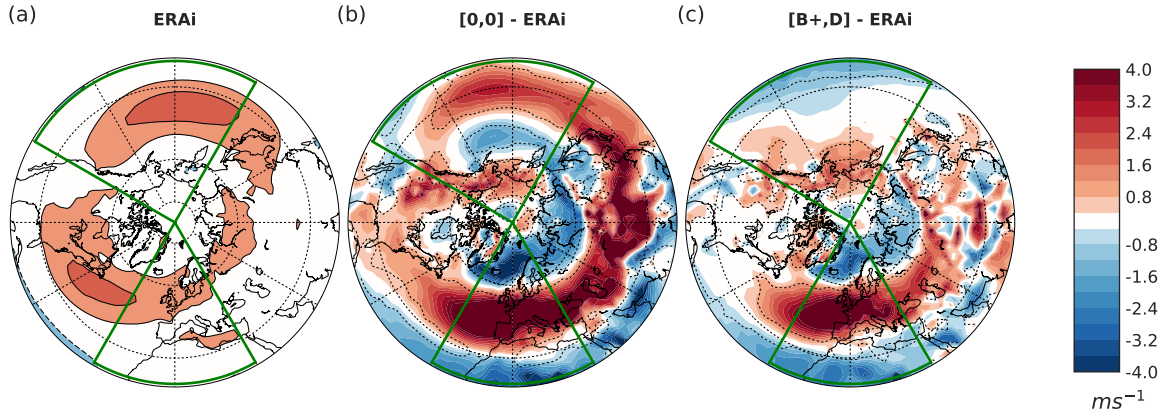

Figure 6.4: DJF u 850hPa. (a) ERA interim climatology, contour interval is $5ms^{-1}$. (b) [0,0] minus ERA interim. (c) [B+,D] minus ERA interim. Contour interval in difference plots given by colorbar.

in figure 6.3 with, as before, the climatological values in [0,0] in figure 6.3a and the response to increased drag in figure 6.3b. The largest changes occur at the jet exit regions over the NA and NP. As a point of reference, the ERA interim DJF climatological 850hPa zonal winds are plotted in figure 6.4a. There are clear differences that can be seen by eye between the ERA interim climatology and the [0,0] climatology: in the latter the NP jet is too strong at the jet exit and entrance regions and the NA jet is too strong and zonal over western Europe. This is evidenced by the difference plotted in figure 6.4b. It is striking that the differences between the [0,0] and ERA interim zonal winds match the structure of the response to increased drag, but with an opposite sign. It is, therefore, not surprising that the differences are much smaller between ERA interim and [B+,D], the experiment with the largest amount of low-level drag (figure 6.4c). This shows that, for the diagnostics considered here, the additional low-level drag is beneficial for the model fidelity of CanAM4.1.

It is clear from what has been discussed that the additional orographic drag has a non-negligible impact on the zonal winds. In order to ascertain the mechanisms behind this sensitivity we appeal again to the momentum budget calculations. As is found in both observations and models (Limpasuvan and Hartmann, 2000; Simpson et al., 2014), the stationary eddies make a dominant contribution to the climatological momentum transport in the NH, whereas the transients account almost entirely for the momentum transport in the SH. A comparison of the total MFC and SEMFC response to increased drag, plotted in a dashed blue line in figure 6.1a, shows that the change in the zonal

wind over the NH is also predominantly due to a change in the transport of momentum by the stationary eddies. In contrast, the zonal wind change in the SH is sustained by a change in the transient momentum flux convergence. While we recognise that the SH response to increased drag is important, the mechanisms are apparently more complex and so beyond the scope of the present study. Analysis of the SH response will, therefore, be left for future investigation. That said, the SH response is similar to the response to orographic blocking found by Pithan et al. (2016) using the MetUM, and is consistent with the mechanism proposed in Chen and Zurita-Gotor (2008). They find that prescribing a positive zonal torque at the surface on the poleward flank of the jet maximum leads to a poleward shift of the mid-latitude jet. The opposite is found for a torque placed on the equatorward flank of the jet maximum. In our experiments the additional orographic drag leads to both a positive torque on the poleward flank and a negative torque on the equatorward flank of the SH jet, which would be expected to result in in a poleward shift by the arguments of Chen and Zurita-Gotor (2008).

6.3.2 Stationary wave response to drag

Since we know that it is the transport of momentum by the stationary eddies that sustains the zonal wind response to increased orographic drag in the NH, it is of interest to consider how the stationary wave field itself changes with increased drag. The zonally asymmetric meridional winds (v^*) at 300hPa are used to visualise the stationary wave field. Climatological v^* at 300hPa is plotted in figure 6.5a for [0,0] and the response to drag in figure 6.5b. From the climatology, there is evidence of a wave train emanating from the Himalayan topography that reaches the North American coast where the flow is altered by the presence of the Rockies, acting to elongate the waves and aiding the characteristic jet tilt that is seen over the North Atlantic. As the parameterized drag is increased, the wave train over the Pacific is strongly damped, whereas the stationary waves over the higher-latitude NA are amplified.

To visualise this, the zonal wavenumber spectrum of v^* at 300hPa is plotted as a function of latitude for [0,0] on the far left of figure 6.6 and the response to drag across the experiments is plotted to its right. As was indicated by figure 6.5, the waves in the midlatitudes (predominantly over the Central Pacific), which peak at zonal wavenumber 5, are systematically damped by the additional drag. At the high latitudes v^* at wavenumber 2 is amplified.

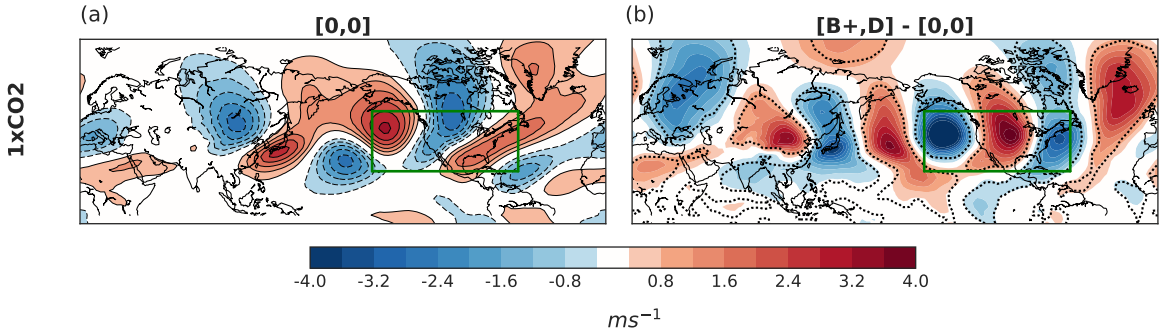

Figure 6.5: DJF v^* 300hPa. (a) [0,0] $1 \times CO2$ climatology, contour interval is $2ms^{-1}$. (b) Response to drag, with contour interval given by colorbar.

The localised change in the stationary wave forcing is illustrated by figure 6.7, which shows the 1xCO2 [0,0] climatology (figure 6.7a) and response to drag (figure 6.7b) of the 700hPa vertical (coloured contours) and 300hPa horizontal (vectors) components of the stationary Plumb flux. The zonal mean of the Plumb flux is equivalent to the EP flux for stationary waves. In regions where the vertical component is large there is an acceleration of the surface westerlies, and in regions where the vectors are diverging meridionally there is an acceleration of the westerlies at 300hPa. As the low-level parameterized drag is increased, there is a large reduction in the vertical and meridional component downwind of the Himalayas and an increase over Siberia, which is consistent with a poleward movement of the NP zonal winds. Over the Rockies there is a decrease in the vertical component, which acts to reduce the surface westerlies. As is anticipated from the increased v^* amplitudes, there is an increase in the vertical and meridional components of the Plumb flux over the NA which results in an increased forcing of the stationary waves and the zonal wind. This not only shows the longitudinal structure of the wave forcing but also demonstrates that the changes in the stationary waves are situated around the largest orography. This diagnostic aids the interpretation that damping of the waves in the mid-latitudes over the NP, which leads to reduced zonal momentum and heat fluxes into that region by the stationary eddies, are a result of changes in the stationary waves originating from the topography, particularly the Himalayas.

The source of the stationary wave changes over the NA is less clear and it is possible that the amplified stationary waves over the NA are a result of changes in the stationary waves originating from either the Rockies or Greenland (Junge et al., 2005). For the

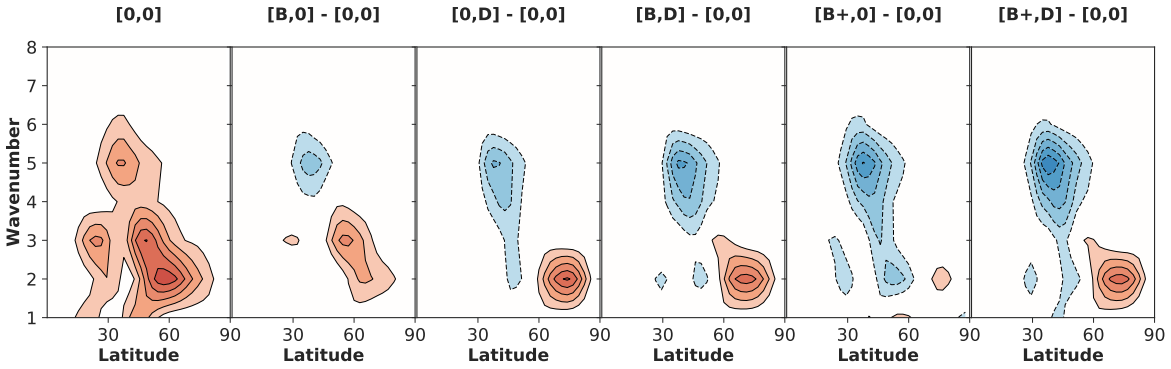

Figure 6.6: DJF v^* 300hPa wavenumber versus latitude spectrum. Far left: [0,0] $1 \times CO2$ climatology, contour interval is $5m^2s^{-2}$. Right: response to drag across the experiments (experiment minus [0,0]). Contour interval is $2m^2s^{-2}$ in difference plots.

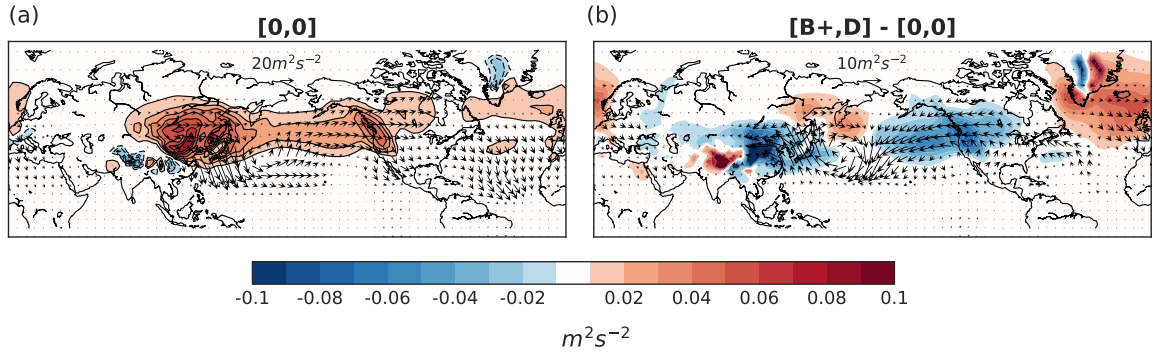

Figure 6.7: DJF stationary Plumb flux. Coloured contours are the vertical component at 700hPa, contour interval is $4 \times 10^{-2}m^2s^{-2}$, and arrows are the horizontal component at 300hPa, with their magnitude indicated by the key. (a) [0,0] 1xCO2 climatological Plumb flux. (b) Response to orographic drag ([B+,D] minus [0,0]), with contour interval given by colorbar and arrow magnitude given by key.

case in which changes in the stationary waves seen over the NA originate from the Rockies (although similar arguments may be be applied to Greenland), there are two possible mechanisms for this response. In the first, the parameterized orographic drag acting over the Rockies directly alter the stationary wave generation over that region. In the second, the zonal wind changes occurring over the Pacific region, that are the results of changes in the parameterized orographic drag over the Himalayas, alter the way in which the winds interact with the resolved Rocky mountains, thus altering the downstream wave generation.

6.3.3 Connection between jet latitude and stationary waves

In section 6.26.2.4, we described a regression analysis which utilises the fact that the low frequency variability of the NA and NP jet latitude is related to the momentum and heat fluxes by the stationary waves. This regression analysis is not capable of attributing cause and effect since it is only capturing the instantaneous covariance of the two fields. It is also possible that externally forced variations in jet latitude and stationary wave amplitude, such as those imposed by the stratosphere or diabatic heating, can have an impact on the relationship between these two fields. Nevertheless, if we wish to understand the contribution that the stationary waves make towards sustaining the jets at particular latitudes, we find this analysis a useful means to this end.

Figure 6.8 shows the normalised jet latitude anomalies for the NA and NP for the NH winter season (DJF) as a function of time (in months) calculated from ERA interim zonal winds at 850hPa. There is clearly a lot of inter-annual variability in jet latitude over the NA and NP, with the anomalies of the NA possibly appearing more persistent compared with those over the NP. Figure 6.9 shows the regression of α calculated over the NA and NP sectors, as shown in figure 6.8, on the stationary Plumb flux ($\mathbf{F_p}$) given by (6.6). Looking first at the NA R field, the Plumb flux over the NA region that is associated with a more poleward NA jet tilt is that of increased vertical surface heat fluxes and upper level meridional momentum fluxes over the NA. This is in contrast to the stationary wave field that is associated with a more poleward NP jet, which appears as a weakening of the vertical component of the Plumb flux over the west coast of North America and downwind of the Himalayas.

The analysis above suggests that a stronger climatological stationary wave pattern

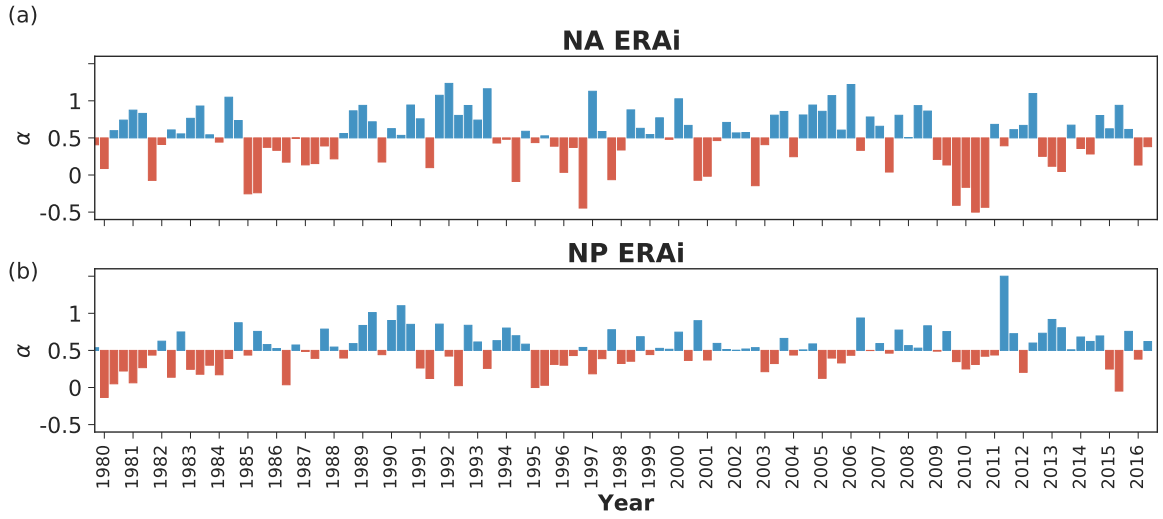

Figure 6.8: Time series of α (see section 6.2.4) calculated from monthly u 850hPa values during DJF season for ERA interim starting in December 1979 over (a) NA and (b) NP sectors given by green boxes in figure 6.3.

over the NA is associated with a more poleward tilted NA jet and that a damping of the stationary waves over the NP is associated with a more poleward positioned NP jet. Indeed, comparing figure 6.9 with the Plumb flux response to increased drag shown in figure 6.7, we see that the anomalous stationary wave fields that emerge from internal variability associated with more poleward jet latitudes are similar to the stationary wave response to increased orographic drag. From this, as well as findings by DeWeaver and Nigam (2000) and Ting et al. (1996), we may conclude that the stationary waves play an important role in sustaining regional jet latitude and, on altering the climatological stationary waves, an associated change in the climatological jet latitudes is likely to be seen.

Figure 6.10 shows the relationship between the RMS v^* amplitude over the region 45W-45E, 30N-90N and the jet latitude over the NA at 1xCO2 in the set of experiments and ERA interim. As is consistent with the regression analysis and the spectra shown in figure 6.6, the experiments with larger amounts of orographic drag, which tend to have larger stationary wave amplitudes over the NA, also tend to have a more poleward tilted NA jet. What is more, the large stationary wave amplitudes in ERA interim also correspond well with a more poleward tilted NA jet.

Figure 6.11 shows the climatological power spectrum of v^* as a function of wavenumber and latitude for ERA interim, [0,0] and [B+,D]. The peak between 30N-40N at

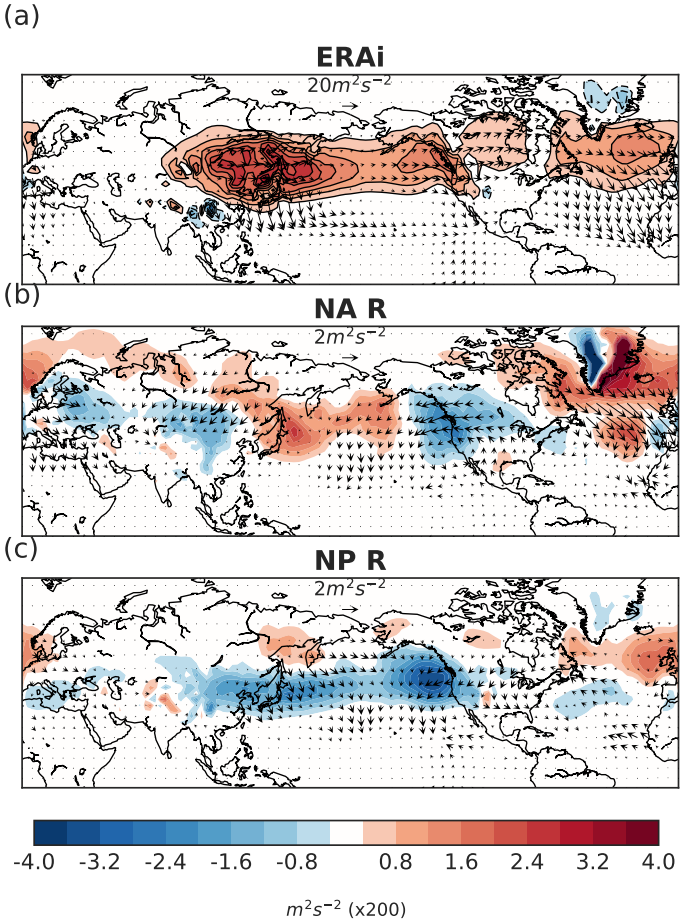

Figure 6.9: (a) DJF stationary Plumb flux calculated for ERA interim. Coloured contours are the vertical component at 700hPa, contour interval is $4 \times 10^{-2} m^2 s^{-2}$, and arrows are the horizontal component at 300hPa, with their magnitude indicated by the key. R (see (6.6)) for ERA interim over DJF season calculated for (b) the NA sector and (c) the NP sector. Coloured contours are the vertical component at 700hPa, contour interval given by colorbar (x200), and arrows are the horizontal component at 300hPa, with their magnitude indicated by the key.

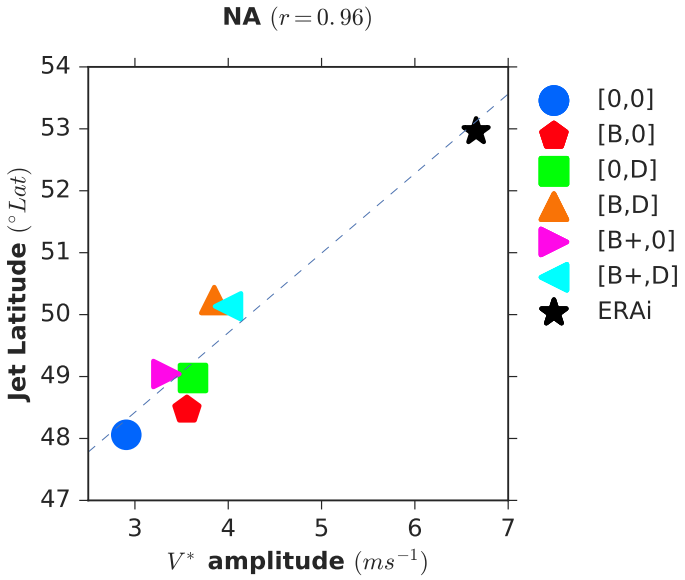

Figure 6.10: Relationship between RMS v^* 300hPa amplitude over the NA and the NA jet latitude for the drag experiments at 1xCO2 and ERA interim (ERAi).

wavenumber 5 in [0,0] is not at all present in the reanalysis and when the low-level drag is increased this peak is barely visible. The increase in wavenumber 2 amplitudes over the northern high latitudes also brings [B+,D] closer to the ERA interim climatology. Figure 4c of Simpson et al. (2015), which shows the CMIP5 multi-model mean climatological v^* spectrum, is similar to that of [0,0] with weak wavenumber 2 amplitudes at high latitudes, relative to ERA interim, and a peak at wavenumber 5. The discussion above, along with the v^* spectrum presented in Simpson et al. (2015), suggests that the too zonal NA jet and equatorward NP jet biases that are prevalent in climate models are connected with the too weak stationary waves over the NA and too strong stationary waves over the NP. A similar conclusion was drawn by Pithan et al. (2016), who found that increased parameterized orographic drag led to an improved representation of the North Atlantic jet tilt and, as a result, an improved storm track density over that region.

6.4 Climate change response

We have shown that there are large changes in the climatological circulation, primarily in the stationary wave field, when the low-level parameterized orographic drag is

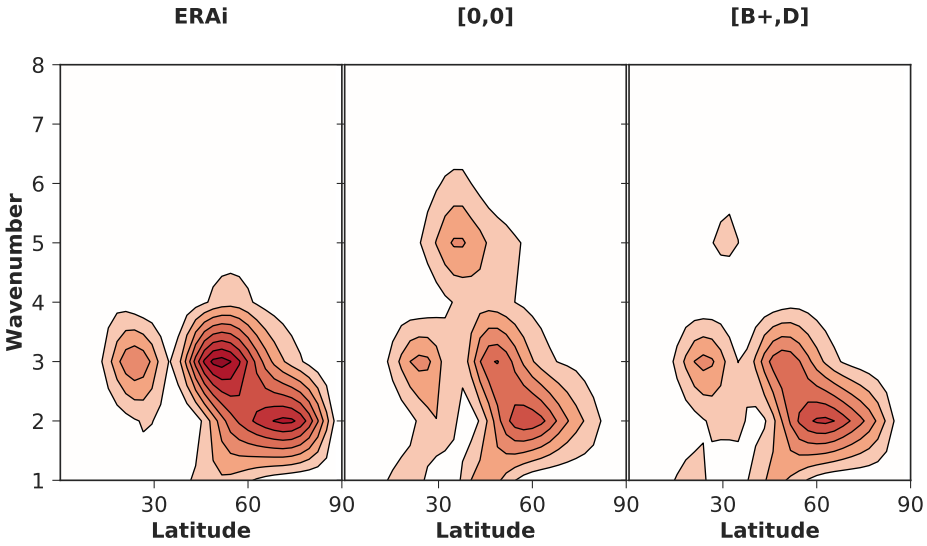

Figure 6.11: DJF climatological v^* at 300hPa zonal wavenumber versus latitude spectrum for, from left to right, ERA interim, [0,0] and [B+,D]. Contour interval is $5m^2s^{-2}$.

systematically altered across our experiments (i.e. Table 1). Since the configurations described in table 6.1 are forced with the same SSTs and sea-ice, it is easier to disentangle the often alluded to but difficult to quantify connection between the climatological basic state of the model and its response to climate change. With this in mind, the following analysis addresses this issue in the context of climatological stationary waves and their response to climate change.

6.4.1 Stationary wave response to climate change

Simpson et al. (2015) showed that the amplitude of the stationary wave response over the South West interior of North America in the CMIP5 ensemble was dependent not only on the historical stationary wave amplitudes but also on the zonal mean zonal wind response to climate change. As a result, we begin the discussion by looking at the latter. Figure 6.12a shows the zonal mean zonal wind response to climate change in [0,0]. The difference between the response to climate change in [B+,D] and the response in [0,0] is shown in coloured contours in figure 6.12b, with the full response in [0,0] repeated in line contours. We note the typical features of the zonal wind response to climate change that are robust across models, such as the poleward movement of the SH jet and the strengthening of the winds in the subtropics that result

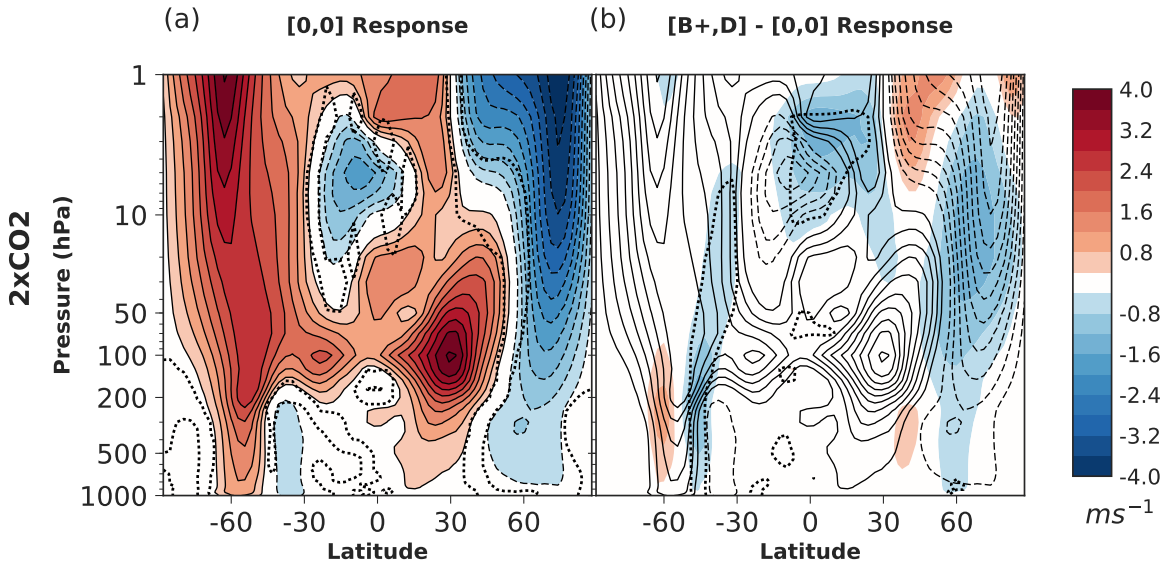

Figure 6.12: DJF $[u]$ response to climate change. (a) Response to climate change in [0,0], contour interval is $0.8ms^{-1}$. (b) Response to climate change in [B+,D] minus the response to climate change in [0,0], with contour interval given by colorbar.

from sub-tropical upper tropospheric amplification of surface warming (e.g. Butler et al. 2010). There is, however, a lot of uncertainty in the Northern Hemisphere high-latitude tropospheric and stratospheric circulation response in climate models, which is often linked to the interplay between the strength of the Arctic and sub-tropical upper tropospheric amplification (Manzini et al., 2014). Although the CMIP5 multi-model mean NH mid-latitude jet response is a poleward shift in DJF (Barnes and Polvani, 2013), there is a lot of spread about this mean and the zonal wind response seen in these experiments is just one possible outcome under climate change. Relative to the CMIP5 ensemble, these experiments have an average amount of polar amplification, a deceleration of the stratospheric winds and a weak sub-tropical amplification, which is consistent with an equatorward shift of the NH zonal winds (Zappa and Shepherd, 2017).

What is clear from the difference in the climate change response (figure 6.12b) is that the additional low-level parameterized orographic drag has no significant impact on the strengthening of the subtropical zonal mean zonal winds, which Simpson et al. (2015) found to be the main driver of the stationary wave response to climate change. This is also true across our model configurations (not shown). Following the reasoning of Simpson et al. (2015), this implies that any significant differences seen in the stationary

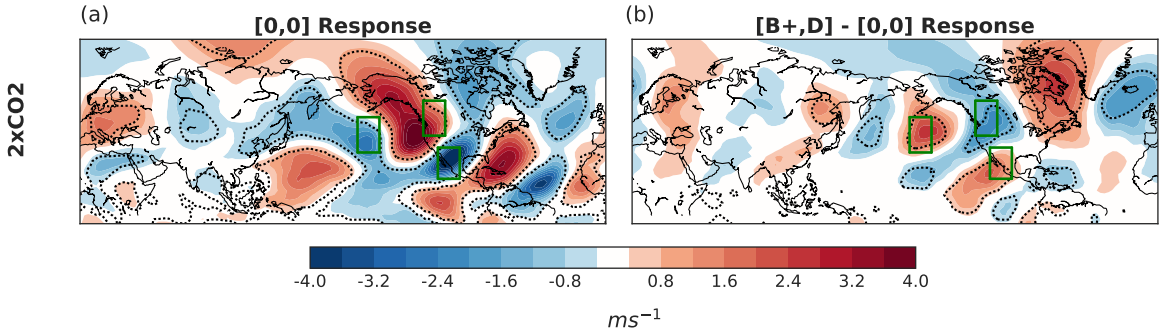

Figure 6.13: DJF v^* 300hPa response to climate change. (a) Response to climate change in [0,0]. (b) Response to climate change in [B+,D] minus the response to climate change in [0,0]. Contour interval given by colorbar.

wave response to climate change over the NH are predominantly due to the differences in the 1xCO2 basic state.

Figure 6.13a shows the v^* at 300hPa response to climate change in [0,0]. It is quantitatively similar over North America to the CMIP5 model mean shown in Simpson et al. (2015). The differences in the response between [B+,D] and [0,0] are plotted in figure 6.13b. As with the response to increased drag in the 1xCO2 climatology, the impact of the additional parameterized orographic drag on the response to increased CO_2 scales with the amount of parameterized drag. This is demonstrated in figure 6.14 which shows the relationship between the root mean square (RMS) amplitude over the region indicated by the green box in figure 6.5 and, from left to right, the region over the Pacific (PC), the west coast of North America (WC) and the south west interior of North America (SW), which are indicated by the green boxes in figure 6.13. There is a strong relationship between the climatological stationary wave amplitudes and their response to increased CO_2. There is some spread around this relationship, however, and the position of the experiments along the linear fit vary somewhat, perhaps due to the discrete nature of the bounding box. These plots are illustrative and should be interpreted as such. In general, the experiments with the least amount of drag ([0,0] and [B,0]) have stronger historical stationary wave amplitudes over the Pacific and North America and exhibit stronger v^* responses. The experiments with the largest amount of drag ([B+,0] and [B+,D]) have the weakest stationary waves over this region and have the weakest v^* responses.

Although the parameterized low-level drag acts to damp the stationary waves over

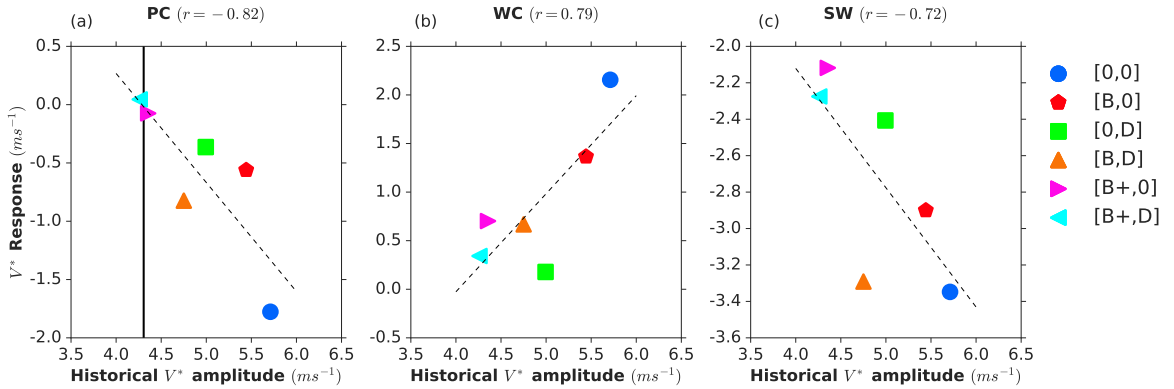

Figure 6.14: Relationship between the DJF 1xCO2 climatological stationary wave amplitudes and their response to climate change. The RMS v^* 300hPa amplitude over 160W-60W, 20N-45N versus the v^* response over (a) PC, (b) WC and (c) SW. PC, SW and WC areas are indicated by green boxes in figure 6.13. r values are the correlation coefficients. Vertical line indicates ERA interim DJF climatological value.

the Pacific and North America, it acts to amplify them over the NA. One might then wonder whether the relationship described above holds for this region. Figure 6.15 shows the relationship between the RMS v^* amplitude over the region 45W-45E, 30N-90N versus the RMS amplitude of the response to increased CO_2 over the same sector. Once again the relationship is strong, with larger historical v^* amplitudes leading to a larger v^* response. However, as was shown in figure 6.10, the experiment [B+,0] does not have a large increase in its v^* amplitude over the NA, despite having a large amount of parameterized drag. This is likely due to the difference between the Froude number dependences and centres of action of the blocking and the downslope wind component.

The dependence of the stationary wave response to climate change on the 1xCO2 basic state is anticipated from linear stationary wave theory. Following the derivations of Nigam and DeWeaver (2002) from the quasi-geostrophic shallow water equations, the amplitude of the stationary wave streamfunction for some arbitrary zonal (k) and meridional (l) wavenumber is given by:

$$\hat{\psi} = \frac{f\hat{h}}{H[k^2 + l^2 - \frac{\beta}{[u]}]} \tag{6.7}$$

where $\beta = \partial f/\partial y$, H is the depth of the fluid and $\hat{h}$ is the amplitude of the mechanical forcing by orography. Equation (6.7) shows that the amplitude of the stationary wave

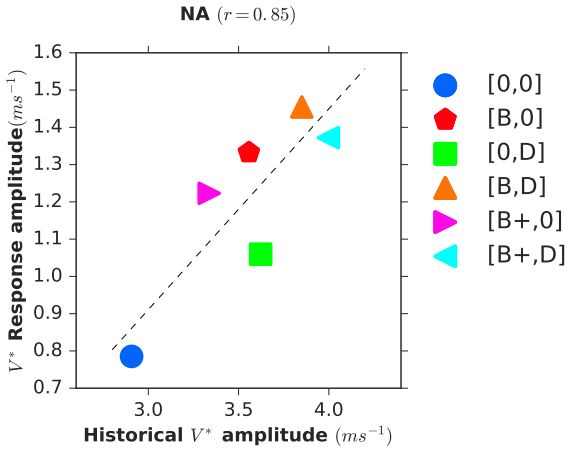

Figure 6.15: Relationship between the DJF 1xCO2 climatological stationary wave amplitude over the NA and its response to climate change. RMS v^* 300hPa amplitude calculated over 45W-45E, 30N-90N. r value is the correlation coefficient.

streamfunction depends linearly on the orographic forcing and, in a more complex way, on the zonal mean zonal wind. By varying the orographic forcing through the orographic drag parameterization we find that there is a variation in the stationary wave response to climate change. Linear stationary wave theory suggests that this variation could be a result of either a different zonal mean zonal wind response or the same zonal mean zonal wind response acting on a different orographic forcing. Since figure 6.12 shows that the former is not significant between the experiments, it must be the latter, in which case, the stationary wave response to climate change depends linearly on the orographic forcing.

6.4.2 Zonal wind response to climate change

The discussion presented in section 6.36.3.3 implies that the spread in the stationary wave response to climate change that results from varying the parameterized orographic drag may have an impact on the regional zonal wind response to climate change. Figure 6.16a shows the climatological MFC (solid black lines) and SEMFC (dashed black line) at 1xCO2 and their responses to climate change in red for experiments [0,0] and [B+,D]. The orographic drag in the 2xCO2 climatology is also shown in grey. The first thing to note is that the orographic drag does not differ discernibly between the 1xCO2 and 2xCO2 climatologies (compare with grey curve in figure 6.1), which implies that the

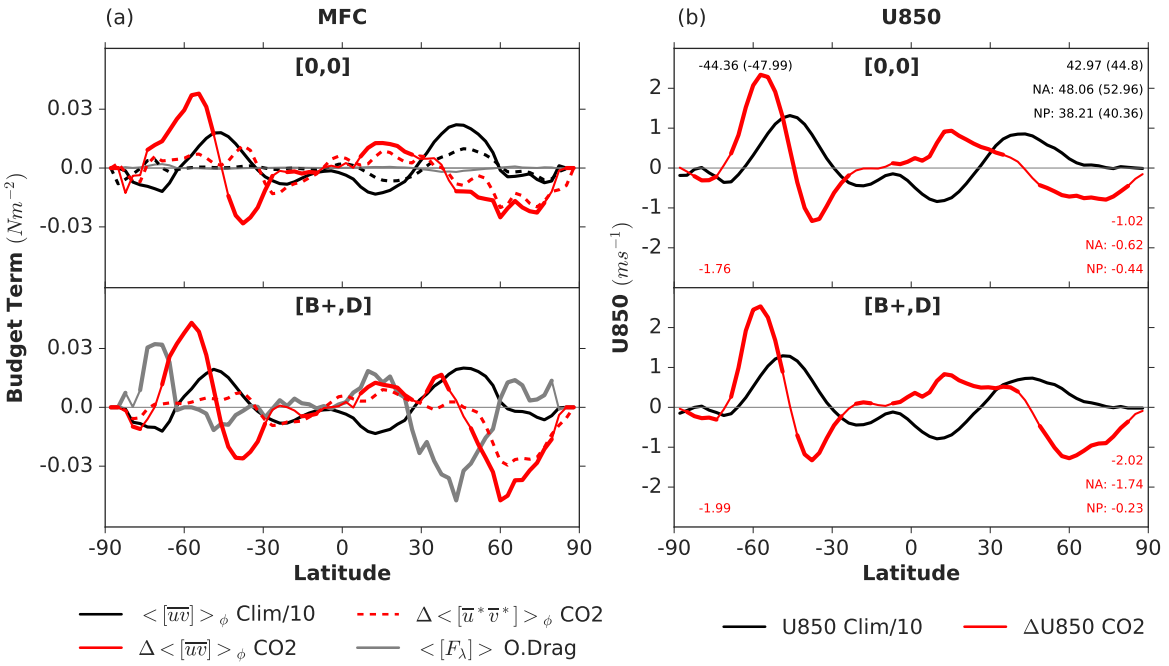

Figure 6.16: (a) DJF 1xCO2 MFC climatology divided by 10 (solid black lines) and response to climate change (solid red lines). Dashed black line: 1xCO2 climatological SEMFC in [0,0] divided by 10. Solid grey line: zonal mean total (freely propagating, blocking and downslope wind) parameterized orographic stress at 2xCO2. Dashed red lines: SEMFC response to climate change. (b) DJF 1xCO2 u 850hPa climatology (solid black lines) and response to climate change (solid red lines). Regions of statistically significant differences (at the 95% level based on a two sided independent student's t-test) are indicated by a thickening of the line.

influence of the orographic drag is limited to its impact on the 1xCO2 climatology and is not the direct cause of the differences in the response to CO_2 seen across the model configurations (see Sigmond and Scinocca (2010) for similar arguments made in regards to gravity wave drag influences on the stratospheric polar vortex response to climate change). The second is that the SEMFC (dashed red curves) dominates the response to climate change over the NH high latitudes, whereas the transient eddies dominate the response in the mid-latitudes and over the SH. Figure 6.16b demonstrates how the 850hPa zonal mean zonal wind response to climate change follows the MFC response.

Figure 6.17 shows the longitudinal structure of the 850hPa zonal wind response to climate change in [0,0] and the difference in the response as a result of increased parameterized drag. Since climate change acts to weaken the climatological stationary waves over the NA (figure 6.13), one would expect an equatorward shift of the NA

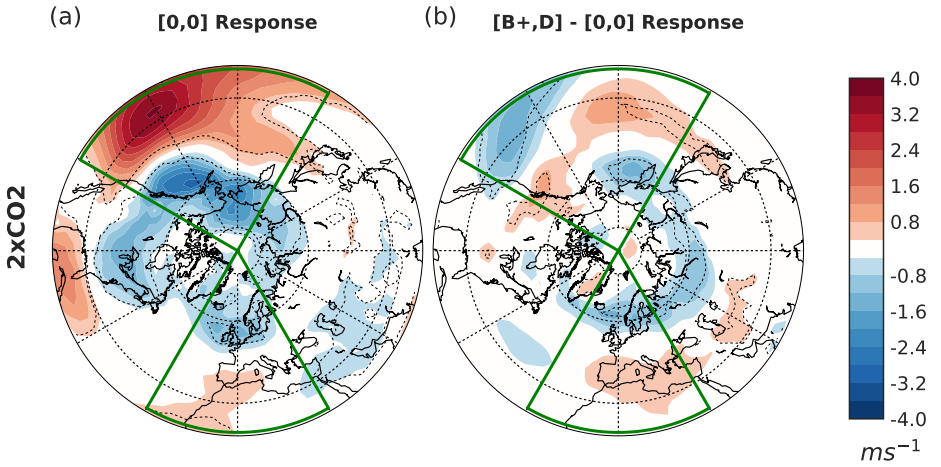

Figure 6.17: DJF u 850hPa response to climate change. (a) Response to climate change in [0,0]. (b) Response to climate change in [B+,D] minus the response to climate change in [0,0]. Contour interval given by colorbar.

jet under climate change in these experiments, which is what is seen. There appears to be only a small subtle difference between the response in [0,0] and [B+,D] but, on inspection of the zonal wind responses across the model configurations, particularly in [B,D], there is a pattern that emerges over the NA region. The experiments with larger amounts of low-level drag exhibit a larger strengthening of the winds over western Europe and a larger weakening of the winds over the Nordic sea, which equates to a larger equatorward shift of the NA jet.

Figure 6.18a shows the relationship between the historical jet latitude over the NA, indicated by the lower green sectors in figure 6.17, and the jet latitude shift in response to climate change. There is a strong relationship between the two, with a more poleward tilted jet having a larger equatorward shift under climate change. Although the internal variability is large over this region, as shown by the confidence intervals, subsetting of the data gives similar results indicating that this relationship is robust. This is consistent with the relationship between the NA jet latitude and stationary wave amplitude presented in section 6.3.

The NP jet latitude response is generally very weak in these experiments (figure 6.18b). This is explained by the fact that the largest response to 2xCO2 is not in the node of the climatological winds but at the jet exit region over the North Pacific (see figure 6.3). This may also explain why there is no relationship between the climatology and the response (figure 6.18b). This does not mean that there cannot be a relationship

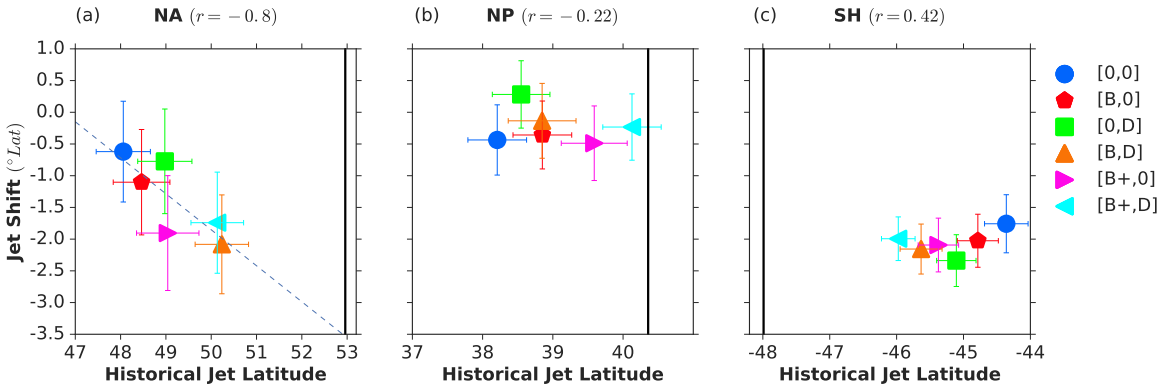

Figure 6.18: Relationship between the DJF 1xCO2 climatological jet latitude and its response to climate change for (a) the NA, (b) the NP and (c) the SH. NA, NP and SH region definitions given in section 6.2.3. r values are the correlation coefficients. Errorbars correspond to the 95% confidence interval based on a two-sided independent student's t-test. Vertical line indicates ERA interim DJF climatological values.

under some other forcing in which the jet latitude shift over the NP is larger, however. While the jet latitude response to CO_2 is large over the SH, there is little relationship between the climatology and the response (figure 6.18), presumably due to the small role of stationary wave fluxes in the climate change response. The relationship between the climatological jet latitude and its response to climate change is also weak in the CMIP5 ensemble in DJF (see Simpson and Polvani 2016, figure 2d).

6.5 Discussion and conclusions

Through a set of experiments designed to systematically vary the magnitude of parameterized low-level orographic drag in CanAM4.1, we have shown that the stationary wave amplitudes and the zonal momentum transport by stationary waves in the NH wintertime are modulated by the strength of the low-level orographic drag. By looking first at the zonal wind response to increased parameterized drag in the 1xCO2 climatology, we found that there was a poleward shift of the midlatitude jets, the amplitude of which increases with increasing drag. Locally, the North Atlantic jet exhibited an increased poleward tilt away from western Europe and there was a weakening of the winds over the central Pacific and a strengthening of the winds over the North Pacific with increased drag. Together, these local changes lead to an improved representation of the zonal winds when compared with ERA interim reanalysis.

We then identified that it is predominantly a change in the stationary eddy momentum flux convergence that contributes towards the change in the NH zonal winds with increased low-level orographic drag. Using the zonally asymmetric component of the meridional winds at 300hPa to visualise the stationary wave field, we found that the increased drag leads to a damping of the waves over the North Pacific and an amplification of the waves over the North Atlantic. Spectral analysis of the meridional winds substantiates this and identifies that it is a damping of the zonal wavenumber 5 meridional winds over the mid-latitudes and an amplification of wavenumber 2 over the high latitudes that lead to changes in the SEMFC. Focusing on the NA jet exit region, we show that there is a strong relationship between the stationary wave amplitudes over the Nordic sea and the NA jet latitude, with stronger stationary waves being associated with a more poleward NA jet. A comparison with the ERA interim meridional wind spectrum reveals that not only are the wavenumber 5 amplitudes too strong in mid-latitudes and the wavenumber 2 amplitudes too weak at high latitudes in [0,0], but that these biases are also present in the CMIP5 multi-model mean spectrum presented in Simpson et al. (2015).

It is important to acknowledge that not all models in the CMIP5 ensemble employ a low-level orographic drag scheme and, if they do, the magnitude of this may vary greatly between them as a result of parameter uncertainty and tuning. Many are also of low horizontal resolution and have smoothed mean orography compared with reality. Since the low-level parameterized orographic drag has been shown to alter the stationary wave amplitudes over the middle and high latitudes, it is possible that the spread seen in the stationary wave amplitudes in the CMIP5 ensemble are a result of their representation of orography. Furthermore, since the SEMFC make the dominant contribution towards the MFC over the NH, it is likely that the equatorward jet biases and lack of NA jet tilt seen across the CMIP5 models are a reflection of biases in their stationary waves and associated momentum forcing. The biases in their stationary waves may be related to the treatment of sub-grid orographic drag, since similar conclusions were drawn by Pithan et al. (2016) using a different model.

By prescribing SST and sea-ice changes from coupled simulations in which the CO_2 was doubled, we demonstrated that the amplitude of the stationary wave response to climate change scales with the climatological stationary wave amplitudes over different regions. Over the Pacific and North America, where the increased orographic drag acts to reduce the stationary wave amplitudes, the meridional wind response to climate

change was also reduced. On the other hand, over the NA, where increased orographic drag acted to amplify the stationary waves, the meridional wind response to climate change was increased with increasing orographic drag. These empirical results are consistent with linear stationary wave theory and suggest that the magnitude of the orographic forcing, which can be altered by the parameterized orographic drag, is important for the stationary wave response to climate change.

Many studies focus on the latitudinal shifting of the mid-latitude jets under climate change and, while we have shown that the stationary waves have an impact on the regional jet shift under climate change, they are also of interest in themselves. For example, in mid-latitudes, large positive meridional wind anomalies lead to the advection of anomalously warm, moist air from the tropics which will have an impact on the local hydrology and temperatures (Nigam and DeWeaver, 2002). Indeed, Simpson et al. (2015) demonstrated the close link between the meridional wind response over North America and the hydroclimate response there. The accurate projection of regional climate change therefore also depends on the accurate representation of the amplitude and location of stationary waves and their response to climate change.

The relationship between the historical stationary wave amplitudes and their response to climate change is likely to depend on the large-scale nature of the circulation response, and thus on the SST and sea-ice forcing prescribed. Nonetheless, this study extends the body of work that highlights the importance of model fidelity and demonstrates that the spread in climatological basic states among models, as a result of parameter tuning or otherwise, can contribute to the uncertainty in the regional circulation response to climate change.

Chapter 7

Conclusions

7.1 Summary

It is important to understand the processes contributing to the spread in the climatological circulation and in the circulation response to climate change that is seen among models. Previous studies have shown sensitivity of the large scale circulation to orographic drag (e.g. Palmer et al. 1986; Lott and Miller 1997; Lott 1999; Zadra et al. 2003; Sandu et al. 2016; Pithan et al. 2016, to name a few). There are, however, different ways in which parameterized (Lott and Miller, 1997; Scinocca and McFarlane, 2000; Zadra et al., 2013) and resolved (Webster et al., 2003; Brown, 2004; Rutt et al., 2006) orographic drag can be represented in models. The primary aim of this body of work was, therefore, to understand how uncertainty in the representation of orography affects modelled atmospheric circulation. A variety of different models and modelling techniques were used across timescales and resolutions to assess the impacts of orography. This approach has meant that a wide area of parameter space could be spanned, generating a dynamic range within which to explore the links between uncertainty in orographic drag parameters[1] and particular features of the circulation.

The main results from this investigation are summarised below:

1. Parameterized orographic drag is not representative of high-resolution resolved orographic drag over the NH mid-latitudes, particularly over the Eastern Hemi-

[1]'Parameters' do not just include tuning parameters in the orographic drag schemes but also aspects like horizontal resolution, parameterization scheme combinations and model dynamics formulation.

sphere, and leads to a systematic wind bias at lower horizontal resolutions in the MetUM (chapters 4 and 5).

2. The correct partitioning of drag parameterization schemes into various processes is uncertain. The fidelity of the modelled circulation has a regional dependence on the particular combination of parameterizations chosen (chapters 4, 5 and 6).

3. The blocking component of the orographic drag parameterization scheme leads to non-robustness of the circulation to changes in resolution (in both the MetUM and ECMWF IFS). The gravity wave drag component also contributes towards the non-robustness in the ECMWF IFS (chapter 5).

4. The assumption of constant winds over the sub-grid orography made by the orographic drag parameterization scheme is strongly violated over the Himalayas. It is proposed that this is partly the cause of the overly-large parameterized orographic blocking in the MetUM and the non-robustness of the circulation to changes in resolution in both the MetUM and ECMWF IFS over this region (chapter 5).

5. The addition of low-level parameterized orographic drag (e.g. downslope wind or blocking) is beneficial for model fidelity across short and long timescales in all of the models considered (chapters 4, 5 and 6).

6. Experiments with CanAM4.1 suggest that the low-level parameterized orographic drag modulates the strength of the NH wintertime stationary waves. Without low-level parameterized orographic drag, the NH stationary wave amplitudes in CanAM4.1 are similar to the CMIP5 multi-model mean. Specifically, they are too strong over the North Pacific and too weak over the North Atlantic relative to reanalysis (chapter 6).

7. The addition of low-level parameterized orographic drag leads to a poleward shift of the mid-latitude jets in the NH and SH. The NH jet shifts are attributed to a change in the zonal momentum fluxes from stationary waves (chapter 6).

8. The amplitude of the NH stationary wave response to climate change in CanAM4.1 scales with the climatological stationary wave amplitude, brought on by changes in the low-level parameterized orographic drag. Due to the connection between

jet latitude and stationary wave amplitude found over the NH, the jet latitude shift with climate change also scales with the climatological jet latitude over the North Atlantic (chapter 6).

7.2 Discussion

In the Introduction to this thesis, the model resolution and parameterization formulation were identified as the main sources of uncertainty in the representation of orography in models. While these two are not completely independent, it is possible to identify their contributions following the results presented in chapters 4, 5 and 6. These contributions are outlined and the implications of this work for the broader field are discussed below. Some discussion on the model evaluation techniques employed is also given.

Non-robustness of orographic drag to model resolution

In chapter 4 the problem of model resolution uncertainty was addressed, specifically how orographic drag (resolved and parameterized) varies with varying horizontal resolution. It was shown that the total orographic drag, resolved plus parameterized, does not remain constant when horizontal resolution is changed. A comparison between the MetUM and ECMWF IFS in section 4.4 revealed that, even with different dynamics, tuning and implementation of the parameterization scheme, the total orographic drag does not remain constant in the NH mid-latitudes in either model. Since the resolved orographic drag changed very little with increased resolution over the mid-latitudes, the resolution sensitivity was attributed to the change in the parameterized orographic drag over this regions, which reduced substantially with increasing resolution. If the total surface drag is not robust to changes in resolution then neither will be the circulation. This means that the climatological circulation is likely to vary from model to model as a result of resolution differences, which may contribute to the circulation spread seen among models.

Chapters 4 and 5 also showed how increasing horizontal resolution reduces the model drift relative to reanalysis and operational analysis. This is a typically observed response to increasing resolution in models and has generally been attributed to an

improved representation of the resolved processes. However, it seems that most of the reduction in error with increasing resolution in the MetUM over the mid-latitudes is coming from the reduction in the error from the parameterized orographic drag, as opposed to the addition of resolved orographic drag. This implies that increasing horizontal resolution in order to better resolve processes may not be the only way of improving the model, since model error can be reduced by improving parameterized processes. This is an important message for modelling centres, since increasing resolution can put a large strain on computational resources and, while the development of improved parameterization schemes may also be difficult and time consuming, an improved representation of unresolved processes may be a more efficient means of reducing model error. What is more, the development process of better parameterization schemes is also likely to give insight into the physical mechanisms at play.

An interesting feature of the resolution sensitivity is its regional dependence. The resolved orographic torques changed very little with resolution over the NH mid-latitudes, whereas the parameterized orographic torques changed dramatically. In contrast, the decrease in parameterized orographic drag over the Northern subtropics was balanced by an almost equivalent increase in resolved orographic drag with increasing resolution. Diagnosis of the resolved and parameterized drag over the Eastern and Western hemispheres indicate that it is the orography over the Eastern Hemisphere, most likely the Himalayan Plateau, that is the cause of this resolution sensitivity. Given that this mountain range is positioned such that it intersects with the mid-latitude jet, this uncertainty from the resolution sensitivity is likely to be important for the structure of the jet over this region.

The differences in formulation and tuning of the parameterization scheme between the ECMWF IFS and MetUM was shown to be important for the overall magnitudes of the individual drag components in chapters 4 and 5, but not for the resolution sensitivity of the total orographic drag. The inability of the models to maintain an equivalent total orographic drag can be attributed to the resolution sensitivity of the parameterization scheme in both the ECMWF IFS and MetUM. Since the scheme is able to adjust to resolution appropriately in certain regions but not others, it suggests that there is something particular related to the scheme's theoretical undertaking rather than just its multiplicative tuning parameters, a hypothesis that is tested in chapter 5.

Compensation and partitioning of drag processes

In the second part of chapter 4 it was shown that, by removing one element of parameterized drag and allowing other drag processes to compensate for this, the substitution of one parameterization scheme for another may not be appropriate in all geographical regions or flow regimes. Similarly, chapter 5 pointed out that different combinations of the downslope wind and blocking components of the orographic drag scheme led to regionally different benefits for the model climatology. The regional dependence of the model error on the relative contributions from parameterized orographic drag suggests that there is likely to be no single combination of tuning parameters or parameterized processes that is optimal for all regions of the globe. As a result, different institutions in different geographic locations with distinctive forecasting or predictive goals will use parameters that are beneficial for their specific purpose, which will generate varying regional circulations among models.

Himalayan orography as a test case for the orographic drag parameterization scheme

The Himalayas were identified as the region over which the non-robustness to changes in resolution was the largest (chapter 4). Chapter 5 isolated the components of the parameterization scheme that led to the non-robustness of the circulation to resolution over this region. In both the MetUM and the ECMWF IFS the blocking component of the parameterized drag was shown to contribute to the non-robustness of the near surface circulation. The gravity wave drag component, on the other hand, was shown to respond well to resolution in the MetUM but contributed significantly to the non-robustness to resolution in the upper atmosphere of the ECMWF IFS. It, therefore, seems likely that variations in the partitioning of the drag into the upper and lower atmosphere component is important for generating climatological spread among models. In chapter 5 it was also suggested that some of the error in the parameterized orographic gravity wave drag may be a result of the error in the parameterized orographic blocking drag, since these two are closely linked through the Froude number. This means that finding an optimal formulation in which both processes are accurately simulated leads to further complications in the representation of parameterized orographic drag in models.

Section 5.4 dissected the output from the blocking component of the orographic drag parameterization scheme in the MetUM over the Himalayan Plateau in detail. Here, the assumption of constant wind speed over the height of the sub-grid orography was shown to be inappropriate for the Himalayan Plateau, since the vertical wind shear can be very large where the orography intersects with the mid-latitude jet. Furthermore, by looking at vertical wind and parameterized tendency profiles, it was shown that even a small decrease in the sub-grid orographic height, brought about by an increase in resolution, may dramatically decrease the vertically integrated parameterized orographic drag. The too-large values of the parameterized orographic drag in the low resolution version of the models and the non-robustness to resolution over the Himalayas were, therefore, attributed to the parameterization scheme's treatment of the winds. This implies that a new formulation of the orographic drag parameterization, one in which the vertical wind shear is taken into account, may be beneficial.

Impact of orographic drag parameter uncertainty on the circulation

Chapter 6 was primarily focused on the impacts of varying the orographic drag formulation and unconstrained parameters on model fidelity and circulation uncertainty. Here, low-level parameterized orographic drag was shown to be beneficial for the model's time mean circulation. This is consistent with the findings in chapter 5, where the parameterized orographic drag was show to reduce the short range forecast drift of the model. By increasing the parameterized orographic drag, some of the biases that are prevalent in low resolution climate models could be alleviated, as was found in Pithan et al. (2016). Specifically, an increase in the parameterized orographic drag improved the location and amplitude of the NH wintertime stationary waves and the mean latitudinal position of the mid-latitude jets in both hemispheres, placing them further poleward.

The increased low-level parameterized orographic drag generally led to a damping of the stationary waves over the North Pacific and an amplification of the stationary waves over the North Atlantic. This is significant because the CMIP5 mean stationary wave amplitudes exhibit too large amplitudes over the North Pacific and too weak amplitudes over the North Atlantic, relative to ERA-interim reanalysis. Many climate modelling centres do not employ an element of low-level orographic drag in their parameterizations and the results of this work show that this is an important process that should be accounted for. It also suggests that orography may be a commonly

underrepresented process among these models, given that they are resolving less of the orographic spectrum than NWP models, which may give rise to systematic model biases.

The results in chapter 6 demonstrate that a variety of different climatological circulations can be generated from varying unconstrained parameters in and employing different combinations of orographic drag parameterizations. As well as causing systematic biases, this suggests that some of the spread seen among models may also be due to the formulation and choice of parameters in their orographic drag schemes.

Chapters 4 and 5 demonstrated that orographic drag can have an impact on model drift across short timescales. In general, the addition of orographic drag, whether it be parameterized or resolved, was shown to reduce the model short-range drift relative to reanalysis (in the nudged framework) and analysis (in short-range forecast framework). In accordance with other studies that have shown that orography is beneficial for forecast scores, the work presented in these chapters reinforces the importance of orography for numerical weather prediction. Additionally, the results in chapter 6 and the work of Pithan et al. (2016) demonstrate that the addition of parameterized orographic drag also leads to an improved climatological circulation over longer timescales, demonstrating its importance for climate models. This suggests that the errors seen at short range, which are more readily attributable to specific processes, correspond well with climatological errors and that the seamless modelling approach may be a fruitful way of constraining the processes that are important for model fidelity across timescales.

Impact of orographic drag parameter uncertainty on the circulation response to climate change

As well as having an impact on the climatological spread seen across models, chapter 6 demonstrated how varying unconstrained orographic drag parameters within one model may lead to different circulation responses to climate change. In particular, changes in the orographic forcing, brought about by changes in the parameterized orographic drag, can lead to a different magnitude of the stationary wave response to climate change. The magnitude of the stationary wave response to climate change has been shown to be uncertain among the CMIP5 models. While some of this spread may be explained by different zonal wind changes, Simpson et al. (2015) showed, using the

CMIP5 ensemble, that there is a relationship between the climatological stationary wave amplitudes and their response to climate change over North America. Similarly, chapter 6 showed that this relationship exists not only over North America but also over the North Atlantic. This is a particularly important result since it motivates the need for fidelity in a model's basic state and shows how the representation of orography within models plays a role in this.

The stationary waves were shown to have a dominant impact on the zonal momentum transport in the NH, compared with the momentum fluxes from transient motions. Since the magnitude of the stationary wave response to climate change was shown to scale with the parameterized orographic drag, the regional jet response to climate change also scaled with the parameterized orographic drag. This is a type of emergent constraint, since the uncertainty in the climate change response can be reduced via calibrating the stationary waves, through orographic drag or otherwise, through observations. Many studies have recognised that the zonal wind response to climate change is very uncertain in the NH wintertime and the spread in the stationary wave response may contribute to this.

Model evaluation techniques

As well as making contributions to the understanding of orographic drag processes in the atmospheric circulation, this work also employs different model evaluation techniques. Although these have been used by others for various purposes, here they are tailored towards the understanding of orographic drag processes. For example, in chapter 4, a nudging technique is employed that provides a 'built-in' model error diagnostic, in the sense that the nudging tendencies reflect the short-range drift of the model. The vertically integrated momentum budget and nudging framework is ideal for looking at surface drag feedbacks on model error. It is a useful model evaluation and validation method that can easily be implemented by climate modelling centres and can also be used for model inter-comparison.

The techniques employed in chapter 5 allow for the isolation of the impacts from additional resolved orography on the circulation, by prescribing low resolution orography in a high resolution model. They also provide a means of constraining the unresolved processes and validating the orographic drag parameterization scheme. Using high resolution simulations in this manner, similarly to convection permitting models, provides

an alternative to direct observations of orographic drag that whilst highly prized are unobtainable over very complex terrain. Of course, the modelled response is not reality and must itself be validated. Nevertheless, chapter 5 and work by several other (e.g. Vosper 2015; Vosper et al. 2016) has helped demonstrate the validity and advantages of using high resolution models for parameterization validation.

Perturbed physics ensembles (PPEs) have previously been used to generate a distribution of model configurations in order to quantify the uncertainty in the climate change response linked to parameter uncertainty (e.g. Murphy et al. 2004; Stainforth et al. 2005). In PPEs, uncertain parameters in different physics parameterization schemes are varied within the range of what is considered realistic. These model configurations are then used to perform climate change experiments. These parameters are, however, not varied systematically but, rather, all at once. This means that they do not easily allow for the quantification of uncertainty due to specific processes or the attribution of physical mechanisms. In chapter 6 the parameters within one particular parameterization scheme, the orographic drag scheme, are systematically varied. This methodology then allows certain aspects of circulation uncertainty, namely stationary wave amplitude and regional jet latitude, related specifically to orographic drag processes to be quantified. Although it may not be possible to apply this procedure to every unconstrained parameter within a model, as a result of computational limitations, chapter 6 illustrates its usefulness in ascribing possible causes of systematic model bias and spread in the regional climate change response.

7.3 Open questions and future work

The work presented in this thesis is by no means exhaustive and raises several questions. In the following section a series of open questions are discussed and possible future work aimed at answering them is presented.

Does short range error reduction correspond to time mean circulation error reduction?

Chapters 4, 5 and 6 made reference to other studies that have looked at the relationship between short-range forecast errors and climatological biases. These studies have

generally found good spatial agreement between the two. Section 4.6 demonstrated how the nudging framework can be used to diagnose errors related to orographic drag and how changes to the parameterized orographic drag can lead to beneficial results over certain regions over short timescales. What is more, chapter 5 demonstrated how varying parameters within the orographic drag scheme can lead to an improved representation of the time-mean circulation. This evokes questions about how the benefits seen over short timescales (in the nudged framework), from adjusting the parameterization schemes, feed into the time-mean climatology. By performing an ensemble of experiments in which the parameterized orographic drag is altered (within the bounds of observations) in the nudged framework it may be possible to arrive at an optimal configuration in which the nudging tendencies are minimised. This is essentially a sort of tuning. Performing longer integrations with the model configuration that minimises the nudging tendencies and evaluating its performance will, firstly, inform whether short range error reduction is beneficial for climatological error reduction and, secondly, give an optimal set of orographic drag parameters.

How do the different treatments of resolved orography affect the circulation?

The resolved orography in the Met Office Unified Model was revealed to be much smoother than the resolved orography in the ECMWF IFS at comparable resolutions in section 4.4. Chapters 4, 5 and 6 demonstrated that models require orographic drag (parameterized or resolved) to maintain their circulation. The partitioning of the surface drag into its resolved and parameterized parts may be weighted more to parameterized drag in the MetUM to account for this smoothing. It is of interest to test whether the addition of power at the smaller scales, through reducing the orographic filtering, has a substantial impact on the large scale circulation. This can then be compared to the impact of the parameterized drag to asses whether additional resolved orography may be used in place of such large parameterized orographic drag. While it may not be possible to remove all of the parameterized drag, additional resolved orography (inline with reality, unlike envelope orography) would seem preferable to very large amounts of parameterized orographic drag.

How can the parameterized orographic drag be reformulated to account for vertical wind shear?

In chapter 5 it was shown that the approximation of constant vertical wind that is used in the orographic drag parameterization scheme is not appropriate for the Himalayan Plateau. An alternative way of calculating the Froude number, which determines the depth of the blocked layer in the orographic drag parameterization scheme, seems to be required. One possibility may be to calculate the Froude number iteratively from the model surface upwards until some critical value, at which gravity wave generation is possible, has been reached. This may circumvent the problem of averaging strong winds aloft with weak winds below, but may lead to complications over other regions. The reformulation of the parameterization scheme will be further complicated by the fact that, firstly, the model is well tuned to the current settings and, secondly, the gravity wave drag component of the scheme is also dependent on the Froude number. A set of sensitivity experiments, in which the calculation of the Froude number is altered to account for strong vertical wind shear, would seem like a suitable starting point towards making the parameterization scheme more realistic over such regions.

What is the parameterized orographic drag doing in the SH?

The work presented in chapter 4 and in Pithan et al. (2016) implies that the climatological Southern Hemisphere circulation has a robust response to parameterized low-level orographic drag, which is not negligible. This response is characterised by a poleward shift of the SH mid-latitude jet with increasing low-level drag. While the parameterized orographic drag is smaller in the SH compared with the NH and is located primarily on the flanks of the SH jet, its impact on the SH circulation is comparable to that in the NH. Understanding the reason for this disproportionately large response would be of interest, since orographic impacts in the SH may be underestimated in general. The mechanism of the response in the SH appears far more complex and less direct that that of the NH.

In the experiments of chapter 4 the increased low-level orographic drag led to a decrease in the propagating gravity wave drag, which was not shown. The decreased gravity wave drag is likely to have an impact on the transition to stratospheric easterlies that occurs in the SH between November and January (McLandress et al., 2012).

Previous studies have made connections between the date of the transition to easterlies and the tropospheric jet in the SH (e.g. Sun et al. 2014). It is, therefore, possible that the SH response is not a result of the change in the low-level blocking alone but rather a response to the decreased parameterized orographic gravity wave drag. This hypothesis could be investigated by prescribing the gravity wave drag component of the orographic drag parameterization from the control simulation, similarly to Sigmond and Scinocca (2010), in an experiment in which only the low-level parameterized orographic drag component is altered. This way, it can be deduced whether it is the orographic gravity wave drag or the low-level blocking that is the cause of the tropospheric jet response.

Why is the stationary wave response to drag opposite over the NA and NP?

Another open question from the work in chapter 6 arises from the difference in the response seen over the North Pacific compared with the North Atlantic. It was shown that the increased low-level parameterized orographic drag led to a damping of the waves over the North Pacific but to an amplification of the waves over the North Atlantic, which were accompanied by poleward jet shifts over both regions. While the North Pacific response may be more easily attributed to the drag over the Himalayan region, the North Atlantic response is less clear. It is possible that the response over the NA is directly related to the increased drag over the Rocky Mountains or even the drag over Greenland, which is also very large. However, the change in the NP jet latitude is likely to change the interaction of the impinging winds with the resolved Rocky Mountains and, thus, lead to a change in the stationary waves downstream. It could, therefore, be either the direct influence of the parameterized orographic drag over the Rockies/Greenland or the change in the interaction with resolved orography that leads to the response over the North Atlantic. In order to understand the controlling region and mechanism, a set of modelling experiments could be performed in which the low-level parameterized orographic drag is altered only over the Rockies, over the Himalayas, over Greenland, or over various combinations of the three.

Bibliography

Andrews, D. G. and McIntyre, M. E. (1976). Planetary Waves in Horizontal and Vertical Shear: The Generalized Eliassen-Palm Relation and the Mean Zonal Acceleration. *J. Atmos. Sci.*, 33(11):2031–2048.

Arakawa, A. and Lamb, V. R. (1977). Computational design of the basic dynamical processes of the UCLA general circulation model.

Barnes, E. A. and Polvani, L. (2013). Response of the midlatitude jets, and of their variability, to increased greenhouse gases in the CMIP5 models. *J. Clim.*, 26(18):7117–7135.

Beljaars, A. C. M., Brown, A. R., and Wood, N. (2004). A new parametrization of turbulent orographic form drag. *Q. J. R. Meteorol. Soc.*, 130(599):1327–1347.

Boer, G. J. (1990). Earth-atmosphere exchange of angular momentum simulated in a general circulation model and implications for the length of day. *J. Geophys. Res.*, 95(D5):5511.

Booker, J. R. and Bretherton, F. P. (1967). The critical layer for internal gravity waves in a shear flow. *J. Fluid Mech.*, 27(03):513.

Bougeault, P., Beau, I., and Stein, J. (1992). Validation of meteorological models and parametrizations with observations of the PYREX field experiment. *Semin. Valid. Model. over Eur. 7-11 Sept. 1992, Conf. Pap. ECMWF.*

Bougeault, P., Benech, B., Bessemoulin, P., Carissimo, B., Clar, A. J., Pelon, J., Petitdidier, M., Richard, E., Bougeault, P., Benech, B., Bessemoulin, P., Carissimo,

B., Clar, A. J., Pelon, J., Petitdidier, M., and Richard, E. (1997). PYREX: A summary of findings. *Bull. Am. Meteorol. Soc.*, 78(4):637–650.

Boyer, D. L. and Davies, P. A. (2000). Laboratory studies of orographic effects in rotating and stratified flows. *Annu. Rev. Fluid Mech.*, 32(1):165–202.

Bracegirdle, T. J., Shuckburgh, E., Sallee, J. B., Wang, Z., Meijers, A. J. S., Bruneau, N., Phillips, T., and Wilcox, L. J. (2013). Assessment of surface winds over the Atlantic, Indian, and Pacific ocean sectors of the southern ocean in cmip5 models: Historical bias, forcing response, and state dependence. *J. Geophys. Res. Atmos.*, 118(2):547–562.

Brayshaw, D. J., Hoskins, B. J., and Blackburn, M. (2009). The basic ingredients of the North Atlantic storm track. Part I: Landsea contrast and orography. *J. Atmos. Sci.*, 66(1986):2539–2558.

Brewer, A. W. (1949). Evidence for a world circulation provided by the measurements of helium and water vapour distribution in the stratosphere. *Q. J. R. Meteorol. Soc.*, 75(326):351–363.

Brown, A. (2004). Resolution dependence of orographic torques. *Q. J. R. Meteorol. Soc.*, 130(603):3029–3046.

Brown, A., Milton, S., Cullen, M., Golding, B., Mitchell, J., Shelly, A., Brown, A., Milton, S., Cullen, M., Golding, B., Mitchell, J., and Shelly, A. (2012). Unified modeling and prediction of weather and climate: A 25-year journey. *Bull. Am. Meteorol. Soc.*, 93(12):1865–1877.

Butler, A. H., Thompson, D. W. J., and Heikes, R. (2010). The steady-state atmospheric circulation response to climate change-like thermal forcings in a simple general circulation model. *J. Clim.*, 23(13):3474–3496.

Carissimo, B. C., Pierrehumbert, R. T., and Pham, H. L. (1988). An estimate of mountain drag during ALPEX for comparison with numerical models. *J. Atmos. Sci.*, 45(13):1949–1960.

Chao, B. (1988). Correlation of interannual length-of-day variation with El Niño/Southern oscillation, 1972-1986. *J. Geophys. Res. Solid Earth (1978 ...*, 93(B7):7709–7715.

Charney, J. G. and Drazin, P. G. (1961). Propagation of planetary-scale disturbances from the lower into the upper atmosphere. *J. Geophys. Res.*, 66(1):83–109.

Charney, J. G. and Eliassen, A. (1949). A numerical nethod for predicting the perturbations of the middle latitude westerlies. *Tellus*, 1(2):38–54.

Chen, G., Held, I. M., and Robinson, W. a. (2007). Sensitivity of the latitude of the surface westerlies to surface friction. *J. Atmos. Sci.*, 64(8):2899–2915.

Chen, G. and Zurita-Gotor, P. (2008). The tropospheric jet response to prescribed zonal forcing in an idealized atmospheric model. *J. Atmos. Sci.*, 65(7):2254–2271.

Chouinard, C., Béland, M., and McFarlane, N. (1986). A simple gravity wave drag parametrization for use in medium-range weather forecast models. *Atmosphere-Ocean*, 24(2):91–110.

Clark, T. L. and Miller, M. J. (1991). Pressure drag and momentum fluxes due to the Alps. II: Representation in large-scale atmospheric models. *Q. J. R. Meteorol. Soc.*, 117(499):527–552.

Clark, T. L. and Peltier, W. R. (1977). On the evolution and stability of finite-amplitude mountain waves. *J. Atmos. Sci.*, 34(11):1715–1730.

Clark, T. L. and Peltier, W. R. (1984). Critical level reflection and the resonant growth of nonlinear mountain waves. *J. Atmos. Sci.*, 41(21):3122–3134.

Cook, K. and Held, I. (1992). The stationary response to large-scale orography in a general circulation model and a linear model. *J. Atmos. Sci.*, 49(6):525–539.

Dalcher, A. and Kalnay, E. (1987). Error growth and predictability in operational ECMWF forecasts. *Tellus A*, 39A(5):474–491.

Davies, L. A. and Brown, A. R. (2001). Assessment of which scales of orography can be credibly resolved in a numerical model. *Q. J. R. Meteorol. Soc.*, 127(574):1225–1237.

Davies, T. (2014). Lateral boundary conditions for limited area models. *Q. J. R. Meteorol. Soc.*, 140(678):185–196.

Dee, D. P., Uppala, S. M., Simmons, A. J., Berrisford, P., Poli, P., Kobayashi, S., Andrae, U., Balmaseda, M. A., Balsamo, G., Bauer, P., Bechtold, P., Beljaars, A. C. M., van de Berg, L., Bidlot, J., Bormann, N., Delsol, C., Dragani, R., Fuentes, M., Geer, A. J., Haimberger, L., Healy, S. B., Hersbach, H., Hólm, E. V., Isaksen, L., Kållberg, P., Köhler, M., Matricardi, M., Mcnally, A. P., Monge-Sanz, B. M., Morcrette, J. J., Park, B. K., Peubey, C., de Rosnay, P., Tavolato, C., Thépaut, J. N., and Vitart, F. (2011). The ERA-Interim reanalysis: Configuration and performance of the data assimilation system. *Q. J. R. Meteorol. Soc.*, 137(656):553–597.

Delsole, T. and Shukla, J. (2010). Model fidelity versus skill in seasonal forecasting. *J. Clim.*, 23(18):4794–4806.

Denis, B., Laprise, R., Caya, D., and Côté, J. (2002). Downscaling ability of one-way nested regional climate models: The Big-Brother Experiment. *Clim. Dyn.*, 18(8):627–646.

DeWeaver, E. and Nigam, S. (2000). Do stationary waves drive the zonal-mean jet anomalies of the Northern Winter? *J. Clim.*, 13(13):2160–2176.

Diamantakis, M., Davies, T., and Wood, N. (2007). An iterative time-stepping scheme for the Met Office's semi-implicit semi-Lagrangian non-hydrostatic model. *Q. J. R. Meteorol. Soc.*, 133(625 B):997–1011.

Dobson, G. M. B. (1956). Origin and distribution of the polyatomic molecules in the atmosphere. *Proc. R. Soc. London A Math. Phys. Eng. Sci.*, 236(1205).

ECMWF (2016). IFS documentation part III: Dynamics and numerical procedures. *IFS Doc. CY43R1, B. Chapter, ECMWF.*, CY43R1.

Egger, J. (1976). The linear response of a hemispheric twolevel primitive equation model to forcing by topography. *Mon. Weather Rev.*, 104(4):351–364.

Eliassen, A. and Palm, E. (1960). On the transfer of energy in stationary mountain waves. *Geofys. Publ.*, 22(3):1–23.

Epifanio, C. C. and Qian, T. (2008). Waveturbulence interactions in a breaking mountain wave. *J. Atmos. Sci.*, 65(10):3139–3158.

Ertel, H. (1942a). Ein neuer hydrodynamischer Erhaltungssatz. *Naturwissenschaften*, 30(36):543–544.

Ertel, H. (1942b). Ein neuer hydrodynamischer Wirbelsatz. *Meteorol. Zeitschrift*, 59(9):277–281.

Garcia, R. R. and Solomon, S. (1985). The effect of breaking gravity waves on the dynamics and chemical composition of the mesosphere and lower thermosphere. *J. Geophys. Res.*, 90(D2):3850.

Georgelin, M., Bougeault, P., Black, T., Brzovic, N., Buzzi, A., Calvo, J., Casse, V., Desgagné, M., El-Khatib, R., and Geleyn, J.-F. (2000). The second COMPARE exercise: a model intercomparison using a case of a typical mesoscale orographic flow, the PYREX IOP3. *Q. J. R. Meteorol. Soc.*, 126(564):991–1029.

Gill, A. E. (1982). *Atmosphere-ocean dynamics*. Academic Press.

Golledge, N. R., Kowalewski, D. E., Naish, T. R., Levy, R. H., Fogwill, C. J., and Gasson, E. G. W. (2015). The multi-millennial Antarctic commitment to future sea-level rise. *Nature*, 526(7573):421–425.

Grose, W. L. and Hoskins, B. J. (1979). On the influence of orography on large-scale atmospheric flow. *J. Atmos. Sci.*, 36(2):223–234.

Hartmann, D. L. (2007). The atmospheric general circulation and its variability. *J. Meteorol. Soc. Japan*, 85B:123–143.

Hawkins, E. and Sutton, R. (2009). The potential to narrow uncertainty in regional climate predictions. *Bull. Am. Meteorol. Soc.*, 90(8):1095–1107.

Hayes, M. (1977). A note on group velocity. *Proc. R. Soc. A Math. Phys. Eng. Sci.*, 354(1679):533–535.

Haynes, P. H., McIntyre, M. E., Shepherd, T. G., Marks, C. J., and Shine, K. P. (1991). On the downward control of extratropical diabatic circulations by eddy-induced mean zonal forces. *J. Atmos. Sci.*, 48(4):651–678.

Held, I. M., Ting, M., and Wang, H. (2002). Northern winter stationary waves: Theory and modeling. *J. Clim.*, 15(16):2125–2144.

Hitchcock, P. and Haynes, P. H. (2014). Zonally symmetric adjustment in the presence of artificial relaxation. *J. Atmos. Sci.*, 71(11):4349–4368.

Holton, J. R. (1979). *An introduction to dynamic meteorology*. Academic Press.

Hortal, M. and Simmons, A. J. (1991). Use of reduced Gaussian grids in spectral models. *Mon. Weather Rev.*, 119(4):1057–1074.

Hoskins, B., Fonseca, R., Blackburn, M., and Jung, T. (2012). Relaxing the Tropics to an 'observed' state: Analysis using a simple baroclinic model. *Q. J. R. Meteorol. Soc.*, 138(667):1618–1626.

Hoskins, B. J., Simmons, A. J., and Andrews, D. G. (1977). Energy dispersion in a barotropic atmosphere. *Q. J. R. Meteorol. Soc.*, 103(438):553–567.

Huang, H.-P., Sardeshmukh, P. D., and Weickmann, K. M. (1999). The balance of global angular momentum in a long-term atmospheric data set. *J. Geophys. Res.*, 104(D2):2031.

Huang, H.-P. and Weickmann, K. M. (2008). On the computation of the mountain torque from gridded global datasets. *Mon. Weather Rev.*, 136(10):4005–4009.

Jung, T. (2011). Diagnosing remote origins of forecast error: Relaxation versus 4D-Var data-assimilation experiments. *Q. J. R. Meteorol. Soc.*, 137(656):598–606.

Junge, M. M., Blender, R., Fraedrich, K., Gayler, V., Luksch, U., and Lunkeit, F. (2005). A world without Greenland: Impacts on the Northern Hemisphere winter circulation in low- and high-resolution models. *Clim. Dyn.*, 24(2-3):297–307.

Kasahara, A., Sasamori, T., and Washington, W. M. (1973). Simulation experiments with a 12-Layer stratospheric global circulation Model. I. Dynamical effect of the Earth's orography and thermal influence of continentality. *J. Atmos. Sci.*, 30(7):1229–1251.

Kharin, V. V. and Scinocca, J. F. (2012). The impact of model fidelity on seasonal predictive skill. *Geophys. Res. Lett.*, 39(17):L18803.

Kim, Y.-J. and Arakawa, A. (1995). Improvement of orographic gravity wave parameterization using a mesoscale gravity wave model. *J. Atmos. Sci.*, 52(11):1875–1902.

Klinker, E. and Sardeshmukh, P. D. (1992). The diagnosis of mechanical dissipation in the atmosphere from large-scale balance requirements. *J. Atmos. Sci.*, 49(7):608–627.

Krüger, K., Naujokat, B., and Labitzke, K. (2005). The unusual midwinter warming in the Southern Hemisphere stratosphere 2002: A comparison to Northern Hemisphere phenomena. *J. Atmos. Sci.*, 62(3):603–613.

Laprise, R. and Girard, C. (1990). A spectral general circulation model using a piecewise-constant finite-element representation on a hybrid vertical coordinate system. *J. Clim.*, 3(1):32–52.

Lilly, D. K. (1978). A severe downslope windstorm and aircraft turbulence event induced by a mountain wave. *J. Atmos. Sci.*, 35(1):59–77.

Limpasuvan, V. and Hartmann, D. L. (2000). Wave-maintained annular modes of climate variability. *J. Clim.*, 13(24):4414–4429.

Lock, A. P., Brown, A. R., Bush, M. R., Martin, G. M., and Smith, R. N. B. (2000). A new boundary layer mixing scheme. Part I: scheme description and single-column model tests. *Mon. Weather Rev.*, 128(9):3187–3199.

Lott, F. (1999). Alleviation of stationary biases in a GCM through a mountain drag parameterization scheme and a simple representation of mountain lift forces. *Mon. Weather Rev.*, 127(5):788–801.

Lott, F. and Miller, M. J. (1997). A new subgrid-scale orographic drag parametrization: Its formulation and testing. *Q. J. R. Meteorol. Soc.*, 123(537):101–127.

Ma, H. Y., Xie, S., Klein, S. A., Williams, K. D., Boyle, J. S., Bony, S., Douville, H., Fermepin, S., Medeiros, B., Tyteca, S., Watanabe, M., and Williamson, D. (2014). On the correspondence between mean forecast errors and climate errors in CMIP5 models. *J. Clim.*, 27(4):1781–1798.

Manabe, S. and Terpstra, T. B. (1974). The effects of mountains on the general circulation of the atmosphere as identified by numerical experiments. *J. Atmos. Sci.*, 31(1):3–42.

Manzini, E., Karpechko, A. Y., Anstey, J., Baldwin, M. P., Black, R. X., Cagnazzo, C., Calvo, N., Charlton-Perez, A., Christiansen, B., Davini, P., Gerber, E., Giorgetta,

M., Gray, L., Hardiman, S. C., Lee, Y. Y., Marsh, D. R., McDaniel, B. A., Purich, A., Scaife, A. A., Shindell, D., Son, S. W., Watanabe, S., and Zappa, G. (2014). Northern winter climate change: Assessment of uncertainty in CMIP5 projections related to stratosphere-troposphere coupling. *J. Geophys. Res. B Solid Earth*, 119(13):7979–7998.

Martin, G. M., Milton, S. F., Senior, C. A., Brooks, M. E., Ineson, S., Reichler, T., and Kim, J. (2010). Analysis and reduction of systematic errors through a seamless approach to modeling weather and climate. *J. Clim.*, 23(22):5933–5957.

Matsuno, T. (1970). Vertical propagation of stationary planetary waves in the winter Northern Hemisphere.

Matsuno, T. (1971). A dynamical model of the stratospheric sudden warming. *J. Atmos. Sci.*, 28(8):1479–1494.

McFarlane, N. A. (1987). The effect of orographically excited gravity wave drag on the general circulation of the lower stratosphere and troposphere.

McLandress, C., Shepherd, T. G., Polavarapu, S., and Beagley, S. R. (2012). Is missing orographic gravity wave drag near 60S the cause of the stratospheric zonal wind biases in chemistry-climate models? *J. Atmos. Sci.*, 69(3):802–818.

Miller, M. J., Palmer, T. N., and Swinbank, R. (1989). Parametrization and influence of subgridscale orography in general circulation and numerical weather prediction models. *Meteorol. Atmos. Phys.*, 40(1-3):84–109.

Murphy, J. M., Sexton, D. M. H., Barnett, D. N., Jones, G. S., Webb, M. J., Collins, M., and Stainforth, D. A. (2004). Quantification of modelling uncertainties in a large ensemble of climate change simulations. *Nature*, 430(7001):768–772.

Nappo, C. J. (2013). *An introduction to atmospheric gravity waves*. Academic.

Nigam, S. and DeWeaver, E. (2002). *Stationary waves (orographic and thermally forced)*. Academic Press, Elsevier Science, London.

Nigam, S., Held, I. M., and Lyons, S. W. (1988). Linear simulation of the stationary eddies in a GCM. Part II: The mountain model. *J. Atmos. Sci.*, 45(9):1433–1452.

Nishii, K., Nakamura, H., and Orsolini, Y. J. (2011). Geographical dependence observed in blocking high influence on the stratospheric variability through enhancement and suppression of upward planetary-wave propagation. *J. Clim.*, 24(24):6408–6423.

NOAA (2017). ESRL : PSD : Boulder Wind Events.

Palmer, T. N., Shutts, G. J., and Swinbank, R. (1986). Alleviation of a systematic westerly bias in general circulation and numerical weather prediction models through an orographic gravity wave drag parametrization. *Q. J. R. Meteorol. Soc.*, 112(474):1001–1039.

Peltier, W. R. and Clark, T. L. (1979). The evolution and stability of finite-amplitude mountain waves. Part II: Surface wave drag and severe downslope windstorms. *J. Atmos. Sci.*, 36(8):1498–1529.

Phillips, D. S. (1984). Analytical surface pressure and drag for linear hydrostatic flow over three-dimensional elliptical mountains. *J. Atmos. Sci.*, 41(6):1073–1084.

Phillips, T. J., Potter, G. L., Williamson, D. L., Cederwall, R. T., Boyle, J. S., Fiorino, M., Hnilo, J. J., Olson, J. G., Xie, S., and Yio, J. J. (2004). Evaluating parameterizations in general circulation models: Climate simulation meets weather prediction. *Bull. Am. Meteorol. Soc.*, 85(12):1903–1915.

Pithan, F., Shepherd, T. G., Zappa, G., and Sandu, I. (2016). Climate model biases in jet streams, blocking and storm tracks resulting from missing orographic drag. *Geophys. Res. Lett.*, 43(13):7231–7240.

Plumb, R. A. (1985). On the three-dimensional propagation of stationary waves. *J. Atmos. Sci.*, 42(3):217–229.

Pope, V. D. and Stratton, R. A. (2002). The processes governing horizontal resolution sensitivity in a climate model. *Clim. Dyn.*, 19(3-4):211–236.

Quiroz, R. S. (1986). The association of stratospheric warmings with tropospheric blocking. *J. Geophys. Res.*, 91(D4):5277.

Ralph, F. M., Neiman, P. J., and Levinson, D. (1997). Lidar observations of a breaking mountain wave associated with extreme turbulence. *Geophys. Res. Lett.*, 24(6):663–666.

Rawlins, F., Ballard, S. P., Bovis, K. J., Clayton, A. M., Li, D., Inverarity, G. W., Lorenc, A. C., and Payne, T. J. (2007). The Met Office global four-dimensional variational data assimilation scheme. *Q. J. R. Meteorol. Soc.*, 133(623):347–362.

Ringler, T. D. and Cook, K. H. (1997). Factors controlling nonlinearity in mechanically forced stationary waves over orography. *J. Atmos. Sci.*, 54(22):2612–2629.

Rossby, C.-G. (1939). Relation between variations in the intensity of the zonal circulation of the atmosphere and the displacements of the semi-permanent centers of action. *J. Mar. Res.*, 2(1):38–55.

Rutt, I. C., Thuburn, J., and Staniforth, A. (2006). A variational method for orographic filtering in NWP and climate models. *Q. J. R. Meteorol. Soc.*, 132(619):1795–1813.

Salstein, D. A. and Rosen, R. D. (1994). Topographic forcing of the atmosphere and a rapid change in the length of day.

Sandu, I., Bechtold, P., Beljaars, A., Bozzo, A., Pithan, F., Shepherd, T. G., and Zadra, A. (2016). Impacts of parameterized orographic drag on the Northern Hemisphere winter circulation. *J. Adv. Model. Earth Syst.*, 8(1):196–211.

Schubert, W., Ruprecht, E., Hertenstein, R., Ferreira, R. N., Taft, R., Rozoff, C., Ciesielski, P., and Kuo, H.-C. (2004). English translations of twenty-one of Ertel's papers on geophysical fluid dynamics. *Meteorol. Zeitschrift*, 13(6):527–576.

Scinocca, J. F. and McFarlane, N. A. (2000). The parametrization of drag induced by stratified flow over anisotropic orography. *Q. J. R. Meteorol. Soc.*, 126(568):2353–2393.

Scinocca, J. F., McFarlane, N. A., Lazare, M., Li, J., and Plummer, D. (2008). The CCCma third generation AGCM and its extension into the middle atmosphere. *Atmos. Chem. Phys.*, 8:7055–7074.

Shepherd, T. G. (2014). Atmospheric circulation as a source of uncertainty in climate change projections. *Nat. Geosci.*, 7(10):703–708.

Shepherd, T. G., Plummer, D. A., Scinocca, J. F., Hegglin, M. I., Fioletov, V. E., Reader, M. C., Remsberg, E., von Clarmann, T., and Wang, H. J. (2014). Reconciliation of halogen-induced ozone loss with the total-column ozone record. *Nat. Geosci.*, 7(6):443–449.

Sigmond, M. and Scinocca, J. F. (2010). The influence of the basic state on the Northern Hemisphere circulation response to climate change. *J. Clim.*, 23(6):1434–1446.

Simpson, I. R. ., Shaw, T. A., and Seager, R. (2014). A diagnosis of the seasonally and longitudinally varying mid-latitude circulation response to global warming. *J. Atmos. Sci.*, 71(7):2489–2515.

Simpson, I. R. and Polvani, L. M. (2016). Revisiting the relationship between jet position, forced response, and annular mode variability in the southern midlatitudes. *Geophys. Res. Lett.*, 43(6):2896–2903.

Simpson, I. R., Seager, R., Ting, M., and Shaw, T. A. (2015). Causes of change in Northern Hemisphere winter meridional winds and regional hydroclimate. *Nat. Clim. Chang.*, 6:65–70.

Smagorinsky, J. (1953). The dynamical influence of large-scale heat sources and sinks on the quasi-stationary mean motions of the atmosphere. *Q. J. R. Meteorol. Soc.*, 79(341):342–366.

Smith, R. B. (1979). Some aspects of the quasi-geostrophic flow over mountains. *J. Atmos. Sci.*, 36(12):2385–2393.

Smith, R. B. (1980). Linear theory of stratified hydrostatic flow past an isolated mountain. *Tellus*, 32(4):348–364.

Smith, S. A., Doyle, J. D., Brown, A., and Webster, S. (2005). Sensitivity of resolved mountain drag to model resolution for map case studies. *Hrvat. Meteoroloski Cas.*, 132(40):264–267.

Stainforth, D. A., Aina, T., Christensen, C., Collins, M., Faull, N., Frame, D. J., Kettleborough, J. A., Knight, S., Martin, A., Murphy, J. M., Piani, C., Sexton, D., Smith, L. A., Spicer, R. A., Thorpe, A. J., and Allen, M. R. (2005). Uncertainty in predictions of the climate response to rising levels of greenhouse gases. *Nature*, 433(7024):403–406.

Staniforth, A., White, A., Wood, N., Thuburn, J., Zerroukat, M., Cordero, E., Davies, T., and Diamantakis, M. (2006). Joy of U.M. 6.3 - Model formulation. *Unified Model Doc. Pap. No 15*.

Stein, J. (1992). Investigation of the regime diagram of hydrostatic flow over a mountain with a primitive equation model. Part I: Two-dimensional flows. *Mon. Weather Rev.*, 120(12):2962–2976.

Sun, L., Chen, G., and Robinson, W. A. (2014). The role of stratospheric polar vortex breakdown in Southern Hemisphere climate trends. *J. Atmos. Sci.*, 71(7):2335–2353.

Teixeira, M., Argaín, J., and Miranda, P. (2013). Drag produced by trapped lee waves and propagating mountain waves in a two-layer atmosphere. *Q. J. R. Meteorol. Soc.*, 139(673):964–981.

Teixeira, M. A. C. (2014). The physics of orographic gravity wave drag. *Front. Phys.*, 2(July):1–24.

Teixeira, M. A. C. and Miranda, P. M. A. (2006). A linear model of gravity wave drag for hydrostatic sheared flow over elliptical mountains. *Q. J. R. Meteorol. Soc.*, 132(620):2439–2458.

Telford, P. J., Braesicke, P., Morgenstern, O., and Pyle, J. A. (2007). Technical note: Description and assessment of a nudged version of the new dynamics Unified Model. *Atmos. Chem. Phys. Discuss.*, 7(6):17261–17297.

Tibaldi, S. (1986). Envelope orography and maintenance of the quasi-stationary circulation in the ECMWF global models. *Adv. Geophys.*, 29:339–374.

Ting, M., Hoerling, M. P., Xu, T., and Kumar, A. (1996). Northern Hemisphere teleconnection patterns during extreme phases of the zonal-mean circulation. *J. Clim.*, 9(10):2614–2633.

Valdes, P. J. and Hoskins, B. J. (1991). Nonlinear orographically forced planetary waves. *J. Atmos. Sci.*, 48(18):2089–2106.

van Aalst, M. K., Lelieveld, J., Steil, B., Brühl, C., Jöckel, P., Giorgetta, M. A., and Roelofs, G.-J. (2005). Stratospheric temperatures and tracer transport in a nudged 4-year middle atmosphere GCM simulation. *Atmos. Chem. Phys. Discuss.*, 5(1):961–1006.

van Niekerk, A., Scinocca, J. F., and Shepherd, T. G. (2017). The modulation of stationary waves, and their response to climate change, by parameterized orographic drag. *Journal of the Atmospheric Sciences*, 74(8):2557–2574.

van Niekerk, A., Shepherd, T. G., Vosper, S. B., and Webster, S. (2016). Sensitivity of resolved and parametrized surface drag to changes in resolution and parametrization. *Q. J. R. Meteorol. Soc.*, 142(699):2300–2313.

von Salzen, K., Scinocca, J. F., McFarlane, N. a., Li, J., Cole, J. N. S., Plummer, D., Verseghy, D., Reader, M. C., Ma, X., Lazare, M., and Solheim, L. (2013). The Canadian Fourth Generation Atmospheric Global Climate Model (CanAM4). Part I: Representation of physical processes. *Atmosphere-Ocean*, 51(1):104–125.

von Storch, H., Langenberg, H., and Feser, F. (2000). A spectral nudging technique for dynamical downscaling purposes. *Mon. Weather Rev.*, 128(10):3664–3673.

Vosper, S. B. (2000). Three-dimensional numerical simulations of strongly stratified flow past conical orography. *J. Atmos. Sci.*, 57(22):3716–3739.

Vosper, S. B. (2015). Mountain waves and wakes generated by South Georgia: Implications for drag parametrization. *Q. J. R. Meteorol. Soc.*, 141(692):2813–2827.

Vosper, S. B., Brown, A. R., and Webster, S. (2016). Orographic drag on islands in the NWP mountain grey zone. *Q. J. R. Meteorol. Soc.*

Vosper, S. B., Wells, H., and Brown, A. R. (2009). Accounting for non-uniform static stability in orographic drag parametrization. *Q. J. R. Meteorol. Soc.*, 135(640):815–822.

Waldron, K. M., Paegle, J., and Horel, J. D. (1996). Sensitivity of a spectrally filtered and nudged limited-area model to outer model options. *Mon. Weather Rev.*, 124(3):529–547.

Wallace, J. M. and Hsu, H. (1985). Another look at the index cycle. *Tellus A*, 37 A(5):478–486.

Wallace, N. M., Tibaldi, S., and Simmons, A. J. (1983). Reduction of systematic forecast errors in the ECMWF model through the introduction of an envelope orography. *Quart. J . R. Mer. Soc*, (109):683–717.

Webster, S., Brown, A. R., Cameron, D. R., Jones, C., and P.Jones, C. (2003). Improvements to the representation of orography in the Met Office Unified Model. *Q. J. R. Meteorol. Soc.*, 129(591):1989–2010.

Wedi, N. P., Bauer, P., Deconinck, W., Diamantakis, M., Hamrud, M., Kuehnlein, C., Malardel, S., Mogensen, K., Mozdzynski, G., and Smolarkiewicz, P. K. (2015). The modelling infrastructure of the Integrated Forecasting System: Recent advances and future challenges.

Wood, N., Brown, A. R., and Hewer, F. E. (2001). Parametrizing the effects of orography on the boundary layer: An alternative to effective roughness lengths. *Q. J. R. Meteorol. Soc.*, 127(573):759–777.

Wood, N. and Mason, P. (1993). The pressure force induced by neutral, turbulent flow over hills. *Q. J. R. Meteorol. Soc.*, 119(514):1233–1267.

Wood, N., Staniforth, A., White, A., Allen, T., Diamantakis, M., Gross, M., Melvin, T., Smith, C., Vosper, S., Zerroukat, M., and Thuburn, J. (2014). An inherently mass-conserving semi-implicit semi-Lagrangian discretization of the deep-atmosphere global non-hydrostatic equations. *Q. J. R. Meteorol. Soc.*, 140(682):1505–1520.

Woollings, T., Hannachi, A., and Hoskins, B. (2010). Variability of the North Atlantic eddy-driven jet stream. *Q. J. R. Meteorol. Soc.*, 136(649):856–868.

Zadra, A., Bacmeister, J., Bouyssel, F., Brown, A., Lock, A., Figueroa, S. N., Innocentini, V., Nakagawa, M., Roff, G., and Tolstykh, M. (2013). WGNE Drag Project, http://collaboration.cmc.ec.gc.ca/science/rpn/drag_project/.

Zadra, A., Roch, M., Laroche, S., and Charron, M. (2003). The subgridscale orographic blocking parametrization of the GEM Model. *Atmosphere-Ocean*, 41(2):155–170.

Zappa, G., Shaffrey, L. C., Hodges, K. I., Sansom, P. G., and Stephenson, D. B. (2013). A multimodel assessment of future projections of north atlantic and european extratropical cyclones in the CMIP5 climate models. *J. Clim.*, 26(16):5846–5862.

Zappa, G. and Shepherd, T. G. (2017). Storylines of atmospheric circulation change for European regional climate impact assessment. *J. Clim.*, Submitted.